

**Chemical Vapor Deposition Grown
Pristine and Chemically Doped Monolayer Graphene**

Liuyan Zhao

Submitted in partial fulfillment of the requirements
for the degree of Doctor of Philosophy
in the Graduate School of Art and Sciences

COLUMBIA UNIVERSITY

2013

© 2013

Liuyan Zhao

All Rights Reserved

ABSTRACT

Chemical Vapor Deposition Grown Pristine and Chemically Doped Monolayer Graphene

Liuyan Zhao

Chemical vapor deposition growth has been a popular technique to produce large-area, high-quality monolayer graphene on Cu substrates ever since its first demonstration in 2009. Pristine graphene grown in such a way owns the natures of zero charge carriers and zero band gap. As an analogy to semi-conductor studies, substitutional doping with foreign atoms is a powerful way to tailor the electronic properties of the host materials. Within such a context, this thesis focuses on growing and characterizing both pristine and chemically-doped CVD grown monolayer graphene films at microscopic scales. We first synthesized pristine graphene on Cu single crystals in ultra-high-vacuum and subsequently characterized their properties by scanning tunneling microscopy/spectroscopy (STM/S), to learn the effects of Cu substrate crystallinity on the quality of graphene growth and to understand the interactions between graphene films and Cu substrates. In the subsequent chapters, we chemically doped graphene with nitrogen (N) and boron (B) atoms, and characterized their topographic and electronic structures via STM/S. We found that both N and B dopants substitutionally dope graphene films, and contribute electron and hole carriers, respectively, into graphene at a rate of approximately 0.5 carrier/dopant. Apart from this, we have made comparisons between N- and B-doped graphene films in aspects of topographic features, dopant distribution and electronic perturbations. In the last part of this thesis, we used Raman spectroscopy mapping to investigate the N dopant distribution within and across structural grains. Future experiments are also briefly discussed at the end of the thesis.

Content

List of Figures	iv
Acknowledgement	viii
1 Introduction	1
1.1 Overview on Pristine Graphene	1
1.1.1 The Electronic Properties of Pristine Graphene	1
1.1.2 The Fabrications of Pristine Graphene	7
1.2 Overview on Chemically Doped Graphene	11
1.2.1 The Fundamental Limits of Pristine Graphene	11
1.2.2 The Chemical Doping of Graphene	13
1.3 Scanning Tunneling Microscopy/Spectroscopy	19
1.3.1 The Basic Theory of STM/S	19
1.3.2 Discussions of Tunneling Matrix and Temperature Effects	23
1.4 Micro-Raman Spectroscopy	25
1.4.1 Raman Spectroscopy of Graphene	25
1.5 Outline of Thesis	29
1.6 References	32
2 Influence of Cu Crystal Surface on CVD Graphene Growth	38
2.1 Overview of Graphene Growth on Cu Substrates	38
2.1.1 Standard Recipe for CVD Graphene Growth on Cu Substrates	38
2.1.2 Modified Recipes for CVD Graphene Growth on Cu Substrates	39
2.2 Sample Preparation in UHV	41
2.2.1 Preparations of Cu Substrates	41
2.2.2 Preparations of Graphene on Cu Substrates	43
2.3 Atomic Scale Characterization of Graphene/Cu Substrates	47
2.3.1 Graphene/Cu(111)	47

2.3.2	Graphene/Cu(100)	61
2.3.3	Graphene/Cu foil	63
2.4	Raman Spectroscopy of Graphene/Cu Substrates	65
2.5	References	68
3	Visualizing Individual Nitrogen Dopants in N-doped Graphene	71
3.1	Overview of Nitrogen Doped Graphene	71
3.1.1	Fabrications of Nitrogen Doped Graphene	71
3.1.2	Characterizations of Nitrogen Doped Graphene	75
3.1.3	Our Approaches to Study Nitrogen Doped Graphene	77
3.2	Topographic Characterizations of Nitrogen Doped Graphene	77
3.2.1	Structure of Individual Nitrogen Dopants	77
3.2.2	Distribution of Nitrogen Dopants	82
3.3	Electronic Characterizations of Nitrogen Doped Graphene	84
3.3.1	Charge Carrier Injection from Nitrogen Dopants	85
3.3.2	Band Gap Opening or Not?	90
3.3.3	Perturbation to Local Electronic Structures	92
3.3.4	Quantum Interferences in the Presence of Nitrogen Dopants	95
3.4	Raman Characterizations of Nitrogen Doped Graphene	100
3.5	NEXAFS Characterizations of Nitrogen Doped Graphene	102
3.6	References	103
4	Atomic and Electronic Structures of B-doped Graphene	107
4.1	Background of Boron Doped Carbon Lattices	107
4.1.1	Literature of Boron Doped Allotropes	108
4.1.2	Our Approaches for B-doped Graphene Preparations and Characterizations	110
4.2	Similarities with N-doped Graphene	112
4.2.1	Boron Doping Forms	113
4.2.2	Electronic Structures	115
4.3	Differences to N-doped Graphene	119
4.3.1	STM Topographic Features	119
4.3.2	Dopant Distributions between Sublattices	125
4.4	NEXAFS Characterizations on B-doped Graphene	131

4.5	Brief Discussions on “Flow-Doped” Graphene	132
4.6	References	133
5	Nitrogen Dopant Distribution in N-doped Graphene Polycrystal	137
5.1	Background of Impurity/Dopant Distribution	137
5.1.1	Review of Dopant Distribution in Three-dimensional Polycrystals	137
5.1.2	Chances in Chemically Doped Two-dimensional Polycrystals	139
5.1.3	Approaches and Subjects in Our Experiments	140
5.2	Micro-Raman Spectroscopy Studies of N Dopant Distribution	141
5.2.1	Individual Raman Spectrum and Its Statistics on N-doped Graphene	141
5.2.2	Raman Mapping on N-doped Graphene	145
5.3	Scanning Tunneling Microscopy Studies on N Dopant Distribution	153
5.3.1	STM of N Dopant Distribution in Polycrystalline N-doped Graphene	153
5.3.2	STM of N Dopant Distribution in N-doped Graphene Islands	156
5.4	Monte Carlo Simulations on N Dopant Distribution	158
5.5	References	160
6	Summary and Future Experiments	163
6.1	Summary	163
6.2	Future Experiments	164

List of Figures

1.1	Crystal and reciprocal lattices of monolayer graphene	2
1.2	Tight binding band structure of monolayer graphene	5
1.3	Chirality for both conduction and valence band at both K and K' Dirac cones	6
1.4	Mechanically exfoliated graphene	7
1.5	Epitaxial growth of graphene on SiC substrate	8
1.6	Grain boundaries in CVD grown graphene	10
1.7	Large grain size graphene grown by the pita-pocket method	11
1.8	Cartoon models for different doping forms of N/B dopants	15
1.9	Cartoon model for F-doped graphene	18
1.10	Band gap opening at Dirac points	18
1.11	Diagrams for tunneling processes	20
1.12	Calculated orbital intensity of B,C,N as a function of radial distance	24
1.13	Phonon and electron band structures of monolayer graphene	26
1.14	Diagrams of Raman scattering processes for D, G, D' and 2D bands	28
1.15	High resolution Raman spectra for pristine and defected graphene	29
2.1	Cartoon for graphene CVD growth setup	39
2.2	Crystal structure for Cu single crystal	41
2.3	Preparations of Cu(111) surface	43
2.4	Cu(111) surface after 1 st trial of graphene growth	45
2.5	Graphene nanoisland	46
2.6	Graphene grown on Cu(111) single crystal	48
2.7	Cartoon diagram visualizing Moiré pattern formed by graphene and Cu(111)	49
2.8	Example of Moiré pattern in one-dimensional case	50
2.9	Calculations of Moiré pattern between graphene and Cu(111)	52
2.10	LEED pattern of graphene/Cu(111)	53
2.11	Grain boundaries in graphene films grown on Cu(111) surface	54
2.12	Graphene on Cu(111) after one month exposure to air	55

2.13	Bias dependent topographs of graphene/Cu(111)	57
2.14	Quantum interference pattern map of graphene/Cu(111)	58
2.15	Modified band structure of Cu(111) SS in the presence of graphene	60
2.16	Graphene grown on Cu(100) single crystal	61
2.17	Moiré pattern of graphene on Cu(100) surface	62
2.18	LEED pattern of graphene on Cu(100) surface	63
2.19	Optical image of graphene growth on Cu foil in UHV condition	64
2.20	STM topo of graphene on Cu foil grown by the standard CVD recipe	65
2.21	Raman spectra taken on graphene/Cu(111) and graphene/Cu(100).....	67
3.1	Cartoon for N-doped graphene CVD growth setup	72
3.2	Cartoon diagram for different doping forms of N dopants	73
3.3	Cartoon for transferring CVD grown graphene from Cu foil to target substrates	75
3.4	Topography comparison between N-doped and pristine graphene	78
3.5	Topography of individual graphitic N dopants	79
3.6	“Tail” feature in STM topography of N-doped graphene	81
3.7	STM topo of other defect forms observed in N-doped graphene	81
3.8	Spatial distribution of N dopants for various N concentrations	83
3.9	Cartoon for N dopant in A or B sublattice of the honeycomb lattice	83
3.10	N dopant distribution between A-B sublattice of graphene lattice	84
3.11	Dirac point shift relative to Fermi level in vicinity of N dopants	86
3.12	Average charge carrier doping rate by graphitic N dopants	88
3.13	Effect of Cu foil on the electronic structures of N-doped graphene	90
3.14	Sublattice asymmetry induced by graphitic N dopants	91
3.15	dI/dV spectra taken on a N dopant and its first carbon neighbors.....	92
3.16	dI/dV spectra taken on/around a N dopant and far away from a N dopant	93
3.17	Spectroscopic mapping around a single graphitic N dopant	94
3.18	Cartoon diagram for inter-and intra-valley scattering in graphene.....	95
3.19	Coexistence of inter-and intra-valley scattering in N-doped graphene.....	96
3.20	Inter-valley scattering in N-doped graphene/Cu foil	97
3.21	Decay of inter-valley scattering in space	98
3.22	Intra-valley scattering in N-doped graphene/Cu foil	99
3.23	Raman spectra of N-doped graphene on SiO ₂ /Si	101

3.24	NEXAFS spectra on pristine and N-doped graphene at N K-edge	102
4.1	Raman spectra on B-doped and N-doped graphene	110
4.2	Cartoon diagram for a CVD setup for B-doped graphene growth	112
4.3	STM topography for “tube-doped” graphene/Cu foil	113
4.4	Topography of individual graphitic B dopants	114
4.5	Dirac point shifts in STS on “tube-doped” graphene on Cu foil	116
4.6	Averaged hole concentration as a function of B density	117
4.7	Spectroscopic mapping around a single B dopant	118
4.8	STM topographic differences between graphitic B and N dopants	120
4.9	DFT calculations of structure and charge density differences for graphitic B and N dopants on a commensurate Cu slab	121
4.10	Stone-wales defects observed on “tube-doped” graphene	123
4.11	Resonances in LDOS induced by SW defects	124
4.12	Dopant distribution between A-B sublattices for B- and N- doped graphene.....	126
4.13	Comparison between B and N distribution at a large scale	127
4.14	Statistics of B and N dopant distributions between sublattices	130
4.15	NEXAFS spectra of “tube-doped” graphene at B1s edge	132
4.16	Topography for “flow-doped” graphene/Cu foil.....	133
5.1	Raman spectra of pristine and N-doped graphene on SiO ₂ /Si	142
5.2	Raman spectra taken on as-grown pristine and N-doped graphene	143
5.3	Statistics of Raman spectra on pristine and N-doped graphene/SiO ₂ /Si	145
5.4	Grain boundaries in pristine graphene imaged by D/2D Raman map	146
5.5	Raman mapping on NG_10m sample	148
5.6	Raman maps of NG_xm films with varying growth time xm.....	150
5.7	Raman mapping of NG_Pyridine sample	151
5.8	Cartoon diagram for calculating the width of N depleted regions	152
5.9	Calculated widths for N depleted regions in NG_xm and NG_Pyridine.....	153
5.10	STM topography of N distribution in as grown NG_10m film on Cu foil	155
5.11	STM topography of N distribution in N-doped graphene island on Cu(111)	157
5.12	Monte Carlo simulations of N distribution in finite sized graphene sheet	159

6.1	Diagram of STM/S measurements of backgated N-doped graphene on BN/SiO ₂ /Si	166
6.2	STM topography of graphene on BN/SiO ₂ /Si	167
6.3	Optical and Raman map images of large-domain-size N-doped graphene islands	168
6.4	Influence of H ₂ flow on N dopant distribution and N-doped graphene island shape	169

Acknowledgements

Looking back now, I feel that I had never learnt as much as in the past five years during which I was very lucky to have so much help from so many people. Without them, I could not imagine I would finally make this thesis possible.

First and foremost, let me thank my Ph.D. advisor, Prof. Abhay Narayan Pasupathy, a kind and patient mentor who has been always available for discussions despite a tight schedule. He not only taught me experimental techniques and scientific thoughts, but also guided me with confidence and persistence when confronting difficulties, which is of great help at both academic and personal levels. I am truly indebted and grateful for all the help that he gave me.

I owe also great gratitude to Prof. George W. Flynn. I spent a majority of the last five years in his lab, doing experiments, joining the weekly group meetings and attending the group events, all of which make me feel being a part of the group – thanks! Moreover, thanks for being supportive on my projects and offering help during my seeking for a job.

Meanwhile, my group mates in both Pasupathy group and Flynn group have made my past five years bright, helping me through all kinds of difficulty periods in researches. Thanks to Chockalingam Subbiah, Ulrich Wurstbauer, Carlos Arguello, Ethan Rosenthal, Erick Andrade, Michael Vitz, Deajin Eom, and Li Liu. In particular, thanks to Kwang Taeg Rim who showed me every details of the two machines in Flynn lab and taught me to be optimistic towards everything; thanks to Scott J. Goncher and Christopher Gutiérrez with whom we shared a lot of painful at the moment but joyful afterwards memories on the Low Temperature - machine; thanks to Amir Zabet who taught me how to think in a way of

chemists; thanks to Hao Wang who always encouraged me whenever I got depressed in experiments.

I also have had the good luck to collaborate a number of wonderful people outside Pasupathy and Flynn groups. Thanks to Prof. Aron Pinczuk and his student Rui He from whom I learnt measurements and analysis of Raman Spectroscopy on graphene layers. Thanks to Prof. Philip Kim and his postdoc Keun Soo Kim who showed me the growths of graphene by CVD method. Thanks to Prof. David Reichman, Prof. Mark Hybertsen and their student Lucia Pálová who always provided important theoretical insights into our experimental data. Thanks to Prof. Tony Heinz and his student Hui Zhou who offered insightful ideas on our projects during our short overlap at Columbia. Thanks to Prof. Jiwoong Park and his student Mark P. Levendorf at Cornell University who consistently provided us with good quality samples over the last two years. Thanks to Theanne Schiros and her colleagues at BNL and SLAC who always provided us with detailed feedbacks on sample qualities and suggestions on producing better quality samples.

Finally, I would like to thank my husband, Gongjun Xu, for your trust and support on whatever I decided to go for. The most precious moments between us are the ones that we spent together to overcome various difficulties. I truly remember and appreciate that you have been always around whenever I needed you, and I know you will be there in our next stages of life as well. Thank you, Gongjun!

New York, New York

Liuyan Zhao

To my parents

Chapter 1

Introduction

1.1 Overview on Pristine Graphene

1.1.1 The Electronic Properties of Pristine Graphene

Ever since its first isolation from graphite in 2004 [1], graphene has attracted enormous attention which spans a wide spectrum of interests, ranging from new quantum phases in condensed matter systems [2, 3] and bench-top models for high energy physics [4, 5] to mediating chemical reactions [6-8] and applications in electric and photonic devices [9-11]. Even before the isolation of graphene, theorists had already explored its elementary electronic properties thanks to the simplicity of its crystal structure [12, 13].

Graphene is a single layer of carbon (C) atoms arranged in a honeycomb structure. The unit cell of this structure consists of two equivalent carbon atoms which are usually denoted as the A and B sublattices of graphene (red and blue sites in Fig 1.1a). Each carbon atom has three nearest neighbors in its opposite sublattice and four valence electrons. The Bravais lattice has unit lattice vectors of

$$\vec{a}_1 = \left(\frac{3a}{2}, \frac{\sqrt{3}a}{2} \right), \vec{a}_2 = \left(\frac{3a}{2}, -\frac{\sqrt{3}a}{2} \right), \quad (1.1)$$

where $a \approx 1.42\text{\AA}$, the nearest carbon-carbon distance. The corresponding reciprocal lattice vectors are

$$\vec{b}_1 = \left(\frac{2\pi}{3a}, \frac{2\sqrt{3}\pi}{3a} \right), \vec{b}_2 = \left(\frac{2\pi}{3a}, -\frac{2\sqrt{3}\pi}{3a} \right), \quad (1.2)$$

and the Brillouin zone (BZ) is defined by the hexagon highlighted with red dashed line in Fig. 1.1 b.

Of particular importance is the two sets of corners of the BZ, K & K' , which are referred to as Dirac points because of the linear band structure of graphene at these points in k -space and defined as

$$\vec{K} = \left(\frac{2\pi}{3a}, \frac{2\pi}{3\sqrt{3}a} \right), \vec{K}' = \left(\frac{2\pi}{3a}, -\frac{2\pi}{3\sqrt{3}a} \right). \quad (1.3)$$

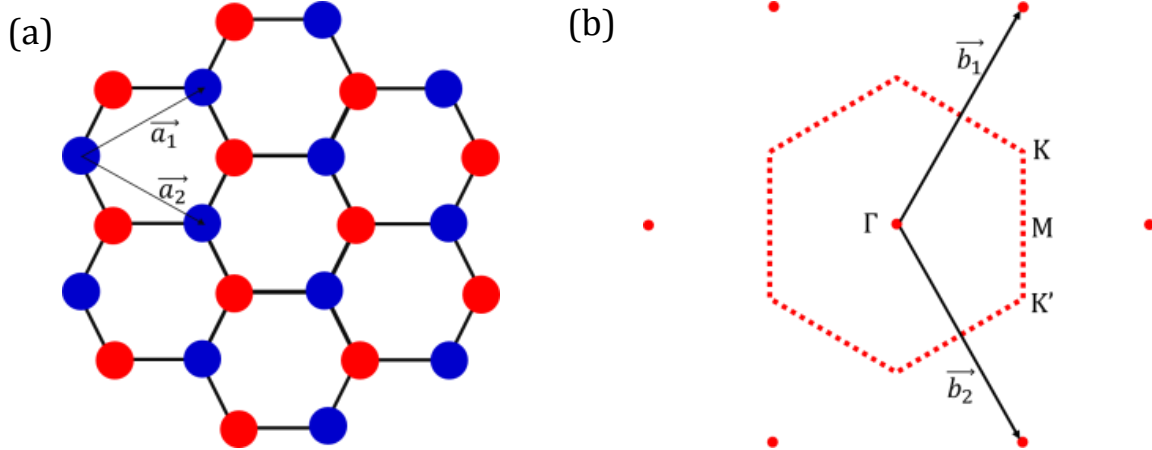


Fig. 1.1 Crystal and reciprocal lattice of monolayer graphene (a) Honeycomb lattice of graphene with two sets of sublattices marked with red and blue dots and unit vectors marked with \vec{a}_1 and \vec{a}_2 . (b) Reciprocal lattice of graphene with outside hexagon (highlighted with six red spots) for Bragg peaks of atomic lattice, and inside hexagon (highlighted with red dashed line) as first Brillouin Zone.

In plane σ bonds are formed by the sp^2 hybridization of the valence electrons from the in-plane orbitals p_x , p_y and s . Thus, three of the four valence electrons from each carbon atom contribute to the formation of σ bonds with the three nearest neighbors. The σ bond is extremely strong which makes graphene the strongest material in the world [14, 15]; however, the electrons forming σ bonds are so tightly bound that they do not contribute to the electronic transport. The remaining one electron from each carbon atom, consisting of a p_z orbital, form the delocalized π bonds with the three nearest neighbors and determine the low-energy electronic band structure of graphene [12, 13, 16].

Within the nearest-neighbor approximation, the tight-binding Hamiltonian is

$$\hat{H} = -Y_0 \sum_{i,j} (\hat{a}_i^\dagger \hat{b}_j + h.c.), \quad (1.4)$$

where \hat{a}_i^\dagger (\hat{a}_i) or \hat{b}_i^\dagger (\hat{b}_i) creates (destroys) an electron on the A or B sublattice, respectively, the nearest neighbor hopping integral is $Y_0 \approx 3.16\text{eV}$, and the summation is over all nearest neighbors in the honeycomb lattice. The vectors connecting the three nearest neighbors are (seen in Fig. 1.1a)

$$\vec{\delta}_1 = \left(\frac{a}{2}, \frac{\sqrt{3}a}{2}\right), \vec{\delta}_2 = \left(\frac{a}{2}, -\frac{\sqrt{3}a}{2}\right), \vec{\delta}_3 = (-a, 0). \quad (1.5)$$

We can write the Hamiltonian in the basis of wavefunctions on A and B sublattices (ψ_A, ψ_B) for an arbitrary momentum \vec{k} ,

$$\hat{H} = \begin{pmatrix} 0 & \sum_j e^{i\vec{k} \cdot \vec{\delta}_j} \\ \sum_j e^{-i\vec{k} \cdot \vec{\delta}_j} & 0 \end{pmatrix}, \quad (1.6)$$

and calculate the eigenvalues of this Hamiltonian,

$$\varepsilon_{\pm}(\vec{k}) = \pm \gamma_0 \sqrt{3 + 4 \cos\left(\frac{\sqrt{3}ak_x}{2}\right) \cos\left(\frac{ak_y}{2}\right) + 2 \cos(ak_y)}, \quad (1.7)$$

where \pm stands for π^* and π bands. The band structure from Eq. 1.7 is shown in Fig. 1.2a. It displays the electron-hole symmetry in the band structure and the valence (π) and conduction (π^*) bands meet each other at six BZ corners, K & K' 's. It is important to mention that the electron-hole symmetry results from the nearest-neighbor approximation. This symmetry is no longer preserved when the next nearest-neighbor hopping is considered. However, the degeneracy at K & K' points is caused by the inversion symmetry of the graphene lattice structure and would not be destroyed by higher order approximations [16].

Recalling that each carbon atom contributes one electron to π bond formation, the bands for undoped graphene would be exactly half filled. As a result, the Fermi surface for pristine graphene consists of only six points at BZ corners, K & K' 's. If we only focus on the energy bands near Fermi surface and expand the Hamiltonian around K & K' points, i.e. define $\vec{p} \equiv \vec{K}(\vec{K}') - \vec{k}$, we will get a Dirac-like Hamiltonian

$$\hat{H} = v_F \hat{\sigma} \cdot \vec{p}, \quad \text{at } \vec{K} \text{ points}, \quad (1.8)$$

$$\text{or } \hat{H} = v_F \hat{\sigma}^* \cdot \vec{p}, \quad \text{at } \vec{K}' \text{ points}, \quad (1.9)$$

where $v_F = \frac{3a}{2}\gamma_0$, and $\hat{\sigma} = (\sigma_x, \sigma_y)$ which is the vector of Pauli matrices

$$\sigma_x = \begin{pmatrix} 0 & i \\ -i & 0 \end{pmatrix}, \sigma_y = \begin{pmatrix} 0 & 1 \\ 1 & 0 \end{pmatrix}, \sigma_z = \begin{pmatrix} 1 & 0 \\ 0 & -1 \end{pmatrix}, \quad (1.10)$$

and the basis chosen is $(\psi_{K,A}, \psi_{K,B})$ at K point or $(\psi_{K',A}, \psi_{K',B})$ at K' point. The eigenvalues at both K and K' points are

$$\varepsilon(p) = \pm v_F |\vec{p}| \quad (1.11)$$

in which the energy shows linear momentum dependence. See the Fig. 1.2b for the zoom-in spectrum near the Fermi level.

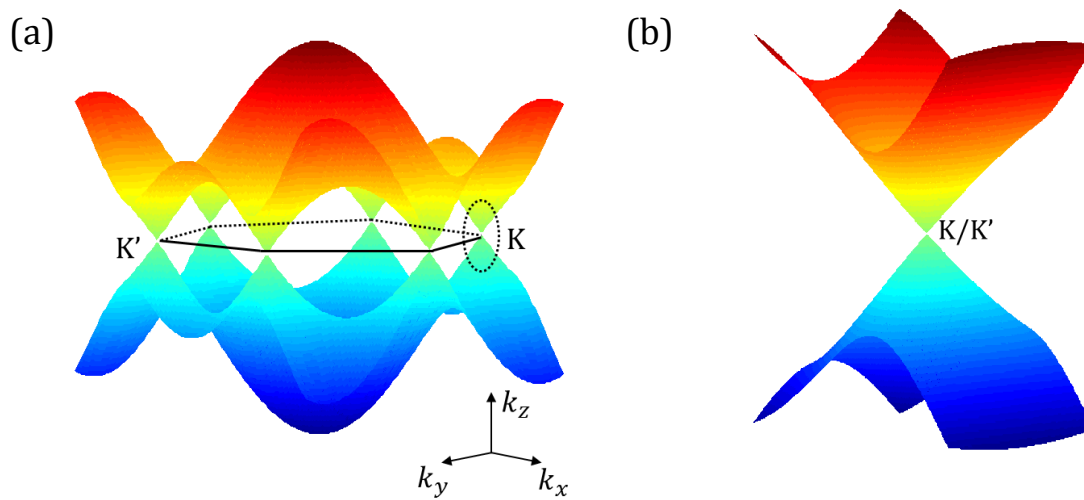


Fig. 1.2 Tightbinding band structure of monolayer graphene (a) Electronic band structure of graphene calculated by tight binding model with only nearest neighbor hopping showing electron-hole symmetry. (b) Close-look at the energy spectrum near Dirac point (highlighted by black dashed ellipse in (a)) showing a linear dispersion.

The form for the Hamiltonian near the K and K' points in graphene is the same as that for relativistic electrons first proposed by Dirac [17], except that the speed of light, c , in Dirac's theory is replaced by Fermi velocity in graphene, $v_F \approx c/300$. This is the reason why the K and K' points are referred to as Dirac points in the graphene band structure. However, although the graphene Hamiltonian takes the mathematical form of the Dirac equation, the "spin" in the context of graphene does not refer to the electron spin as in Dirac's theory. Instead, it refers to the weight of

the wavefunction on the basis of (ψ_A, ψ_B) , which is the reason why it is denoted as the pseudo-spin of graphene. Nevertheless, pseudo-spin preserves the properties of a spinor such as chirality, \hat{P} ,

$$\hat{P} = \frac{\hat{\sigma} \cdot \vec{p}}{|\vec{p}|}. \quad (1.12)$$

In fact, this chirality operator projects the spin onto momentum and normalizes the projection to the momentum value. The eigenstates of the Hamiltonian are also eigenstates of the chirality operator, and the eigenvalues of chirality result in $P = \pm 1$ with +1 for conduction band and -1 for valence band at K point. Similarly, the eigenvalues for $P = \pm 1$ at K' point but with -1 for conduction band and +1 for valence band, as shown in Fig. 1.3.

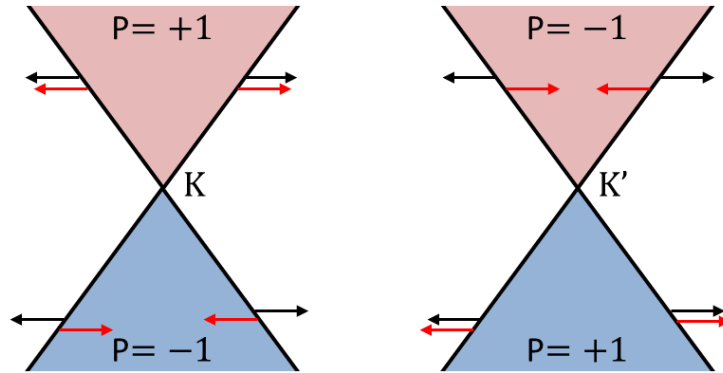


Fig. 1.3 Chirality for both conduction and valence bands at both K and K' Dirac cones. Black arrows indicate momentum directions, and red arrows indicate pseudo-spin directions. As shown above, the momentum is parallel to the pseudo-spin in the conduction band of valley K and the valence band of valley K' (i.e. $P=+1$) and anti-parallel in the conduction band of valley K' and the valence band of valley K (i.e. $P=-1$).

The density of states per unit cell, which is derived from the band structure of graphene, is

$$\rho(E) = \frac{2A_c |\epsilon|}{\pi v_F^2}. \quad (1.13)$$

The density of states (DOS) spectrum shows a linear dependence on energy with zero DOS intensity at $\epsilon(p) = 0$ which corresponds to the Dirac points.

1.1.2 The Fabrication of Pristine Graphene

Benefiting from the unique electronic structure discussed in section 1.1.1, graphene has been proven in research labs to possess a number of extremely unique properties, including highest mobility, longest mean-free-path [1-3] and so on [18-20]. The graphene samples used in these studies are primarily made by mechanical exfoliations of graphite, which is the method that *Geim and Novoselov et. al.* at Manchester University first invented in 2004 [1]. Although this method produces high quality graphene samples, the size of the sample is typically limited to a few tens of micrometers (μm) which is large enough for research purpose but not for industrial applications. Fig.1.4a shows a picture of this exfoliation process [21], and Fig.1.4b displays an optical image of such a graphene flake exfoliated onto a SiO_2/Si substrate with a 300nm thick oxide layer.

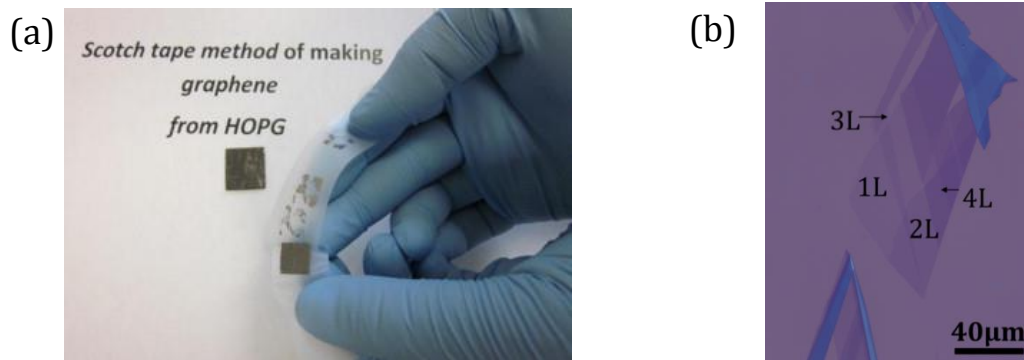


Fig. 1.4 Mechanically exfoliated graphene; (a) Fabrication of graphene from HOPG by mechanical exfoliations with scotch tape. Figure cited from Ref. [21]. (b) Optical image of mechanically exfoliated graphene which is deposited on 300nm thick SiO_2/Si wafer. Different layer numbers marked according to the color contrast. As seen in (b), the monolayer graphene in this sample is $\sim 20\mu\text{m}$ by $40\mu\text{m}$. Image cited from <http://technologiesofworld2013.blogspot.com/2013/04/graphene.html>.

In order to scale up the size of graphene films, there are two most popular methods that have been recently developed. One is the epitaxial growth of graphene on SiC(0001) surfaces first reported by De Heer group at The Georgia Institute of Technology [22]. In this method, graphene films as large as SiC wafers (shown in Fig.1.5a) can be grown on both the C-face and the Si-face of Si(0001) through a high temperature ($\sim 1200^\circ\text{C}$) graphitization procedure, and the number of layers of graphene films is typically tuned by the graphitization time. Due to the weak interactions between graphene layers produced in this manner, even multilayer graphene grown on SiC(0001) behaves as a single sheet of graphene [23-25]. Despite the large size of graphene achieved in this method, the quality of graphene is limited by a few factors including wrinkles [24], as in Fig.1.5b, atomic defects (particularly for growth on the Si-face) [26], as in Fig.1.5c, and difficulties in isolating graphene from SiC substrates.

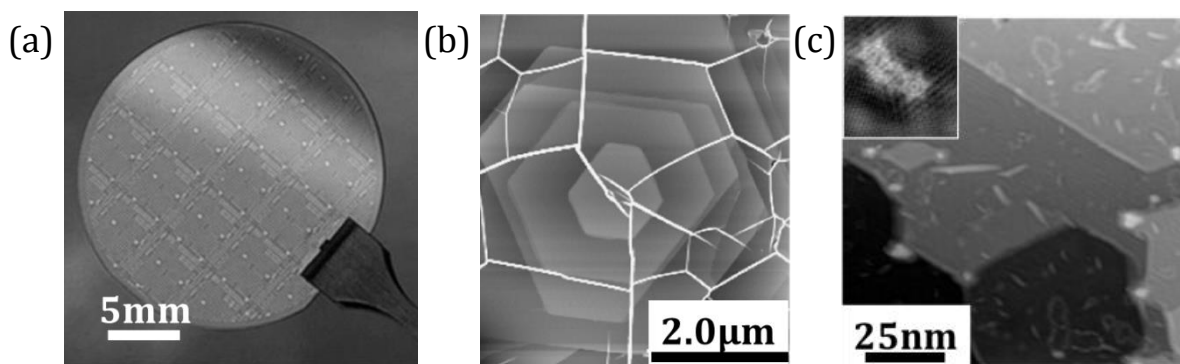


Fig. 1.5 Epitaxial growth of graphene on SiC substrate; (a) Arrays of FETs made out of graphene grown on the entire surface of a two-inch SiC wafer. Image cited from <http://nanotechweb.org/cws/article/tech/39365> (b) AFM image of graphene on SiC, showing wrinkles formed in graphene. Image cited from Ref. [23] (3) STM topography image, showing many “loop” defects in graphene on SiC. Inset is a zoom-in of one of the “loop” defects observed in (c), which has been proven to result from Stone-wales defects. Images cited from Ref. [26].

The other method is chemical vapor deposition (CVD) growth of graphene on transition metal substrates such as Ni [27], Pt [28], Ru [29], Ir [30], Rh [31], Pd[32], ... , and more recently Cu

[33]. During the growth procedure, carbon sources (typically Methane CH_4) together with Hydrogen (H_2) flow over a hot transition metal substrate at a temperature of $\sim 1000^\circ\text{C}$ for a certain amount of time and then the system is cooled down to room temperature. Usually, the transition metal acts as a catalyst to break C-H bonds in carbon sources. However, the mechanism for graphene formation from the isolated carbon atoms varies between metals and depends on the carbon solubility in a specific transition metal. For example, Ni has high carbon solubility so that carbon atoms first dissolve into Ni substrates at high temperature and then precipitate onto the surface of Ni substrates when cooling down to room temperature. Due to such a growth mechanism, multilayer graphene grow on Ni substrates, and the number of layers is controlled by the amount of carbon atoms dissolved in the substrates at high temperature. However, Cu has very low carbon solubility even up to its melting temperature, so graphene growth on Cu substrates is a pure surface reaction process. This is why graphene predominantly grows monolayer on Cu substrates [34].

Although the exact mechanism for graphene seeding and nucleation on Cu surfaces remains disputed [35-38], CVD graphene growth on Cu substrates gained its popularity among the growths on the transition metals due to its low cost, self-limiting growth process, and high graphene quality as well. The majority (>99.9%) of the defects in CVD graphene films are grain boundaries where two graphene grains which are mis-oriented or translated merge together (cartoon shown in Fig.1.6.a). As first proved by researchers at Cornell University and UC Berkeley [39, 40], mis-orientations between graphene grains are the main source of grain boundaries. In Fig.1.6.b, the false-colored TEM image shows the patchwork-like structure for a polycrystalline graphene film, in which different colors represent the different oriented angles of the grains. The typical grain size produced in this CVD recipe is on the order of a few micrometers. Zooming into one boundary between two grains, a line of defects is formed by pentagons and heptagons as shown in Fig.1.6.c.

These randomly distributed line defects were predicted [41] and proven [42] to impair the electric transport in graphene and their reduction or even elimination is now desired.

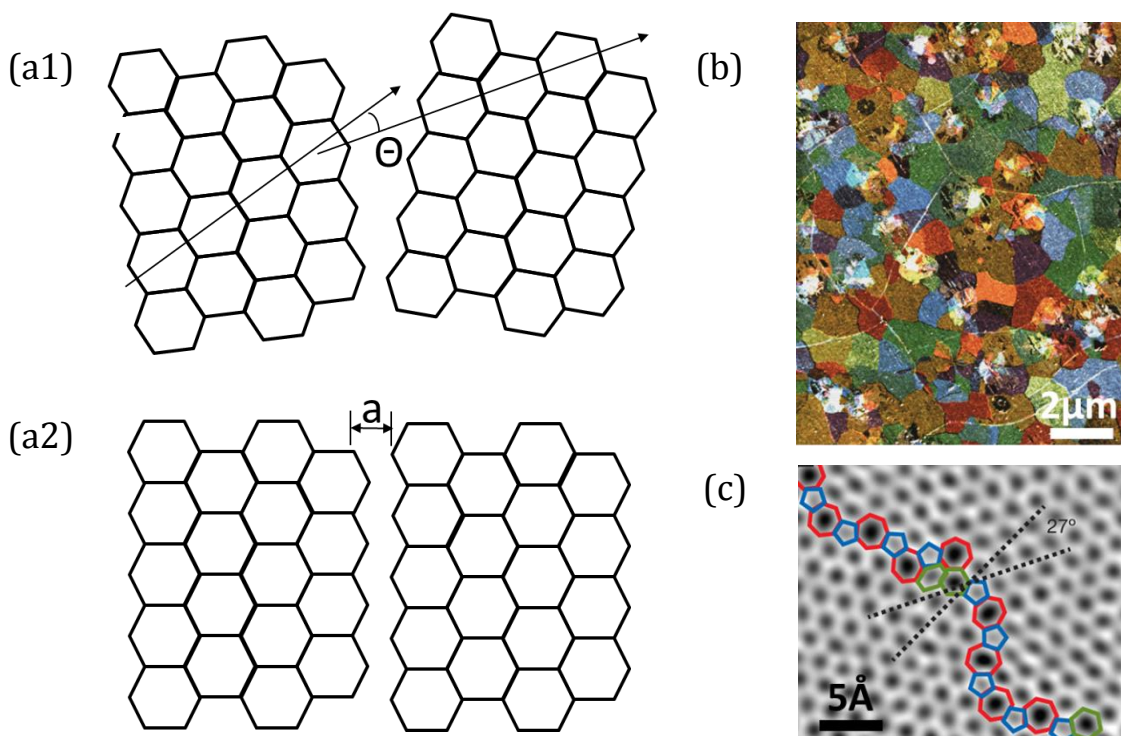


Fig. 1.6 Grain boundaries in CVD grown graphene; (a) Diagrams showing how a grain boundary is formed in graphene lattice. (a1) shows a mis-orientation of angle θ between two domains, and (a2) shows a translational mis-match of length “a” between two domains. (b) A false colored image mapping graphene domains with different colors indicating different crystal orientations. Image cited from <http://www.ccmr.cornell.edu/news/news.html?id=232>. (c) A zoom-in image at the grain boundary revealing a defect line composed of heptagons and pentagons. Image cited from Ref. [39].

In principle, fewer seeds at the beginning of growth results in fewer grains and thus fewer grain boundaries. Along this direction, large grain size graphene has been produced when Cu substrates are folded into a pita-pocket geometry [43] (shown in Fig.1.7.a). A single grain size can be extended up to sub-millimeter scale, as shown in Fig.1.7.b.

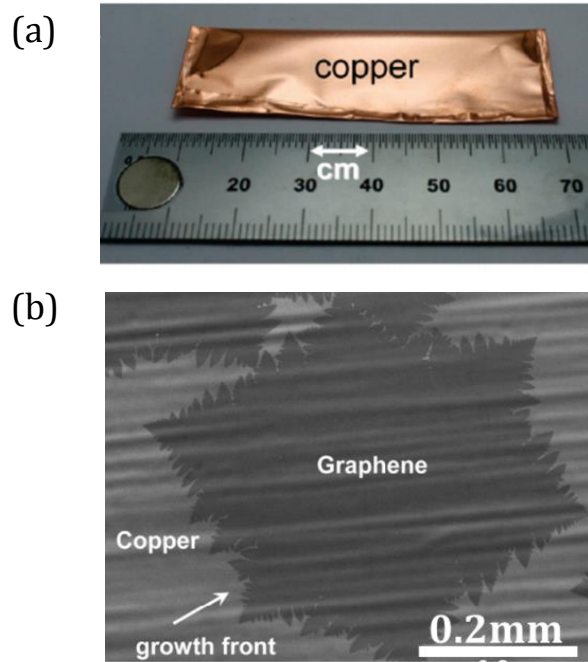


Fig. 1.7 Large grain size grain grown by pita-pocket method; (a) Copper foil folded into pita-pocket geometry. (b) Pristine graphene grown by low pressure, pita-pocket geometry, with single grain size as large as sub millimeters. Images cited from Ref. [42].

1.2 Overview on Chemically Doped Graphene

1.2.1 The Fundamental Limits of Pristine Graphene

Owing to the exceptional electronic properties of graphene, it has been proposed to be a promising candidate for many applications such as transparent electrodes for solar cells, graphene based field-effect-transistors (FET), and so on. However, before putting these proposals into practice, there are some major limits in graphene's electronic structure that one has to overcome.

The first shortcoming concerns free charge carriers in graphene. As the valence electrons in pristine graphene exactly fill the electronic bands up to Dirac point, there are no free charge carriers available for electronic transport in pristine graphene. Consequently, transport

measurements show a minimum conductivity near this charge neutrality point. It is important to mention that this minimum conductivity does not go to zero but stays at $4e^2/\hbar$ even for the cleanest graphene sample [1-3, 16, 18]. This minimum conductivity lowers the efficiency of electron transport in graphene, and it must be increased for applications like electrodes. An obvious way to achieve this goal is to introduce free charge carriers in order to move away from the charge neutrality point. As shown in Fig.1.8.a, the electric field effect is a versatile way to introduce either electron or hole carriers into graphene by varying the polarity of the gate voltage. However, this field effect doping depends on the external voltage through a dielectric media and may complicate the geometry of a device in application. Therefore, it is desired to introduce permanent free charge carriers with well-controlled carrier type and concentration which is one of the major focuses of this thesis.

The other limit is the semimetal nature of graphene. As seen from both $E(\vec{k})$ and $DOS(E)$ spectrum in section 1.1.1, there is no band gap over any energy window in the graphene band structure. However, such an electronic bandgap is essential in device physics and technology and governs the operation of semiconductor devices because it allows the host material to switch the flow of electrons on and off. It has been shown that a wide, tunable band gap can be realized in AB stacked bilayer graphene via a dual gating technique that breaks inversion symmetry [44]. However, it is still difficult to produce large area AB stacked bilayer graphene films compared to monolayer graphene [45]. In monolayer graphene, the absence of a band gap is protected by the AB sublattice symmetry of honeycomb structure. By introducing short range potentials which breaks up the AB sublattice symmetry, it is in principle possible to open up a band gap at the Dirac points [18]. Another focus of this thesis is to experimentally test these effects on the graphene band

structure by introducing atomically sharp potentials by incorporating atomic defects in the honeycomb lattice.

Of course, besides charge injection and band gap engineering, the electronic properties of graphene can be tuned by many other methods like introducing magnetism [46, 47], superconductivity [48, 49], edge states [50], topological orders [51] and charge density waves [52]. Given such a wide spectrum of tunable properties, this thesis is limited to the first two aspects specified above.

1.2.2 The Chemical Doping of Graphene

Chemical doping a host material with foreign species is a promising way to tailor the electronic properties of the host material. This technique has been widely employed in the modern semiconductor industry most commonly with electron/hole-doped silicon. To make a simple analogy between graphene and silicon, one could imagine modulating the electronic properties of graphene via chemical doping as well. Let's follow up with the desired properties of graphene which were discussed above.

Firstly, in order to introduce free charge carriers into graphene films, species with an excess or depletion of electrons are usually suitable. Taking a look at the periodic table, we can first locate the two neighbors of carbon which are boron on the left side and nitrogen on the right side. Intuitively, boron has one less electron than carbon, so it should withdraw some amount of electrons from the carbon lattice when it is embedded in the matrix. As a result, boron doped graphene film would be hole doped. Similarly, nitrogen doped graphene would be electron doped. However, theoretical calculations predict much richer physics than such intuitions [53, 54]. First, there are multiple ways that a boron/nitrogen atom can incorporate into the honeycomb lattice of

graphene [53], including graphitic (a boron/nitrogen atom replaces a carbon atom and forms sp^2 bonds with three nearest neighboring carbon atoms, see Fig. 1.8a), pyridinic (a boron/nitrogen atom replaces two carbon atoms and forms sp^2 bonds with two closest carbon atoms and a vacancy in the lattice, see Fig. 1.8b) and nitrilic (nitrogen remains sp^3 bonds with two hydrogen atoms and one carbon atoms in the lattice, see Fig. 1.8c) forms. Moreover, whether the dopants contribute electrons or holes is predicted to depend on the doping form of the dopants. Specifically, in nitrogen doped graphene, graphitic nitrogen dopants contribute electrons into graphene while pyridinic and nitrilic forms donate holes. In fact, there are cases of coexistence of all the doping forms in the same sample in both CVD [55, 56] and post treatment [57, 58] samples. Therefore, a careful characterization of the relation between doping form and its contribution to free charge carrier is necessary to understand the doped graphene material. Second, it is known in semiconductor science that a dopant forms spatially and energetically localized states, and free charge carriers result from the ionization of such localized states. Whether such a classical picture applies in graphene, where the quasi-particles behave as massless Dirac fermions, is another intriguing question. For the sake of simplicity, taking graphitic nitrogen dopants as an example, we can treat such a nitrogen dopant to the first order as a localized positive charge at one atomic site and an extra electron obeying the Dirac band structure. This motivates questions of Coulomb interactions in Dirac fermions, which have been intensively explored in theory [54, 59-62] and recently in experiments [5, 63]. Besides chemically doping with these two neighboring elements of carbon, a second option would be using metal atoms, such as potassium (K) and calcium (Ca). In such cases, the metal atoms physisorb on the surfaces of graphene films, rather than forming any chemical bonds with carbon atoms in the graphene. Nevertheless, the charge transfer from the physisorbed metal atoms can dope graphene with large concentrations of electrons [49, 64, 65], depending on

the coverage of the metal atom adsorption. In particular, a full layer of Ca atoms on graphene can shift the Fermi level as high as the M point where graphene is heavily electron doped, which is hardly reachable by any other doping methods [49].

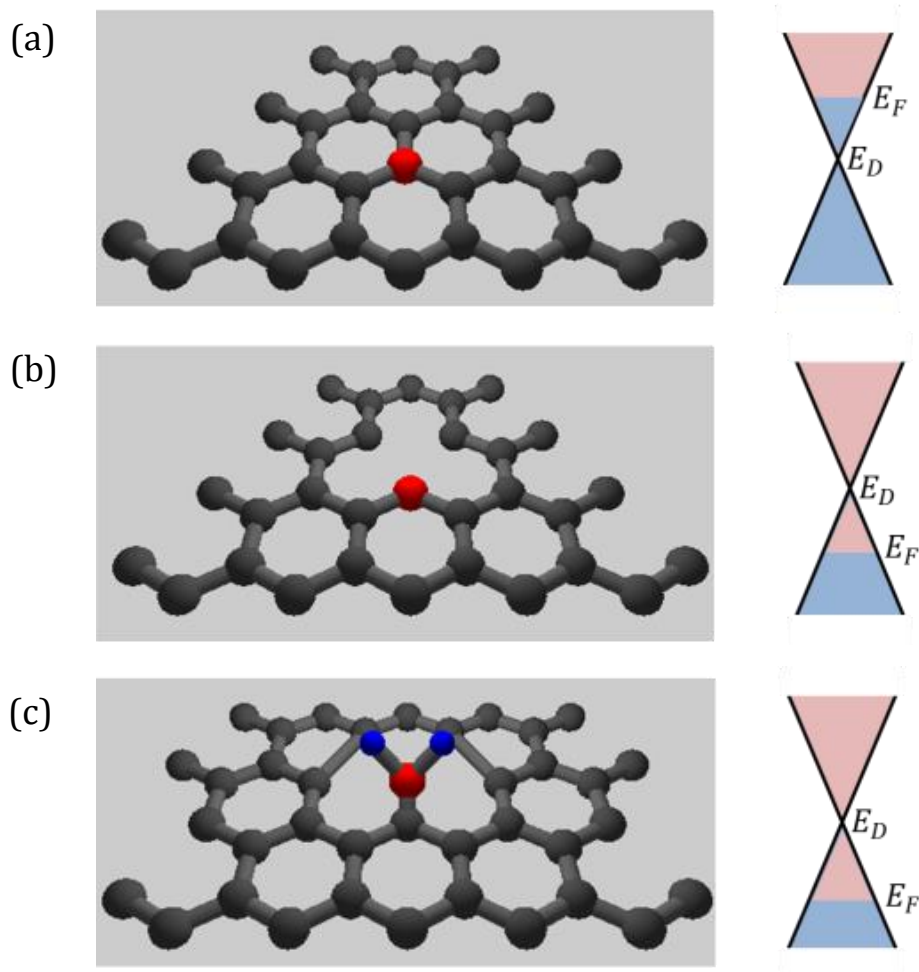


Fig. 1.8 Cartoon models for different doping forms of nitrogen/boron dopants. (a) Graphitic doping form, a single dopant atom substituting a carbon atom in the lattice, predicted to n-dope graphene. (b) Pyridinic doping form, a dopant atom and an adjacent vacancy replacing a unit cell of carbon atoms, predicted to p-dope graphene. (c) Nitrilic doping form, $-NH_2$ group attaching to a carbon atom in graphene, predicted to p-doped graphene even stronger than pyridinic case. Red ball for nitrogen/boron dopant, blue ball for hydrogen atom, and gray one for carbon atom.

Secondly, since the discover of graphene, there have been several methods attempting to open a band gap in the band structure of graphene. The method of chemical doping can be categorized into two groups. The first group aims at deforming the sp^2 network by forming a local sp^3 bonding environment; hydrogen (H) [66] and fluorine (F) [67] atoms are selected to be the proper dopants. In this method, a H/F atom stays on top of a carbon atom and pulls the carbon atom out of graphene plane just enough so as to form sp^3 bonding (see in Fig. 1.9a). In the sp^3 hybridized carbon case, a carbon atom forms tetrahedral geometry with its four neighbors, and each of the four valence electrons from the carbon atom pairs with one electron from each neighboring atom. Such pairs of electrons between two nearest neighbors are strongly localized, just as that in σ bonds of graphene, and this is why sp^3 bonded carbons do not provide conductivity as in, for example, diamond. Due to the sp^3 bonding geometry, two H/F atoms could not bond with two neighboring carbon atoms in a benzene ring, and the second nearest neighbor is the closest choice for a second H/F atom. As a consequence, fully doped graphene has a layer of H/F atoms attaching to one sublattice of carbon atoms on one side of graphene and another layer of H/F atoms binding with the other sublattice of carbons on the other side (as shown in Fig. 1.9b). It has been shown experimentally that fully H doped graphene (graphane) opens up a band gap of at least 450meV , while fully F doped graphene (Fluorographene) is a band insulator with $\sim 3\text{eV}$ band gap. The band gaps are adjustable by tuning the concentration of H/F dopants in graphene. The second category tries to introduce a band gap by breaking AB sublattice symmetry in graphene which is the fundamental origin of the gapless nature at Dirac points. Of course, H/F doped graphene described in the previous method breaks sublattice symmetry, however, it also alters the entire electronic structure, at least locally, around dopants by converting sp^2 bonding into sp^3 bonding, changing the unique electronic properties of graphene. As a comparison to H/F, graphitic N/B doped graphene

perturbs the system least by preserving sp^2 bonding while still breaking the symmetry between the two sublattices (by putting dopants in one sublattice but not the other). Theoretical studies of graphitic N/B doped graphene claim that a band gap opens with the size of the gap depending on the concentration of the dopants but also on the distribution of the dopants [68]. It is most effective to induce sublattice asymmetry when the dopants are in the same sublattice of graphene, and least effective when dopants randomly distribute between the two sublattices. A simple mathematical way of understanding this is as follows: with the asymmetry of Δ between the A and B sublattice, the diagonal terms in the Hamiltonian around the K point is express as

$$\hat{H} = \begin{pmatrix} \Delta & \hbar v_F(ik_x + k_y) \\ \hbar v_F(-ik_x + k_y) & 0 \end{pmatrix} \text{ at K points.} \quad (1.14)$$

The eigenvalues of this Hamiltonian are

$$E(k) = \frac{1}{2}\Delta \pm \sqrt{(\hbar v_F k)^2 + \frac{1}{4}\Delta^2}. \quad (1.15)$$

From the formula for $E(k)$, the gap size equals the sublattice asymmetry Δ . A sketch of such a band structure is shown in Fig. 1.10, with a comparison to that of pristine graphene.

Finally, besides introducing free charge carriers and a band gap in graphene, chemical doping is also applied to modulate other electronic properties of graphene. For examples, a full layer of Ca deposition on graphene can introduce one dimensional charge density waves (CDW) [52], can introduce superconductivity instability from saddle point (M point) singularity [49], or magnetic elements such as Mn [69, 70], Co [71], Ni [72], etc., are predicted theoretically to induce magnetism in graphene.

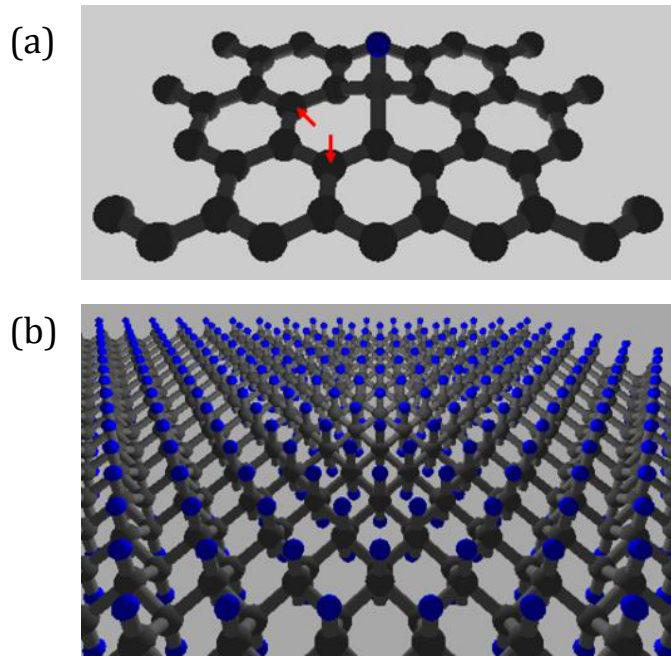


Fig. 1.9 Cartoon model for F-doped graphene; (a) Cartoon model for fluorine (F)- or hydrogen (H)-doped graphene. The F/H atom staying right on top of a carbon atom and pulling it slightly out of the plane of graphene film. The red arrows pointing to two possible closest sites where a second F/H atom can attach on the top surface. (b) Cartoon for fully F-/H-doped graphene. F/H on top surface of graphene occupying one sublattice of the honeycomb lattice while those on bottom surface attaching to the other sublattice. The honeycomb lattice deforms into a zig-zag pattern as shown in the inset.

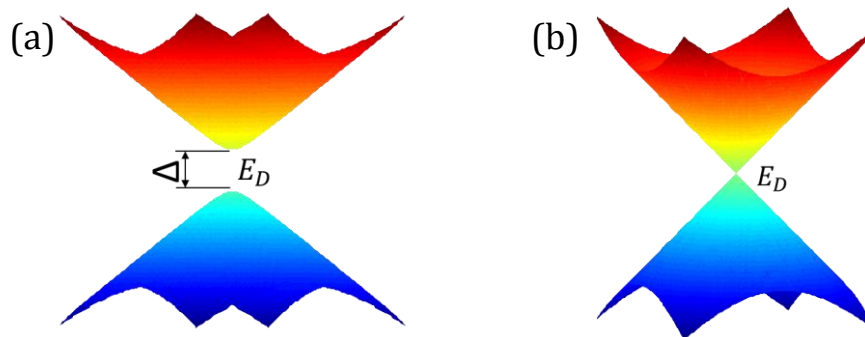


Fig. 1.10 Band gap opening at Dirac point; (a) Sketch of the electronic band structure for Eq.1.15 where sublattice asymmetry is introduced. A band gap of Δ shows at the Dirac point, which equals the strength of asymmetry between the A and B sublattices. (b) Band structure for pristine graphene, showing gapless nature at Dirac Point.

1.3 Scanning Tunneling Microscopy/Spectroscopy

Scanning Tunneling Microscopy/Spectroscopy (STM/S) is a powerful local probe technique that detects topographic features and electronic structures (i.e. local density of states (LDOS)) with sub-pico-meter spatial resolution. This capability of probing topography and LDOS at exactly the same position allows us to correlate any electronic inhomogeneity with structural anomalies such as impurities or defects in the host lattices. In the past decades, this unique ability of STM/S has been used to probe a number of systems, including single crystal metals (Cu(111) [73], Au(111) [74], etc.), semiconductors (Mn-doped GaAs(110) [75, 76], (doped) Si(111) [77, 78], etc.), super-conductors (Ba₂Sr₂Ca₂CuO_{8+δ} [79], pnictide [80, 81], etc.), topological insulators (Bi_{1-x}Sb_x [82, 83], etc.), and graphene (pristine graphene on SiO₂ [84] and on BN [85, 86], B/N [87]-doped graphene, Co-doped graphene [63], Ca-doped graphene [5], etc.)

1.3.1 The Basic Theory of STM/S

The concept of STM/S arises from the phenomenon of quantum mechanical tunneling where an electron with energy E has certain probability P to tunnel through a barrier with energy U even larger than E , as long as there is available states at energy E on the other side of the barrier (cartoon diagram shown in Fig. 1.11a).

In the scenario of tunneling in STM/S, the vacuum between tip and sample acts as the potential barrier and its value typically equals the work function of the tip/sample, $\sim 4 - 5\text{eV}$. Here, we make an assumption that the work function of the tip is almost equals to that of the sample, which is generally true in reality (the work functions of conductors vary within a few tens of meV).

When there is no bias potential V applied between tip and sample, the Fermi level of tip and sample align

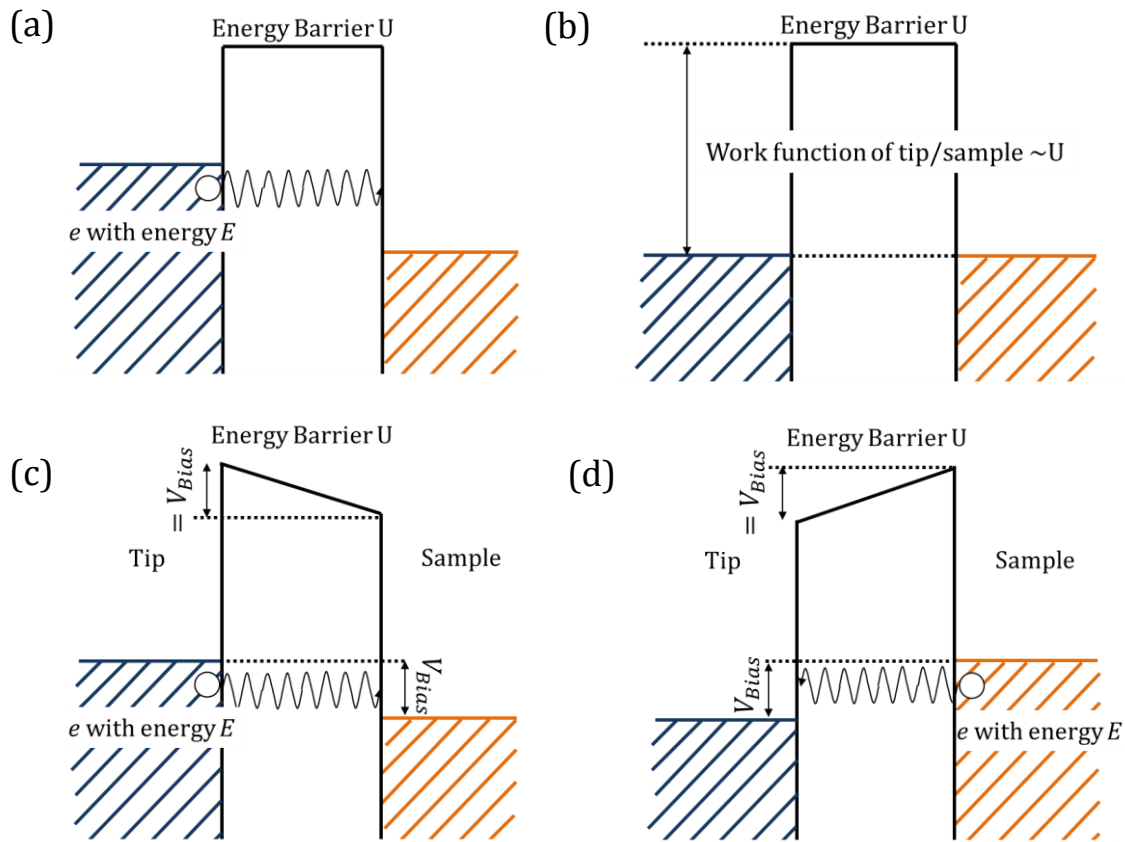


Fig. 1.11 Diagrams for tunneling processes; (a) Diagram for tunneling process, with potential barrier modeled as a square potential. (b) Fermi levels tip and sample aligned without bias voltage applied between the two. (c) and (d) Tunneling processes with bias voltage applied, showing modified potential barrier due to electric field, and tunneling direction depending on the bias polarity.

with each other, and no net tunneling process happens, as shown in Fig. 1.11b. When a positive bias is applied on the sample with respect to the tip, a net tunneling of electron from tip to sample happens at the energy window from E_F to $E_F + V$, as seen in Fig. 1.11c. Vice versa, a net flux of electrons flows from the sample to the tip when negative bias is applied on the sample, as seen in

Fig. 1.11d. Here, it is worth pointing out two assumptions which are typically accepted in modeling the tunneling phenomenon. First, the bias potential between tip and sample should be substantially smaller than the work functions of the tip/sample, normally within the range of $[-1.5\text{eV}, 1.5\text{eV}]$. When the bias potential is greater than the work function, the system enters into the field emission regime, which is different from tunneling regime and may cause damage to sample. Second, since the bias potential is typically much smaller than tunneling barrier, we usually ignore the electronic field effect in the tunneling process, i.e., we still model tunneling barrier as a square potential in Fig. 1.11a rather than a sloped edge in Fig. 1.11c.

With these widely accepted assumptions, one of the most popular theories to model the tunneling phenomenon is Bardeen Tunneling Theory, with a couple of modification by Tersoff and Hamann [88-90]. Under Bardeen theory, the tunneling current is approximated as:

$$I = \frac{2\pi e}{\hbar} \sum_{\mu, \nu} f(E_{\mu}, T) [1 - f(E_{\nu} + eV, T)] |M_{\mu\nu}|^2 \delta(E_{\mu} - E_{\nu}), \quad (1.16)$$

where μ, ν labels the energy states in the tip and the sample respectively, $f(E, T)$ stands for Fermi distribution at temperature T , V is the bias potential applied between tip and sample, and $M_{\mu\nu}$ is the tunneling matrix element between state μ in the tip and state ν in the sample and is given by

$$M_{\mu\nu} = \frac{\hbar^2}{2m} \int \vec{dS} \cdot (\psi_{\mu}^* \nabla \psi_{\nu} - \psi_{\nu}^* \nabla \psi_{\mu}), \quad (1.17)$$

where ψ_{μ} and ψ_{ν} are the wave functions for state μ in the tip and state ν in the sample, and the integral is over the entire tunneling area (its typically determined by the tip size in STM/S). By

introducing the local density of states for both tip and sample, the current formula can be rewritten as

$$I = \frac{4\pi e}{\hbar} \int_{-\infty}^{+\infty} \rho_t(E) \rho_s(E + eV) (f(E) - f(E + eV)) |M|^2 dE, \quad (1.18)$$

where t, s denotes the tip and the sample respectively, and M is the tunneling matrix given by Eq. 1.17. In topography mode, the tip height with respect to sample surface is adjusted (this parameter is hidden in the tunneling matrix element M) so as to maintain a constant current. As seen from the current expression, the apparent height obtained from STM image reflects physical heights (such as the steps in single crystal samples), electronic perturbations as well (such as scattering interference pattern caused by defects), and even differences between species (more discussion in the following Section 1.3.2). In $I(V)$ spectroscopy mode, the current I variation is recorded as a function of the bias voltage V , while the tip is held at a fixed height over the sample surface.

Usually STM/S works in low temperature regime in order to suppress the thermal broadening effects. At low temperatures, the Fermi distribution function could be approximated as a step function,

$$f(E + eV) - f(E) \approx \begin{cases} 1, & E_F - eV < E < E_F \\ 0, & \text{otherwise} \end{cases}. \quad (1.19)$$

With this approximation, the current function in Eq. 1.18 can be simplified as

$$I = \frac{4\pi e}{\hbar} \int_{E_F - eV}^{E_F} \rho_t(E) \rho_s(E + eV) |M|^2 dE. \quad (1.20)$$

Assuming the bias energy is fairly small (as described above), the tunneling matrix element is usually considered to be constant over this narrow energy window of $[E_F - eV, E_F]$, and therefore it can be move out from the integral. Furthermore, a metallic tip usually has a constant DOS over a

broad energy range, and thus $\rho_t(E)$ is eligible to be taken out from the integral as well. As a result of these approximations, the current is now written as

$$I(V) = \frac{4\pi e}{\hbar} \rho_t |M|^2 \int_{E_F}^{E_F + eV} \rho_s(E) dE. \quad (1.21)$$

A derivative of $I(V)$ with respect to V , $\frac{dI}{dV}$, will be directly proportional to the local density of states at energy of $E_F + eV$,

$$\frac{dI}{dV} \propto \rho_s(E_F + eV). \quad (1.22)$$

This is how STS works to probe the LDOS of a sample. In practice, we can either numerically differentiate the $I(V)$ curve, or directly record $\frac{dI}{dV}$ values at various bias voltages with the help of the lock-in technique.

1.3.2 Discussions of Tunneling Matrix and Temperature Effect

As described above, to a first order approximation, the tunneling matrix element $M_{\mu\nu}$ is approximated to be constant over a narrow energy window for a uniform sample surface. However, if the sample contains more than one element which contribute conductive electrons, the tunneling matrix could be sensitive enough to pick up the difference between the elements, despite the similarity of their LDOS. Taking the example of boron, carbon and nitrogen, the p_z orbitals extend differently in space. As shown in Fig. 1.12, p_z orbital of carbon extends further than that of nitrogen, but shorter than that of boron. As a result, the tunneling matrix over these three elements at the same physical height from the surface will follow the order of $M_E(B) > M_E(C) > M_E(N)$. Therefore, in constant current topography mode, the apparent height for boron is highest, and that for carbon is less, and that for nitrogen is the least among the three. Of course, such subtle difference in

apparent height/tunneling matrix is never enough for an accurate element analysis if the elements are not pre-known. Nevertheless, it can be very useful, for example, when assigning whether it is a graphitic boron or nitrogen dopant in graphene films which will be discussed in details in Chapter 2 and 3.

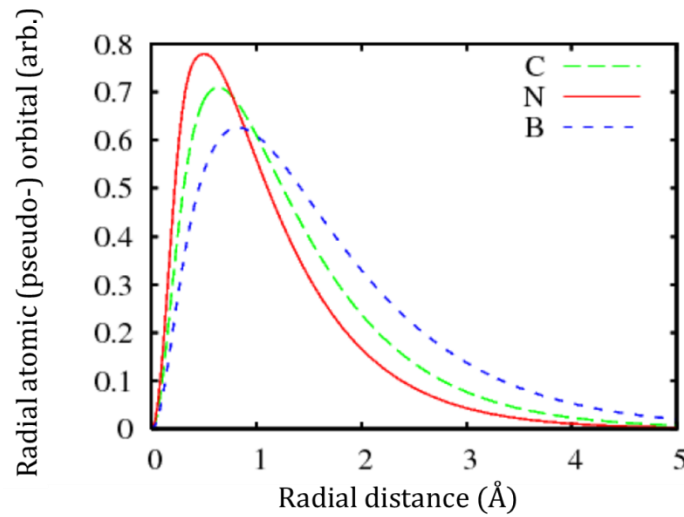


Fig. 1.12 Calculated atomic orbital intensity for boron (B), carbon (C) and nitrogen (N), as a function of radial distance, showing that the orbital of B extends furthest, C less, and N least.

In Section 1.3.1, we assume that the temperature effect in spectroscopy measurements is ignorable for the sake of simplicity. However, this assumption is not always valid, especially when the energy width of a feature is comparable to the thermal energy. In this case,

$$I = \frac{4\pi e}{\hbar} \rho_t |M|^2 \int_{-\infty}^{+\infty} \rho_s(E) (f(E - eV) - f(E)) dE, \quad (1.23)$$

under the assumptions of constant tip LDOS and constant tunneling matrix. Hence,

$$\frac{dI}{dV}(V) = -\frac{4\pi e}{\hbar} \rho_t |M|^2 \int_{-\infty}^{+\infty} \rho_s(E) \frac{df}{dV}(E - eV) dE, \quad (1.24)$$

which is proportional to the convolution between the LDOS of sample and the derivative of Fermi distribution function. From a mathematical perspective, convolution means smoothing a function ($\rho_s(E)$) with another function ($\frac{df}{dV}$), and only the features in the function $\rho_s(E)$ sharper than the width of function $\frac{df}{dV}$ will be strongly affected by the “smoothing” process. At temperature T , the width of $\frac{df}{dV}$ is approximately $\sim kT$. For example, a gap feature in $\frac{dI}{dV}(V)$ is more pronounced at low temperature of 4K, and gets rounded at the gap edge at a higher temperature of 77K.

1.4 Micro-Raman Spectroscopy

1.4.1 Raman Spectroscopy of Graphene

Raman spectroscopy has been proved to be an essential part of graphene research ever since its first report on graphene characterization in 2006 [91]. It has been widely used to determine the number of layers [92-94], the orientations between layers [45, 95], the chirality of edges [96], the quality of a film [92-94], and the effects from functionalization such as doping [97, 98], strain [99-101], magnetic fields [102, 103] and inhomogeneity. All the capabilities mentioned above exploit the four signature peaks in Raman spectroscopy on graphene, namely, D, G, D' and 2D peaks. In this section, I will give a brief description of each peak and its physical origin.

Raman spectroscopy on graphene is resonance Raman spectroscopy because the energy of exciting light matches the energy difference between electronic states in the graphene band structure. Such energy match strongly enhances the transition probability between electronic states and life time at excited energy states, and hence increases the chance of Raman scattering.

The scattering process can be understood with a combination of electronic band structure (shown in Fig. 1.13b) and phonon band structure of graphene (shown in Fig. 1.13a).

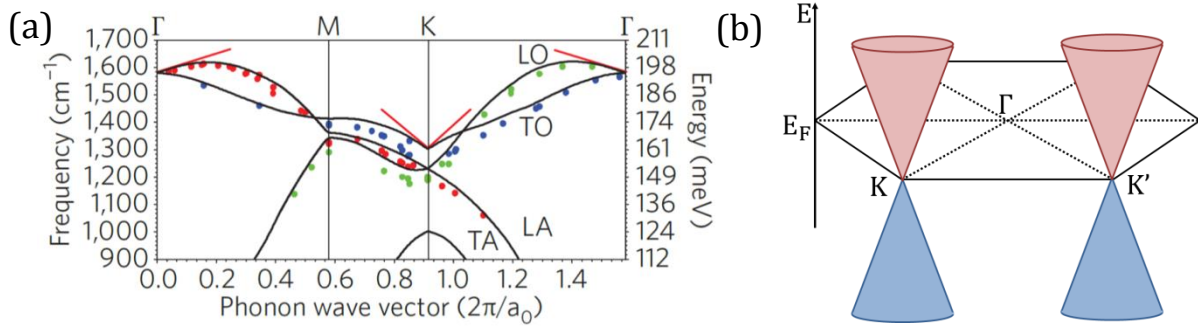


Fig. 1.13 Phonon and electron band structures of monolayer graphene; (a) Phonon spectrum of graphene. Image cited from Ref. [93] (b) Energy spectrum of graphene.

Shown in Fig.1.14a is the scattering process for G peak formation. (1) An electron at (E_0, k_0) adsorbs an incoming photon $(\varepsilon_i, k_i \sim 0)$ and gets excited to state (E_1, k_1) . Due to energy and momentum conservation, $E_1 = E_0 + \varepsilon_i$, and $k_1 \sim k_0$; (2) The excited electron (E_1, k_1) is scattered by a phonon (ε_p, k_p) and gets to a virtual state (E_2, k_2) . Similarly as in step (1), we have $E_2 = E_1 - \varepsilon_p$, and $k_2 = k_1 - k_p$; (3) Finally, the electron drops from virtual state (E_2, k_2) to initial state (E_0, k_0) with an emission of a photon $(\varepsilon_f, k_f \sim 0)$. Here, $E_2 = E_0 + \varepsilon_f$, and $k_2 \sim k_0$. All together, we have $\varepsilon_p = \varepsilon_i - \varepsilon_f$, $k_p \sim 0$. When looking into the phonon spectrum in Fig. 1.13a, a phonon at momentum $k_p \sim 0$ has energy of $\varepsilon_p \sim 1580 \text{ cm}^{-1}$, which is the defined as G peak in Raman scattering. As has been proven experimentally, G peak frequency is sensitive to strain [99-101] and doping [97, 98], while G peak intensity depends on the number of layers [91] and the orientation between layers [45, 95].

Fig.1.14b shows the scattering process for 2D band formation. As we can see from the diagram, two phonons with the same energy and opposite momentums are involved in this

scattering process, with a momentum $\sim K$. Searching in the phonon spectrum, we find the energy of the phonon with a momentum $\sim K$ is $\sim 1350\text{cm}^{-1}$. Therefore, the Raman shift results from this process is twice the phonon energy, $\sim 2700\text{cm}^{-1}$, and this Raman band is called as 2D band. 2D band characterizes the properties of graphene from a few aspects. Its width is a good indicator of number of layers [91] for multilayer graphene, and reflects doping levels [97, 98] as well for monolayer graphene. Its frequency is tied with doping [97, 98], while its intensity is sensitive to impurities either in or on the surface of graphene[92, 93].

In pristine graphene, all the scattering processes are assisted by phonons, and hence only G and 2D peaks show up in Raman spectroscopy. However, any impurities in graphene lattice can act as scatters as well. Therefore, two more peaks, D and D' peaks, show up in the vicinity of any defects in graphene.

In Fig.1.14c, the scattering procedures for D peak is depicted. As we can see, it looks quite similar as the 2D diagram in Fig.1.15b, except one of the two phonon assisted scatterings between the two Dirac cones is replace by an elastic inter-valley scattering from impurities. As a result, the Raman shift equals one phonon energy 1350cm^{-1} which is half of the 2D Raman shift.

Similarly as the D peak, the D' peak originates from one phonon assisted scattering and one impurity assisted scattering, but within one Dirac cone, as shown in Fig.1.14d. The phonon involved has a momentum ≥ 0 , therefore we see an energy slightly higher than the G mode, $\sim 1620\text{cm}^{-1}$.

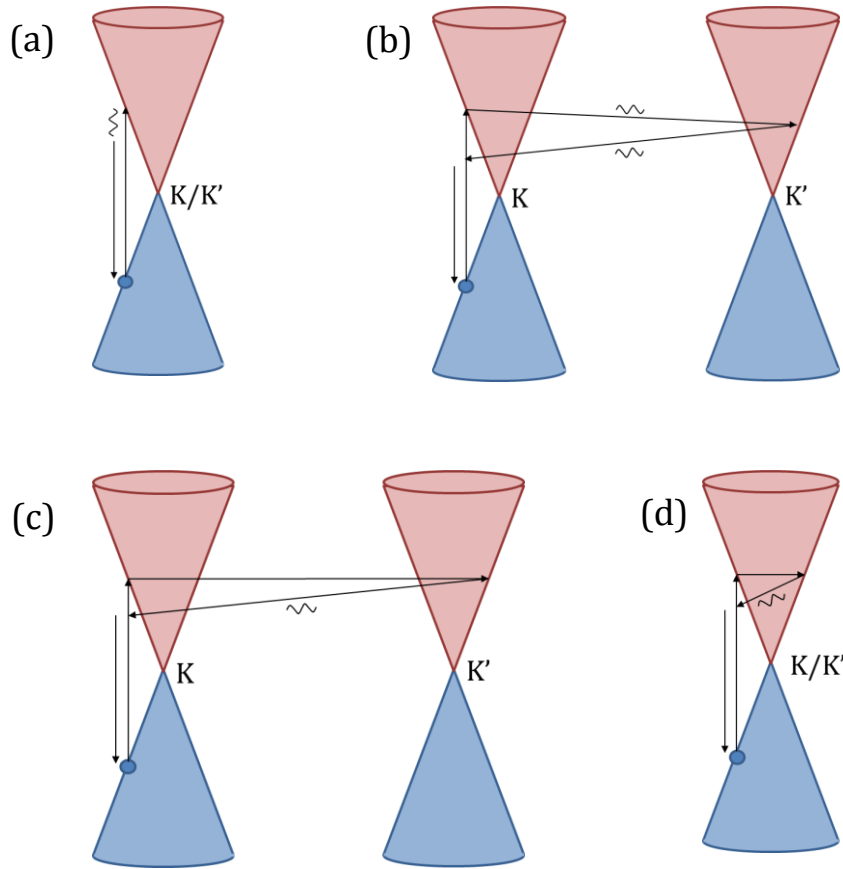


Fig. 1.14 (a) (b) (c) and (d) Diagrams of scattering processes for G, 2D, D and D' bands in Raman spectroscopy of graphene. Arrow with wiggles for phonon assisted scattering, and arrow for electronic scattering. (a) One phonon with zero momentum involved in G band scattering process. (b) Two phonons with $\sim K$ momentum involved in 2D band scattering process. (c) One phonon with $\sim K$ momentum involved in D band scattering. (d) One phonon with $>\sim$ zero momentum in D' band scattering process.

More recently, with better resolution measurement, more Raman peaks have been observed in graphene experimentally [94], including so called D'', D+D'', D+D' and 2D' peaks, as shown in Fig. 1.15. In the upper panel we see the 2D' peak in pristine graphene and in the lower panel we see D+D'', D+D' and 2D' peaks in defected graphene. They have much lower intensity than the four main

peaks described above, and are not as sensitive as the four to perturbations. I am not going to focus on them in this thesis, and detailed information about them can be found in Ref [93].

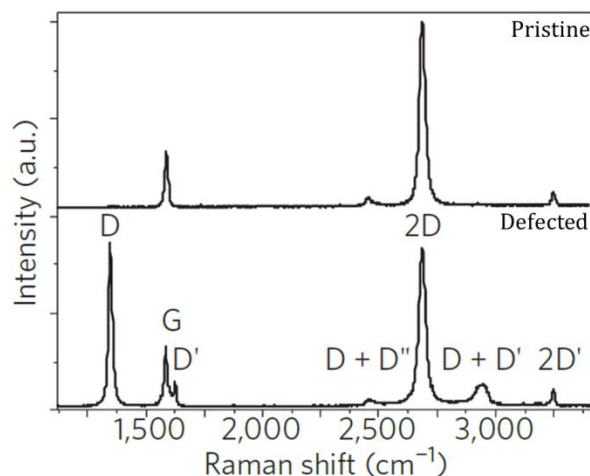


Fig. 1.15 High resolution Raman spectroscopy of pristine graphene (upper panel) and defected graphene (lower panel), with extra peaks D+D'', D+D', 2D' showing up beside the four signature peaks G, 2D, D and D'. Image cited from Ref. [93].

1.5 Outline of the Thesis

After giving the introduction to the basics of (doped) graphene and the main techniques, the rest of this thesis will be organized as following.

Chapter 2 will focus on the synthesis of pristine monolayer graphene films on various copper substrates, and the microscopic characterizations by STM on these as-grown graphene samples. The discovery of uniform growth of monolayer graphene films on copper foil in 2009 generated significant interest in understanding and optimizing the CVD conditions for large area graphene productions. Among all the factors in CVD conditions, copper substrate is the most important one because it not only limits the graphene growth to a monolayer thickness, it also

reduces the cost for fabrications. Along this direction, we studied the influence of the surface structure of copper substrate on the growth of large area monolayer graphene by CVD in ultra-high vacuum (UHV). Using atomic resolution STM, we found that graphene grows primarily in registry with the underlying copper lattice for Cu(111) and Cu(100) single crystals. Graphene on Cu(111) forms a microscopically uniform sheet, and its quality is determined by the presence of grain boundaries where graphene grains, with mismatched orientation or lateral translation, meet. Graphene grown on Cu(100) with the same recipe does not form a uniform sheet but instead displays exposed nano edges, while graphene grown on copper foil under the same condition only forms isolated dendritic patterns. Our results indicate the importance of the copper crystal structure on the microstructure of graphene films produced by CVD.

Production of large scale high-quality pristine graphene is a great step towards the ultimate goal of graphene based electronics. However, two fundamental limits of pristine graphene, absence of both free charge carriers and a band gap, remain to be solved at this stage. Chemical doping has been proved in a good number of systems to be a powerful way to tailor the electronic properties of a host material. Therefore, we introduce either a nitrogen source (NH_3) or a boron source (B_2H_6) during the graphene CVD growth process, and as a result, achieve nitrogen- or boron-doped graphene.

In Chapters 3 and 4, I will briefly describe the synthesis of doped graphene films on copper foil substrates in a CVD furnace, and mainly focus on the topographic and electronic characterizations of as-grown nitrogen- (Chapter 3) and boron- (Chapter 4)doped graphene at the microscopic scale. As theory has predicted, different doping forms of nitrogen/boron dopants will affect the electronic structure of graphene in different ways. Prior to our experiments, macroscopic

characterizations on nitrogen-doped graphene have shown the coexistence of graphitic and pyridinic doping forms, and no direct measurements have ever been done to correlate the doping form and its electronic properties. In Chapter 3, we identify that more than 90% of the dopants in nitrogen doped graphene are single graphitic dopants. Furthermore, we simultaneously measured the dopant concentration and doping level at the same local area, and found each graphitic nitrogen dopant contributes ~ 0.5 electron to graphene system. Finally, we examined the perturbation in electronic band structure in the vicinity of nitrogen dopants, and find such disturbances to be within $\sim 7\text{\AA}$ from the dopant site. In Chapter 4, we show that only $\sim 80\%$ of the impurities are graphitic boron dopants while the remaining defects are associated with stone-wales defects. Graphitic boron dopants, like nitrogen, donate ~ 0.5 hole carrier to the graphene sheet per boron dopant and perturb the electronic structure as locally as $< 1\text{nm}$. Density functional theory calculations indicate that boron dopants interact strongly with the underlying substrate while nitrogen dopants do not. Such local bonding differences between graphitic boron and nitrogen dopants lead to large scale differences in dopant distribution. The distribution of dopants is observed to be completely random in the case of boron, while nitrogen displays strong sublattice clustering. This difference in dopant distribution between sublattices theoretically will result in different degrees of sublattice symmetry breaking, and hence different ways of opening a band gap at Dirac points. The other 20% structural defects create local electronic resonances and cause electronic scattering, but do not electronically dope graphene films.

Large area CVD graphene inevitably contains a good number of grain boundaries and these grain boundaries are the main factor in determining the transport properties of pristine graphene. What are their influences in chemically doped graphene films is the question we would like to answer in Chapter 5. Chapter 5 combines the measurements of Micro-Raman Spectroscopy and

STM topography, to show the nitrogen distribution within grains and around grain boundaries. Typically in three dimensional polycrystals, the impurities in them tend to migrate to the grain boundaries and subsequently modify the electronic structures around the grain boundaries. However, our experiments on the two dimensional nitrogen-doped graphene demonstrate that, in contrast to three-dimensional polycrystals, the graphitic nitrogen dopants in doped graphene polycrystals avoid grain boundaries and edges over micron length scales while distributing uniformly in the interior of each grain. We further show that this phenomenon is independent of the details of the growth procedure (such as temperature, pressure, substrate, and precursor) and instead a result of the bonding and coordination of individual nitrogen atoms in the carbon lattice.

1.6 References

1. Novoselov, K.S., et al., *Electric Field Effect in Atomically Thin Carbon Films*. Science, 2004. 306(5696): p. 666-669.
2. Zhang, Y., et al., *Experimental observation of the quantum Hall effect and Berry's phase in graphene*. Nature, 2005. 438(7065): p. 201-204.
3. Novoselov, K.S., et al., *Two-dimensional gas of massless Dirac fermions in graphene*. Nature, 2005. 438(7065): p. 197-200.
4. Young, A.F. and P. Kim, *Quantum interference and Klein tunnelling in graphene heterojunctions*. Nat Phys, 2009. 5(3): p. 222-226.
5. Wang, Y., et al., *Observing Atomic Collapse Resonances in Artificial Nuclei on Graphene*. Science, 2013. 340(6133): p. 734-737.
6. Liu, H., et al., *Photochemical Reactivity of Graphene*. Journal of the American Chemical Society, 2009. 131(47): p. 17099-17101.
7. Dreyer, D.R., et al., *The chemistry of graphene oxide*. Chemical Society Reviews, 2010. 39(1): p. 228-240.
8. Rodriguez-Perez, L., M.a.A. Herranz, and N. Martin, *The chemistry of pristine graphene*. Chemical Communications, 2013. 49(36): p. 3721-3735.
9. Novoselov, K.S., et al., *A roadmap for graphene*. Nature, 2012. 490(7419): p. 192-200.
10. Schwierz, F., *Graphene transistors*. Nat Nano, 2010. 5(7): p. 487-496.
11. Avouris, P., *Graphene: Electronic and Photonic Properties and Devices*. Nano Letters, 2010. 10(11): p. 4285-4294.
12. Wallace, P.R., *The Band Theory of Graphite*. Physical Review, 1947. 71(9): p. 622-634.
13. Slonczewski, J.C. and P.R. Weiss, *Band Structure of Graphite*. Physical Review, 1958. 109(2): p. 272-279.

14. Lee, C., et al., *Measurement of the Elastic Properties and Intrinsic Strength of Monolayer Graphene*. Science, 2008. 321(5887): p. 385-388.
15. Lee, G.-H., et al., *High-Strength Chemical-Vapor-Deposited Graphene and Grain Boundaries*. Science, 2013. 340(6136): p. 1073-1076.
16. Castro Neto, A.H., et al., *The electronic properties of graphene*. Reviews of Modern Physics, 2009. 81(1): p. 109-162.
17. Dirac, P. *A new basis for cosmology*. in *Proc. R. Soc. Lond., Ser. A*. 1938.
18. Geim, A.K. and K.S. Novoselov, *The rise of graphene*. Nat Mater, 2007. 6(3): p. 183-191.
19. Geim, A.K., *Graphene: Status and Prospects*. Science, 2009. 324(5934): p. 1530-1534.
20. Neto, A.H.C. and K. Novoselov, *New directions in science and technology: two-dimensional crystals*. Reports on Progress in Physics, 2011. 74(8): p. 082501.
21. Singh, V., et al., *Graphene based materials: Past, present and future*. Progress in Materials Science, 2011. 56(8): p. 1178-1271.
22. Berger, C., et al., *Ultrathin Epitaxial Graphite: 2D Electron Gas Properties and a Route toward Graphene-based Nanoelectronics*. The Journal of Physical Chemistry B, 2004. 108(52): p. 19912-19916.
23. Hass, J., et al., *Why Multilayer Graphene on 4H-SiC(0001[over]) Behaves Like a Single Sheet of Graphene*. Physical Review Letters, 2008. 100(12): p. 125504.
24. Yike, H., et al., *Structured epitaxial graphene: growth and properties*. Journal of Physics D: Applied Physics, 2012. 45(15): p. 154010.
25. Riedl, C., C. Coletti, and U. Starke, *Structural and electronic properties of epitaxial graphene on SiC(0001): a review of growth, characterization, transfer doping and hydrogen intercalation*. Journal of Physics D: Applied Physics, 2010. 43(37): p. 374009.
26. Guisinger, N.P., et al. *Atomic-scale investigation of graphene formation on 6H-SiC(0001)*. 2008. Seattle, Washington (USA): AVS.
27. Kim, K.S., et al., *Large-scale pattern growth of graphene films for stretchable transparent electrodes*. Nature, 2009. 457(7230): p. 706-710.
28. Sutter, P., J.T. Sadowski, and E. Sutter, *Graphene on Pt(111): Growth and substrate interaction*. Physical Review B, 2009. 80(24): p. 245411.
29. Vázquez de Parga, A.L., et al., *Periodically Rippled Graphene: Growth and Spatially Resolved Electronic Structure*. Physical Review Letters, 2008. 100(5): p. 056807.
30. Johann, C., et al., *Growth of graphene on Ir(111)*. New Journal of Physics, 2009. 11(2): p. 023006.
31. Sicot, M., et al., *Nucleation and growth of nickel nanoclusters on graphene Moir[e-acute] on Rh(111)*. Applied Physics Letters, 2010. 96(9): p. 093115-3.
32. Kwon, S.-Y., et al., *Growth of Semiconducting Graphene on Palladium*. Nano Letters, 2009. 9(12): p. 3985-3990.
33. Li, X., et al., *Large-Area Synthesis of High-Quality and Uniform Graphene Films on Copper Foils*. Science, 2009. 324(5932): p. 1312-1314.
34. Li, X., et al., *Evolution of Graphene Growth on Ni and Cu by Carbon Isotope Labeling*. Nano Letters, 2009. 9(12): p. 4268-4272.
35. Bhaviripudi, S., et al., *Role of Kinetic Factors in Chemical Vapor Deposition Synthesis of Uniform Large Area Graphene Using Copper Catalyst*. Nano Letters, 2010. 10(10): p. 4128-4133.
36. Wofford, J.M., et al., *Graphene Islands on Cu Foils: The Interplay between Shape, Orientation, and Defects*. Nano Letters, 2010. 10(12): p. 4890-4896.

37. Zhao, L., et al., *Influence of copper crystal surface on the CVD growth of large area monolayer graphene*. Solid State Communications, 2011. 151(7): p. 509-513.
38. Han, G.H., et al., *Influence of Copper Morphology in Forming Nucleation Seeds for Graphene Growth*. Nano Letters, 2011. 11(10): p. 4144-4148.
39. Huang, P.Y., et al., *Grains and grain boundaries in single-layer graphene atomic patchwork quilts*. Nature, 2011. 469(7330): p. 389-392.
40. Kim, K., et al., *Grain Boundary Mapping in Polycrystalline Graphene*. ACS Nano, 2011. 5(3): p. 2142-2146.
41. Yazyev, O.V. and S.G. Louie, *Electronic transport in polycrystalline graphene*. Nat Mater, 2010. 9(10): p. 806-809.
42. Tsen, A.W., et al., *Tailoring Electrical Transport Across Grain Boundaries in Polycrystalline Graphene*. Science, 2012. 336(6085): p. 1143-1146.
43. Li, X., et al., *Large-Area Graphene Single Crystals Grown by Low-Pressure Chemical Vapor Deposition of Methane on Copper*. Journal of the American Chemical Society, 2011. 133(9): p. 2816-2819.
44. Zhang, Y., et al., *Direct observation of a widely tunable bandgap in bilayer graphene*. Nature, 2009. 459(7248): p. 820-823.
45. Havener, R.W., et al., *Angle-Resolved Raman Imaging of Interlayer Rotations and Interactions in Twisted Bilayer Graphene*. Nano Letters, 2012. 12(6): p. 3162-3167.
46. Kim, D., et al., *Magnetization reversal and spintronics of Ni/Graphene/Co induced by doped graphene*. Applied Physics Letters, 2013. 102(11): p. 112403-4.
47. Zuo, Z., et al., *Peculiarly strong room-temperature ferromagnetism from low Mn-doping in ZnO grown by molecular beam epitaxy*. AIP Advances, 2013. 3(3): p. 032110-16.
48. Profeta, G., M. Calandra, and F. Mauri, *Phonon-mediated superconductivity in graphene by lithium deposition*. Nat Phys, 2012. advance online publication.
49. McChesney, J.L., et al., *Extended van Hove Singularity and Superconducting Instability in Doped Graphene*. Physical Review Letters, 2010. 104(13): p. 136803.
50. Tao, C., et al., *Spatially resolving edge states of chiral graphene nanoribbons*. Nat Phys, 2011. 7(8): p. 616-620.
51. Avdoshenko, S.M., et al., *Topological Signatures in the Electronic Structure of Graphene Spirals*. Sci. Rep., 2013. 3.
52. Rahnejat, K.C., et al., *Charge density waves in the graphene sheets of the superconductor CaC₆*. Nat Commun, 2011. 2: p. 558.
53. Zheng, B., P. Hermet, and L. Henrard, *Scanning Tunneling Microscopy Simulations of Nitrogen- and Boron-Doped Graphene and Single-Walled Carbon Nanotubes*. ACS Nano, 2010. 4(7): p. 4165-4173.
54. Pereira, V.M., J. Nilsson, and A.H. Castro Neto, *Coulomb Impurity Problem in Graphene*. Physical Review Letters, 2007. 99(16): p. 166802.
55. Wei, D., et al., *Synthesis of N-Doped Graphene by Chemical Vapor Deposition and Its Electrical Properties*. Nano Letters, 2009. 9(5): p. 1752-1758.
56. Schiros, T., et al., *Connecting Dopant Bond Type with Electronic Structure in N-Doped Graphene*. Nano Letters, 2012. 12(8): p. 4025-4031.
57. Wang, H., T. Maiyalagan, and X. Wang, *Review on Recent Progress in Nitrogen-Doped Graphene: Synthesis, Characterization, and Its Potential Applications*. ACS Catalysis, 2012. 2(5): p. 781-794.

58. Lin, Y.-C., C.-Y. Lin, and P.-W. Chiu, *Controllable graphene N-doping with ammonia plasma*. Applied Physics Letters, 2010. 96(13): p. 133110-3.
59. Adam, S., et al., *Theory of charged impurity scattering in two-dimensional graphene*. Solid State Communications, 2009. 149(27–28): p. 1072-1079.
60. Biswas, R.R., S. Sachdev, and D.T. Son, *Coulomb impurity in graphene*. Physical Review B, 2007. 76(20): p. 205122.
61. Terekhov, I.S., et al., *Screening of Coulomb Impurities in Graphene*. Physical Review Letters, 2008. 100(7): p. 076803.
62. Shytov, A.V., M.I. Katsnelson, and L.S. Levitov, *Atomic Collapse and Quasi-Rydberg States in Graphene*. Physical Review Letters, 2007. 99(24): p. 246802.
63. Wang, Y., et al., *Mapping Dirac quasiparticles near a single Coulomb impurity on graphene*. Nat Phys, 2012. 8(9): p. 653-657.
64. Ohta, T., et al., *Controlling the Electronic Structure of Bilayer Graphene*. Science, 2006. 313(5789): p. 951-954.
65. Bostwick, A., et al., *Quasiparticle dynamics in graphene*. Nat Phys, 2007. 3(1): p. 36-40.
66. Elias, D.C., et al., *Control of Graphene's Properties by Reversible Hydrogenation: Evidence for Graphane*. Science, 2009. 323(5914): p. 610-613.
67. Cheng, S.H., et al., *Reversible fluorination of graphene: Evidence of a two-dimensional wide bandgap semiconductor*. Physical Review B, 2010. 81(20): p. 205435.
68. Jindal, P.R.V.K., *Designing band gap of graphene by B and N dopant atoms*. arXiv, 2013. 1209(5228).
69. Gorjizadeh, N. and Y. Kawazoe, *Magnetic Properties of Mn Doped Armchair Graphene Nanoribbon*. MATERIALS TRANSACTIONS, 2008. 49(11): p. 2445-2447.
70. Wu, M., C. Cao, and J.Z. Jiang, *Electronic structure of substitutionally Mn-doped graphene*. New Journal of Physics, 2010. 12(6): p. 063020.
71. Santos, E.J.G., D. Sánchez-Portal, and A. Ayuela, *Magnetism of substitutional Co impurities in graphene: Realization of single π vacancies*. Physical Review B, 2010. 81(12): p. 125433.
72. Santos, E.J.G., et al., *Switching on magnetism in Ni-doped graphene: Density functional calculations*. Physical Review B, 2008. 78(19): p. 195420.
73. Crommie, M.F., C.P. Lutz, and D.M. Eigler, *Imaging standing waves in a two-dimensional electron gas*. Nature, 1993. 363(6429): p. 524-527.
74. Chen, W., et al., *Scanning Tunneling Microscopy Observation of an Electronic Superlattice at the Surface of Clean Gold*. Physical Review Letters, 1998. 80(7): p. 1469-1472.
75. Kitchen, D., et al., *Atom-by-atom substitution of Mn in GaAs and visualization of their hole-mediated interactions*. Nature, 2006. 442(7101): p. 436-439.
76. Kitchen, D., A. Richardella, and A. Yazdani, *Spatial Structure of a Single Mn Impurity State on GaAs (110) Surface*. Journal of Superconductivity, 2005. 18(1): p. 23-28.
77. Owman, F. and P. Mårtensson, *STM study of Si(111)1 \times 1-H surfaces prepared by in situ hydrogen exposure*. Surface Science, 1994. 303(3): p. L367-L372.
78. Li, L., et al., *STM study of C₂H₂ adsorption on Si(001)*. Physical Review B, 1997. 56(8): p. 4648-4655.
79. Gomes, K.K., et al., *Visualizing pair formation on the atomic scale in the high-T_c superconductor Bi₂Sr₂CaCu₂O₈+[dgr]*. Nature, 2007. 447(7144): p. 569-572.

80. Chuang, T.-M., et al., *Nematic Electronic Structure in the “Parent” State of the Iron-Based Superconductor $\text{Ca}(\text{Fe}_{1-x}\text{Co}_x)_2\text{As}_2$* . Science, 2010. 327(5962): p. 181-184.
81. Allan, M.P., et al., *Anisotropic Energy Gaps of Iron-Based Superconductivity from Intraband Quasiparticle Interference in LiFeAs* . Science, 2012. 336(6081): p. 563-567.
82. Seo, J., et al., *Transmission of topological surface states through surface barriers*. Nature, 2010. 466(7304): p. 343-346.
83. Jia, S., et al., *Defects and high bulk resistivities in the Bi-rich tetradymite topological insulator $\text{Bi}_{2+x}\text{Te}_{2-x}\text{Se}$* . Physical Review B, 2012. 86(16): p. 165119.
84. Zhang, Y., et al., *Origin of spatial charge inhomogeneity in graphene*. Nat Phys, 2009. 5(10): p. 722-726.
85. Decker, R.g., et al., *Local Electronic Properties of Graphene on a BN Substrate via Scanning Tunneling Microscopy*. Nano Letters, 2011. 11(6): p. 2291-2295.
86. Xue, J., et al., *Scanning tunnelling microscopy and spectroscopy of ultra-flat graphene on hexagonal boron nitride*. Nat Mater, 2011. 10(4): p. 282-285.
87. Zhao, L., et al., *Visualizing Individual Nitrogen Dopants in Monolayer Graphene*. Science, 2011. 333(6045): p. 999-1003.
88. Tersoff, J. and D.R. Hamann, *Theory and Application for the Scanning Tunneling Microscope*. Physical Review Letters, 1983. 50(25): p. 1998-2001.
89. Tersoff, J. and D.R. Hamann, *Theory of the scanning tunneling microscope*. Physical Review B, 1985. 31(2): p. 805-813.
90. Bardeen, J., *Tunnelling from a Many-Particle Point of View*. Physical Review Letters, 1961. 6(2): p. 57-59.
91. Ferrari, A.C., et al., *Raman Spectrum of Graphene and Graphene Layers*. Physical Review Letters, 2006. 97(18): p. 187401.
92. Ferrari, A.C., *Raman spectroscopy of graphene and graphite: Disorder, electron–phonon coupling, doping and nonadiabatic effects*. Solid State Communications, 2007. 143(1–2): p. 47-57.
93. Malard, L.M., et al., *Raman spectroscopy in graphene*. Physics Reports, 2009. 473(5–6): p. 51-87.
94. Ferrari, A.C. and D.M. Basko, *Raman spectroscopy as a versatile tool for studying the properties of graphene*. Nat Nano, 2013. 8(4): p. 235-246.
95. Kim, K., et al., *Raman Spectroscopy Study of Rotated Double-Layer Graphene: Misorientation-Angle Dependence of Electronic Structure*. Physical Review Letters, 2012. 108(24): p. 246103.
96. You, Y., et al., *Edge chirality determination of graphene by Raman spectroscopy*. Applied Physics Letters, 2008. 93(16): p. 163112-3.
97. Yan, J., et al., *Electric Field Effect Tuning of Electron-Phonon Coupling in Graphene*. Physical Review Letters, 2007. 98(16): p. 166802.
98. DasA, et al., *Monitoring dopants by Raman scattering in an electrochemically top-gated graphene transistor*. Nat Nano, 2008. 3(4): p. 210-215.
99. Mohiuddin, T.M.G., et al., *Uniaxial strain in graphene by Raman spectroscopy: G peak splitting, Grüneisen parameters, and sample orientation*. Physical Review B, 2009. 79(20): p. 205433.
100. Ni, Z.H., et al., *Uniaxial Strain on Graphene: Raman Spectroscopy Study and Band-Gap Opening*. ACS Nano, 2008. 2(11): p. 2301-2305.
101. Huang, M., et al., *Phonon softening and crystallographic orientation of strained graphene studied by Raman spectroscopy*. Proceedings of the National Academy of Sciences, 2009. 106(18): p. 7304-7308.

102. Pinczuk, S.G.J.Y.V.P.A., *Raman Spectroscopy of magneto-phonon resonances in graphene and graphite*. arXiv, 2012. 1204(5081).
103. Faugeras, C., et al., *Effect of a magnetic field on the two-phonon Raman scattering in graphene*. Physical Review B, 2010. 81(15): p. 155436.

Chapter 2

Influence of Cu Crystal Surface on CVD Graphene Growth

2.1 Overview of CVD Graphene Growth on Cu Substrates

The successful growth of large-area, few layer graphene films [1-4] has the potential to revolutionize applications of graphene in electronic, mechanic and photonic devices [5-8]. In the past few years, chemical vapor deposition (CVD) growth has been used to produce such thin-layer films on a number of transition metal substrates, including Cu [1, 9], Ni[2, 10, 11], Ru [12-15], Ir [16-19],.... Among these transition metals, Cu substrate is of especial interest, because of the low cost of Cu as substrates and, perhaps more importantly, the fact that the catalytic growth of graphene on Cu substrates is self-limiting and mostly (>90%) results in formation of single layer graphene [1]. Understanding the impact of Cu substrate on graphene films is thus crucial to the quest of achieving high quality, large-area, single layer graphene.

2.1.1 Standard Recipe for CVD Graphene Growth on Cu Substrates

The report on successful growths of large-area monolayer graphene films on Cu foils [1] sets up the protocol recipe for graphene growth on Cu foil substrates in a CVD furnace. In Fig. 2.1, the diagram shows a standard setup for CVD graphene growth on Cu, – a furnace, a mechanical pump, a quartz tube and three ultra-high purity gases including Methane (CH_4), Hydrogen (H_2) and Argon (Ar). A typical procedure for growing graphene on Cu foil is described as follows: (1) Place a piece of Cu foil

in the middle of the quartz tube, and start pumping the system afterwards. (2) Rise up the temperature of the furnace to 1000°C at the position to the left of the Cu foil, and then move the hot furnace to the position of Cu foil. (3) Add in H_2 gas at a flow rate of 2 sccm to clean the Cu foil at 1000°C. (3) Add in CH_4 gas at a flow rate of 35 sccm to grow graphene. Note the ratio between H_2 and CH_4 is chosen to be $\sim 1:17$ in Ref [1]. (4) Shut down both H_2 and CH_4 gases and cool down the system in Ar environment. This recipe not only has been well adopted by a great number of research groups [20-26], but also has been scaled up to the industry level for mass productions of monolayer graphene films [4].

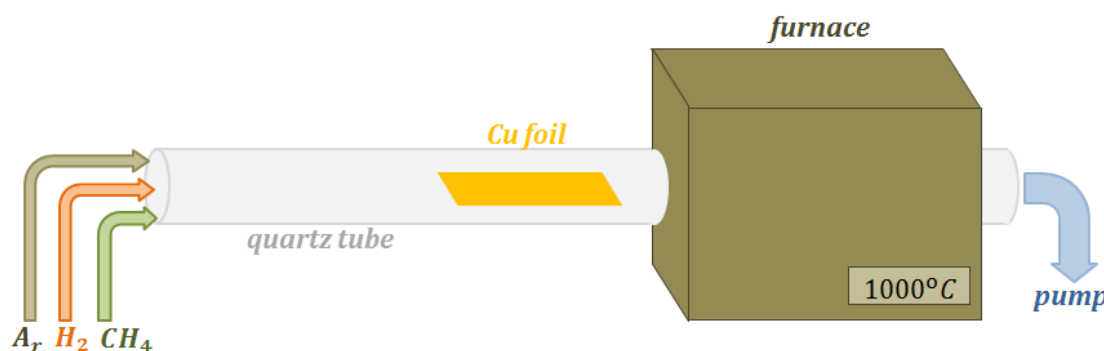


Fig. 2.1 Cartoon for the CVD graphene growth setup, including three precursor gases, a quartz tube, a piece of Cu foil, a furnace and a mechanical pump.

2.1.2 Modified Recipes for CVD Graphene Growth on Cu substrates

Although the recipe in Ref. [1] is capable of producing large-area, high quality, polycrystalline monolayer graphene, the quest of achieving even better quality never stops, neither does the curiosity of learning the growth mechanism. In fact, there are quite a number of parameters that are tunable during growth, including overall pressure, ratio between H_2 and CH_4 , geometry of Cu foil, precursors, temperature, and crystallinity of Cu substrate.

It has been proved that H_2 , rather than CH_4 , dictates the size and shape of graphene grains [27]. By increasing the ratio of H_2 to CH_4 during CVD growth, individual grains of graphene are cultivated into a hexagonal shape and their sizes are noticeably increased (from $\sim 3\text{-}5\mu\text{m}$ to $\sim 20\mu\text{m}$), even though at a cost of much slower growth speed [27]. Besides the ratio between H_2 and CH_4 , decreasing the overall growth pressure, together with creating a stable environment for growth, contributes to increase the grain size of graphene. Two manners have been reported to achieve ultra-large grain size (typically in order of a few hundreds μm) graphene in stable, low pressure environment. One is to fold a piece of Cu foil into pita-pocket geometry so that it creates a steady atmosphere inside the pocket [28]. The other way is to put a small quartz tube with one end sealed inside the growth quartz tube and keep the open side of the small tube facing the flow of gases [29]. In this way, the trapped gases inside the small quartz tube will be stabilized. The former method has been widely applied to produce large grain size graphene [24-26]

A second alternative to achieve well-shaped, large grain size graphene is by using Benzene, instead of a mixture of H_2 and CH_4 , as the precursor for growth [30, 31]. Furthermore, due to the structural similarity between Benzene and graphene, high quality graphene films can be grown at a relatively low temperature of $\sim 300^\circ\text{C}$, compared with at least $>800^\circ\text{C}$ for H_2 and CH_4 as precursors. From the perspective of saving energies and costs, it is an attractive recipe to put into practice. However, the liquid form of Benzene requires more cares to handle with.

Finally, the influence of Cu substrate crystallinity on graphene growth is also a popular aspect to investigate [32-34], and this is where we put our effects in. Simply imaging that the Cu foil used for CVD graphene growth is neither pure (98% purity) nor smooth (facets and grains in polycrystalline Cu foil), we would naturally wonder how an atomic-thick layer of film may grow on

top of it with high quality. Under such a motivation, we performed atomic-scale STM studies of graphene films grown on Cu(111), Cu(100), and polycrystalline Cu with the same modified recipe (described in Section 2.2) in ultra-high vacuum (UHV).

2.2 Sample Preparation in UHV

2.2.1 Preparations of Cu Substrates

The crystal structure for Cu single crystal is Face Centered Cubic (FCC) (Fig. 2.2a). If the bulk is cut normal to a crystalline direction of (x, y, z) , the exposed surface is usually labeled as Cu(xyz). The surface structure depends on the crystallinity of the surface. Here, we choose two most common Cu surfaces, Cu(111) and Cu(100), to grow graphene on. As shown in Fig. 2.2b, the Cu(111) surface structure is a hexagonal lattice with a lattice constant of 2.55\AA , and the stacking order between the layers follows ABCABC.... In Fig. 2.2c, it shows the square lattice of Cu(100) surface, with a lattice constant of 2.55\AA . The single crystals that we used in our experiments are pre-cut at desired crystalline orientations. Both of the single crystals are disks of 1.5mm thick and 9mm in diameter.

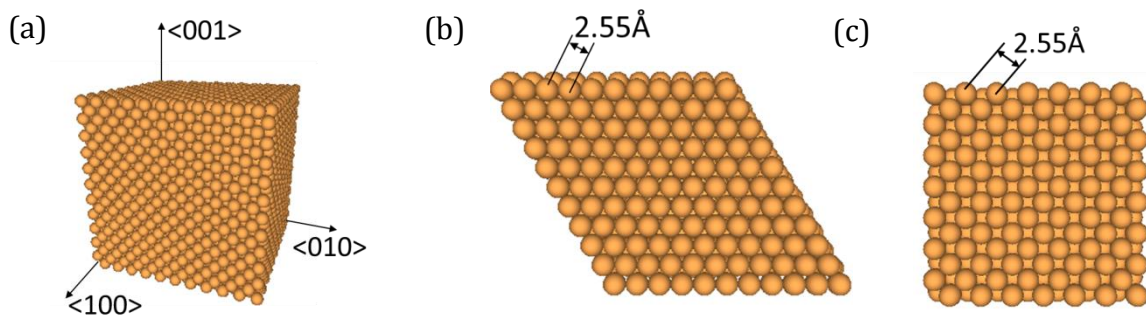


Fig. 2.2 (a) FCC structure for Cu single crystal; (b) Hexagonal lattice of Cu(111) surface, with lattice constant of $a = 2.55\text{\AA}$; (c) Square lattice of Cu(100) surface, with lattice constant of $a = 2.55\text{\AA}$

A standard way to prepare clean surfaces of single crystals in UHV is by repeated cycles of Ar^+ ion sputtering to remove the surface contaminants and subsequently annealing to flatten the surfaces. Shown in Fig. 2.3a is a typical Cu(111) surface with sputtering but not annealing. Sputtering (at Ar pressure of 5×10^{-6} torr, accelerating voltage of 1.5kV, and emission current of 20mA for 15mins) creates mountain/valley-like features over the Cu(111) surface, and these features are formed by layers of Cu terraces as evidenced by the steps and step heights of $\sim 2\text{\AA}$ in the line profile in inset of Fig. 2.3a. After a subsequent annealing (at 650°C for 15mins) after sputtering, the surface rearrange into large flat terraces so as to minimize the surface energy. Shown in Fig. 2.3b is a typically clean Cu(111) surfaces that we usually obtain. However, if the surface contains a good amount of impurities, it is usually difficult to get as clean and large terraces as in Fig. 2.3b. We will show more results of this case in session 2.2.2 when we deposit a lot of carbons on the surface.

Following the standard recipe describe in last paragraph, we prepared both Cu(111) and Cu(100) surfaces prior to the growth of graphene on them. Over a large scale ($\sim 300\text{nm}$), both surfaces show terraces as that in Fig. 2.3b. However, when zooming into a smaller scale, we observe atomic size depletions on Cu(111) surface (Fig. 2.3c and line profile in Fig. 2.3d) but not on Cu(100) surface. Such depletions originate from the sulfur (S) impurities in Cu single crystals[35], and should be in both Cu(111) and Cu(100). The S impurities stand out only on Cu(111) surface, because they act as scattering centers for the two dimensional electron gas (2DEG) of Cu(111) surface states [35], but no surface states are present on Cu(100) surface. A low bias ($V_{\text{bias}}=0.1\text{eV}$) topography on Cu(111) surface displays ripple-like features surrounding these defects as a consequence of quantum interferences from scattering, as shown in Fig. 2.3c.

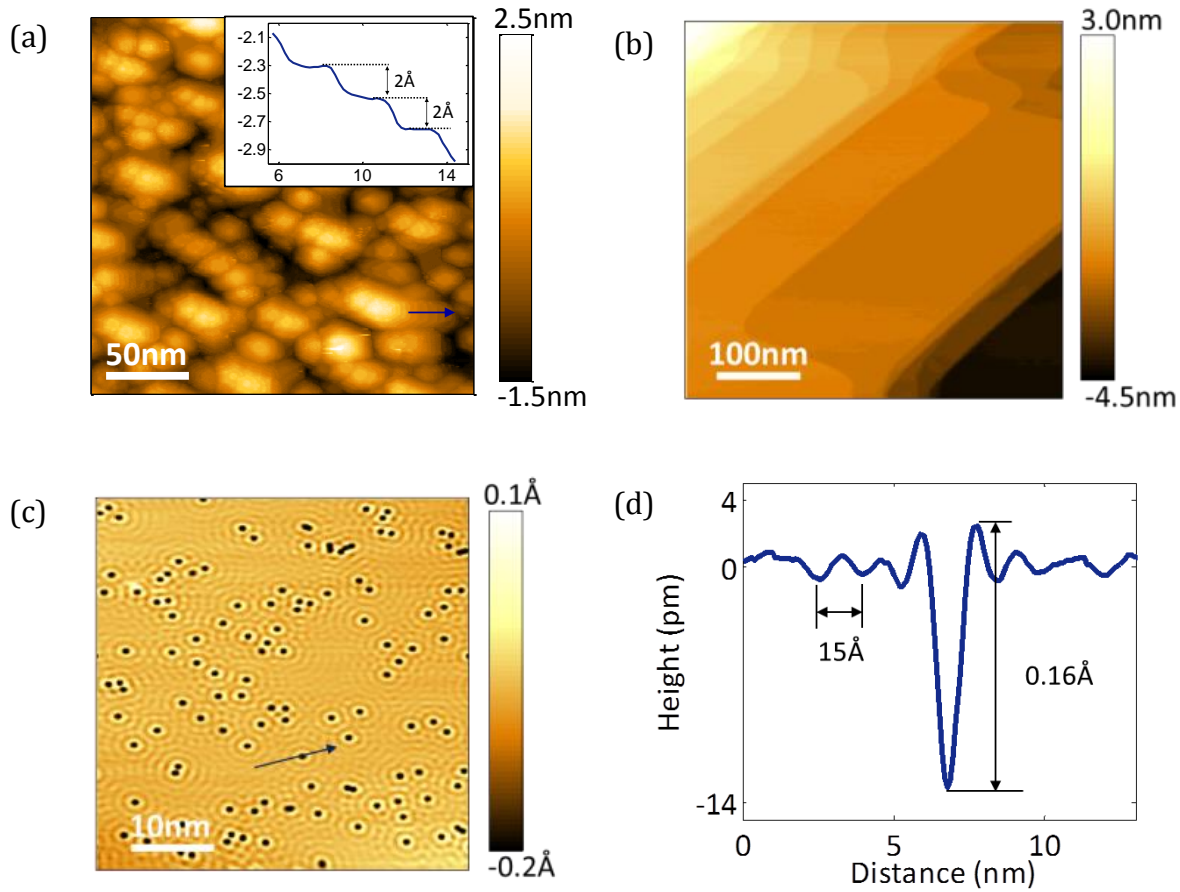


Fig. 2.3 Preparations of Cu(111) surface. (a) STM topography of Cu(111) surface after Ar^+ bombardment; (b) STM image of clean Cu(111) surface, displaying terraces and steps; (c) Zoom-in of Cu(111) surface, showing sulfur defects (atomic depressions); (d) Line profile across one sulfur defects, as marked by the arrow in (c), showing a depth of $\sim 0.15\text{\AA}$ for the defect and a wavelength of $\sim 15\text{\AA}$ for the ripple-feature. Scanning conditions: $V_{\text{bias}} = 0.8\text{V}$ and $I_{\text{set}} = 0.8\text{nA}$ for (a) and (b); $V_{\text{bias}} = 0.1\text{V}$ and $I_{\text{set}} = 0.3\text{nA}$ for (c).

2.2.2 Preparations of Graphene on Cu Substrates

After obtaining clean Cu surfaces, we are ready to prepare graphene thin films on top of them. Here, we choose ethylene (C_2H_4) as the only precursor for the graphene growth because it is easier to

monitor one component at one time in UHV chamber. The only two parameters that we can adjust are pressure of C_2H_4 and temperature of Cu substrates.

At the first trial of growth, we attempted to grow graphene on Cu(111) by heating up the crystal up to $\sim 900^\circ\text{C}$ in C_2H_4 at a pressure of $\sim 10^{-5}$ torr range for 20mins (up to 10^4L of C_2H_4 deposited on to Cu surface). This was followed by annealing the sample at 800°C for 15mins at 10^{-9} torr and cooling down to room temperature. We found that these conditions are not sufficient to grow large-area graphene on Cu(111) surfaces. Comparing with the previous in-situ graphene growths in which graphene was grown by passing $\sim 100\text{L}$ hydrocarbon over heated transition metal substrates [12, 13, 36], it indicates that the catalytic efficiency of Cu is much lower than that of other transition metals such as Ni, Ru, Ir, ... We did, however, find evidence of carbon incorporation into Cu single crystals – the well-ordered terraces of pristine Cu(111) disappeared and are replaced by a rough topology with islands and valleys as shown in Fig. 2.4a. A natural question is whether these islands are graphene nano-islands. The answer is no because the step heights for islands and valleys on this surface are the same as Cu(111) step height, $\sim 2\text{\AA}$, as displayed in the line-profile in Fig. 2.4b. Further-more, the atomic resolution topography on the surface only show a hexagonal lattice with lattice constant same as that of Cu(111), $\sim 2.55\text{\AA}$. Therefore, we conclude that the surface in Fig. 2a is indeed a disordered Cu (111) surface. Sequential scans of topography images taken over the same area, in Fig. 2.4c and Fig. 2.4d, show that these Cu islands and valleys can diffuse over the surface in a relative short time scale, less than 4mins per scan. To be specific, we highlighted the changes in Fig. 2.4c and Fig. 2.4d, where the black arrow points to the position with two depressions getting merged and the white arrow points to spot with the top layer of Cu vanishing after one scan. More changes in the sizes and shapes of islands and depressions are also observable in the two scans.

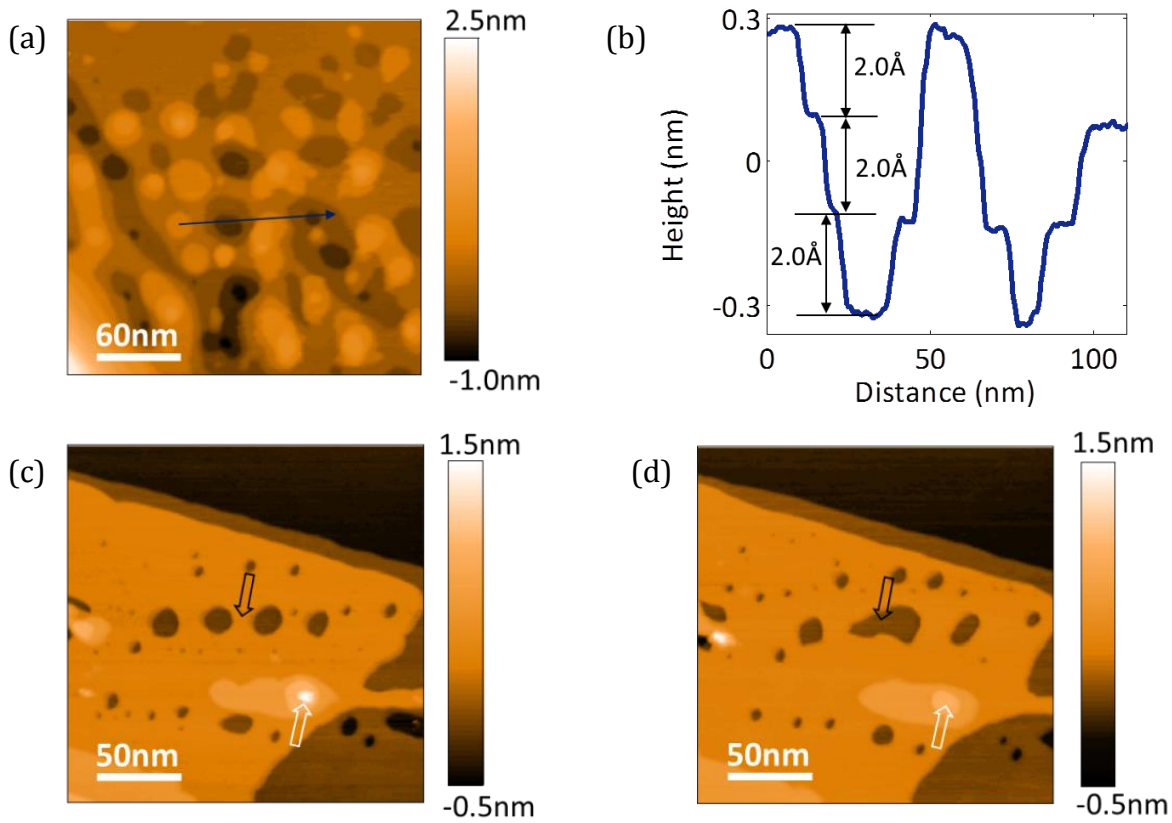


Fig. 2.4 Cu(111) surface after 1st trial of graphene growth. (a) STM image of Cu(111) surface after 1st trial of graphene growth, showing islands and depressions over the surface; (b) Line profile at the position indicated by the blue arrow in (a), confirming the step height of 2.0Å; (c) and (d) Sequential scans of STM images taken at the same area, with the black arrow highlighting the merge of two depressions and writing arrow pointing the disappearance of a top layer. Scanning conditions: $V_{bias} = 0.6V$, $I_{set} = 0.8nA$.

We attribute such an unstable, disordered surface to the incorporation of carbon atoms in the top layers of the crystal, which prevents Cu surface arranging in large terraces as in the case of pristine Cu(111). Therefore, we annealed such a rough Cu(111) surface at high temperature of 800°C for extended periods of time of a few hours. As a result, the islands and valleys combine to form well-ordered terraces, as shown in Fig. 2.5a. Taking a careful look at the terraces, we notice

that the hexagonal island in the center of the image does not align with any other terraces, and the step height of this island is $\sim 1.5\text{\AA}$ (Fig. 2.5b), different from that of Cu(111). Moreover, the atomic resolution topography on this hexagonal island displays a honeycomb lattice with a lattice constant of $\sim 2.45\text{\AA}$ (inset of Fig. 2.5a). Therefore, it is evident that this center island is a piece of graphene nano-flake. It is worth to stress on two points here. First, the DOS of pristine graphene around its Fermi level (e.g. Dirac point) is much smaller than that of Cu(111) surface states, because graphene is a semi metal with almost zero DOS around Dirac points [37] while Cu(111) surface states is metallic with constantly high DOS above -0.5eV (referenced with its Fermi level) [35]. Such a difference in DOS is exactly the main reason why the apparent height of graphene on Cu(111) is smaller than that of Cu(111) steps. Second, as highlighted in Fig. 2.5.a, the orientations of the edges of the graphene island match very well with the crystalline directions of the honeycomb lattice. This indicates that the zigzag edge is the growth front for this graphene nano-island. A survey across the surface shows less than 1% of surface is covered by such islands, which is far away from a full coverage of monolayer graphene.

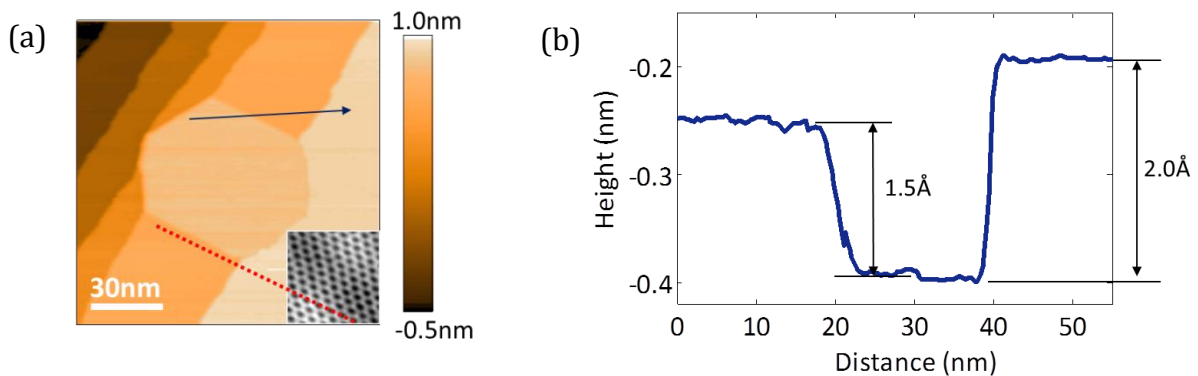


Fig. 2.5 Graphene nanoisland. (a) STM image of a hexagonal graphene nanoisland grown on Cu(111); inset image shows the honeycomb lattice obtained on the nanoisland, with zig-zag edge aligned with the edge of island; (b) Line profile taken at the position along the blue arrow in (a), with graphene's apparent height of 1.5\AA .

In order to achieve large-area monolayer graphene, the results of the first trial suggest to increase the C_2H_4 exposure to the hot Cu surface. Accordingly, the clean Cu(111) single crystal was exposed at $\sim 900^\circ\text{C}$ to 1 mtorr C_2H_4 for 5mins ($\sim 3 \times 10^5\text{L}$), which was followed by annealing at 800°C in UHV for 15mins. As a result of this preparation procedure, we achieved monlayer graphene covering the entire Cu(111) surface. We applied the same recipe for graphene growth on Cu(100) surface, and Cu foil as well. Sooner after the growth, we transferred the samples from the preparation chamber into STM chamber for characterizations. The results of STM characterizations are discussed in details in the following session 2.3, and Raman spectroscopy measurements are shown in session 2.4 as well.

2.3 Atomic Scale Characterizations of Graphene/Cu Substrates

2.3.1 Graphene/Cu(111)

Over a large scale of a few hundreds nanometers, the surface displays large and clean terraces just as the pristine Cu(111) surface does, as shown in Fig. 2.6a. A close look at one of the terraces shows a hexagonal pattern with a periodicity of $\sim 6 \pm 0.5\text{nm}$ and a peak-to-trough apparent height of $0.35 \pm 0.1\text{\AA}$, as shown in Fig. 2.6b. Atomic resolution topography, in Fig. 2.6c, clearly displays the perfect honeycomb lattice of pristine graphene. Aside from the hexagonal superstructure, a few dark depletions are also observable over the area in Fig. 2.6b, one of which is highlighted by a red dashed box. These depletions result from the sulfur impurities in the Cu single crystal underneath graphene, and graphene films grow over them without any interruptions in the lattice. As shown in Fig. 2.6d, the honeycomb lattice of graphene runs continuously across such a defect in Cu. This observation shed light on the question whether impurities in Cu substrates cause defects in graphene grown on top. Apparently, our results suggest that, impurities, at least the ones at atomic sizes, would not affect the graphene quality.

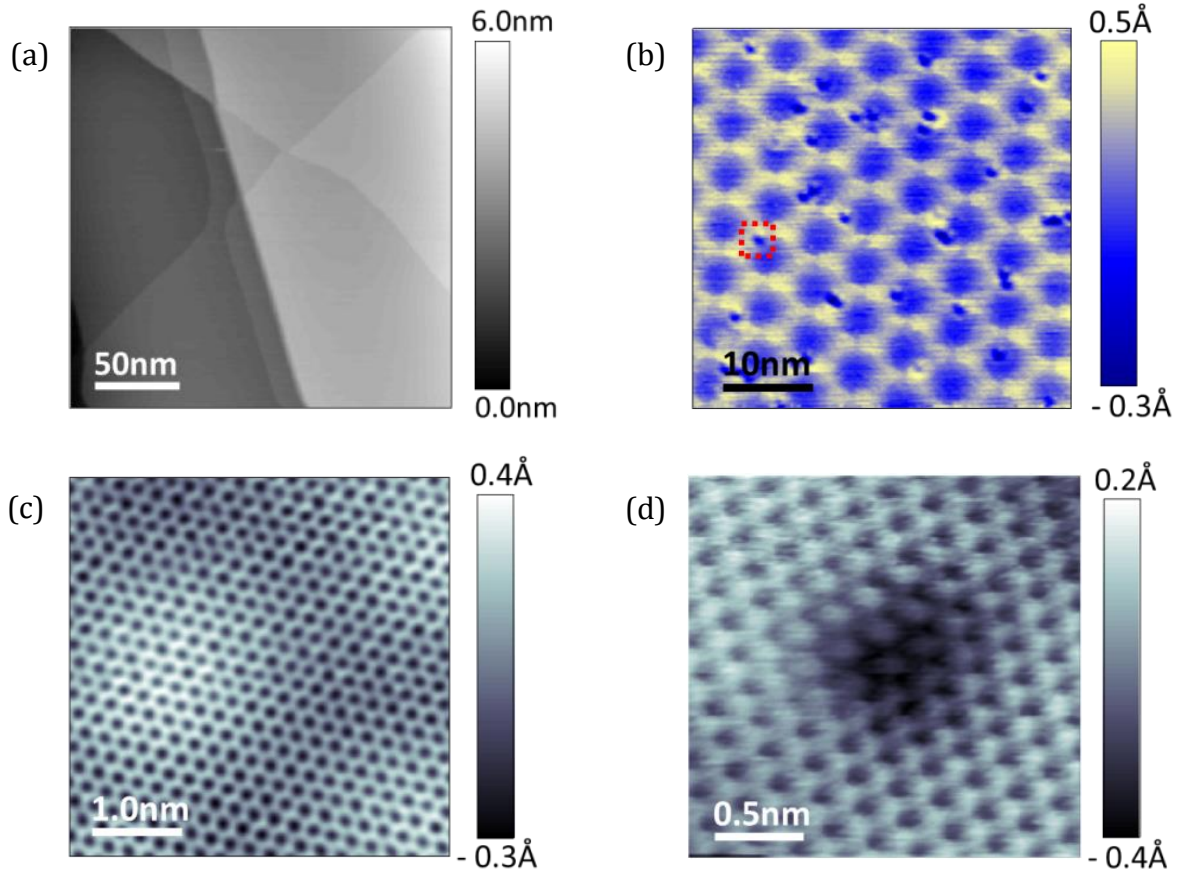


Fig. 2.6 Graphene grown on Cu(111) single crystal. (a) Large scale STM image of gr/Cu(111), showing large and flat terraces; (b) Zoom-in STM image, showing Moiré pattern with periodicity of $\sim 6.0\text{nm}$; (c) Atomic resolution topography, showing perfect honeycomb lattice of graphene; (d) Atomic resolution STM image of graphene over sulfur defect in Cu substrate. Scanning conditions: $V_{bias} = 0.6\text{V}$ and $I_{set} = 0.8\text{nA}$.

The hexagonal superstructure observed in Fig. 2.6b is in presence through the entire surface of graphene/Cu(111). It can be explained by the “beating” formed by overlaying the honeycomb lattice of graphene on top of the hexagonal lattice. As shown in Fig. 2.7a and Fig. 2.7b, hexagonal superstructures with different periodicities form when a layer of graphene is placed on top of a layer of Cu(111) with mis-oriented angles of $\theta_1 = 2^\circ$ and $\theta_2 = 15^\circ$ respectively.

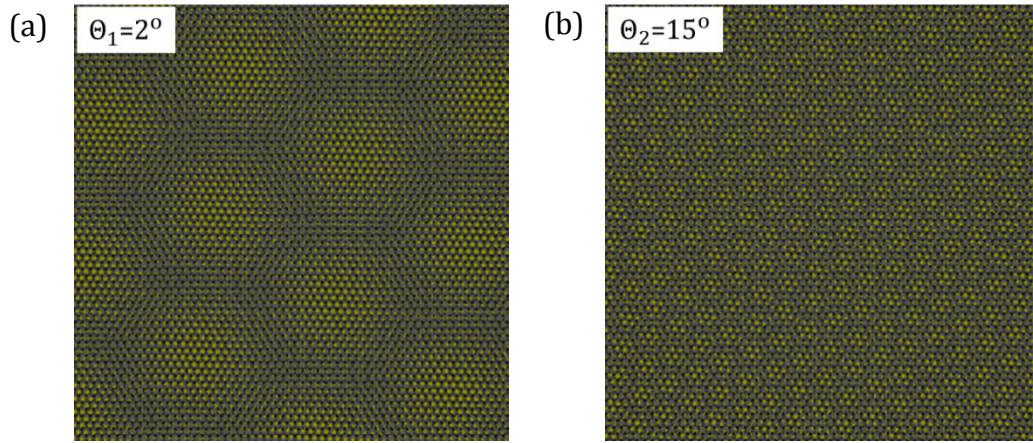


Fig. 2.6 Cartoon diagrams visualizing Moiré pattern formed by graphene and Cu(111). Depending on the angle between graphene and Cu(111), the Moiré pattern wavelength and angle vary.

A simple mathematical way to model such a problem is to sum up two periodic lattices, for instance, in one dimensional case,

$$h = \sin(k_1 x) + \sin(k_2 x) \quad (2.1)$$

where k_1 and k_2 are the wave vectors for the two periodic lattices. Eq.2.1 can be further simplified as,

$$h = 2\sin\left(\frac{k_1 + k_2}{2}x\right)\cos\left(\frac{k_1 - k_2}{2}x\right) \quad (2.2)$$

Here we adopt the assumption that $k_1 \cong k_2$, thus the periodicity of Eq.2.1 can be considered from two situations.

- (1) If $\left|\frac{k_1 + k_2}{k_1 - k_2}\right| = N \in \mathbb{Z}$, then the wave vector for Eq.2.2 is exactly $k_1 - k_2$. That is equivalent to say the two lattices are commensurate at the wave vector of $k_1 - k_2$. It is better illustrated

by the example in Fig. 2.7a, where $k_1 = 1.0$, $k_2 = 0.9$, and $\left|\frac{k_1+k_2}{k_1-k_2}\right| = 19$. For any two points which are separated by $\Delta x = \frac{2\pi}{k_1-k_2}$, as highlighted by the dark arrows in Fig. 2.8a, their h values are exactly the same. The superstructure from Eq. 2.2 are also outlined with red dashed lines which repeats at a frequency of $k_1 - k_2$.

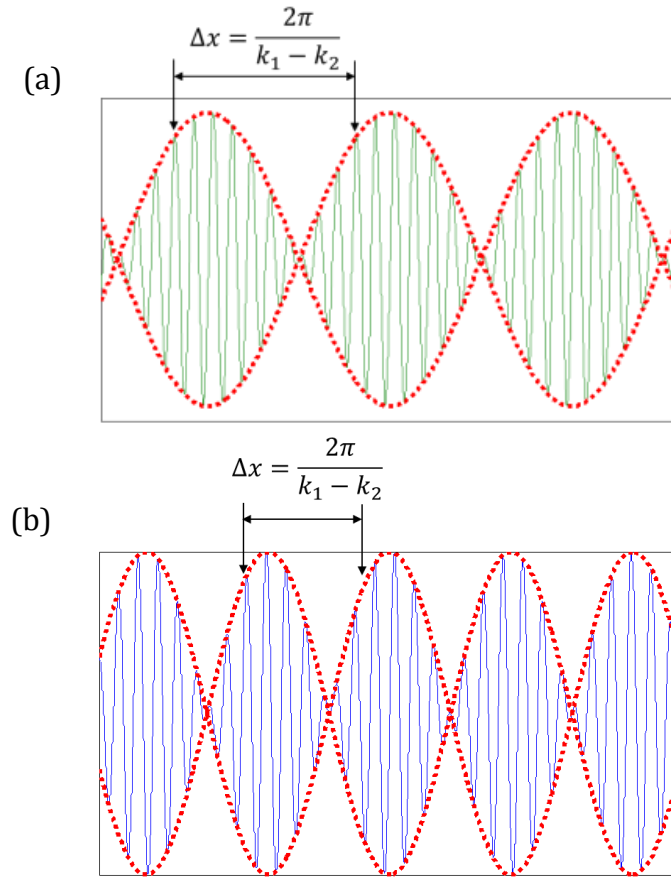


Fig. 2.8 Examples of Moiré pattern in 1-dimensional situation. (a) Commensurate case when $\left|\frac{k_1+k_2}{k_1-k_2}\right| = N \in \mathbb{Z}$. The envelop has wave vector of $k_1 - k_2$; (b) Non-commensurate case when $\left|\frac{k_1+k_2}{k_1-k_2}\right| \neq N \in \mathbb{Z}$. The envelop has wave vector of $k_1 - k_2$.

(2) If $\left| \frac{k_1+k_2}{k_1-k_2} \right| \neq N \in \mathbb{Z}$, then the wave vector for Eq.2.2 could be assigned as, but not exactly in fact $k_1 - k_2$. This is because the two lattices are not commensurate at wave vector of $k_1 - k_2$, but the super-structure pattern almost repeat at the periodicity of $\Delta x = \frac{2\pi}{k_1-k_2}$. For instance, $k_1 = 1.0$, $k_2 = 0.85$, and $\left| \frac{k_1+k_2}{k_1-k_2} \right| = 37/3$. As illustrated in Fig. 2.8b, the two spots (highlighted by two arrows) separated by Δx do not have the same h values, but the outlined envelop have a periodicity about Δx .

Therefore, the wave vector of two periodic lattice overlapping each other can be approximated by

$$k_s = k_1 - k_2 . \quad (2.3)$$

This conclusion in one dimensional case can be generalized to two dimensional case as well, but attentions should be paid to the symmetry of the two lattices. In the case of Cu(111) and graphene, both of whose lattices have six-fold symmetry, therefore

$$\vec{k}_s = \vec{k}_G - \vec{k}_{Cu} , \quad (2.4)$$

where \vec{k}_G and \vec{k}_{Cu} stand for the wave vectors of graphene and Cu(111) respectively. The relation in Eq. 2.4 is displayed in Fig. 2.9. Due to symmetry, we only consider the angles of misorientation within the range from 0° to 30° . With the value of Cu(111) and graphene wave vectors known, we can calculate the periodicity of the superstructure from the angle mismatch (θ) between Cu(111) and graphene, and vice verse, through the relation

$$k_s = \sqrt{k_G^2 + k_{Cu}^2 - 2\cos(\theta)k_Gk_{Cu}} . \quad (2.5)$$

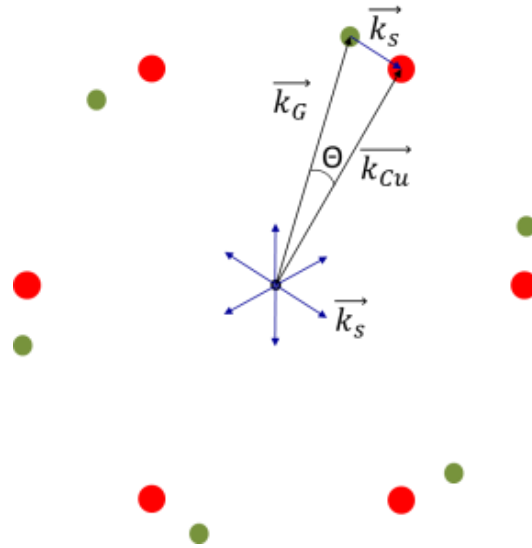


Fig. 2.9 Calculation of Moiré pattern between graphene and Cu(111). Wave vector of Moiré pattern equals to the difference between that of Cu and graphene.

Surveying over the graphene/Cu(111) surface shows that the majority of the superstructures seen on the surface have a wavelength $\sim 6\text{nm}$. Putting $k_s = \frac{2\pi}{6}\text{nm}^{-1}$, $k_G = \frac{2\pi}{0.246}\text{nm}^{-1}$ and $k_{Cu} = \frac{2\pi}{0.255}\text{nm}^{-1}$ in Eq. 2.5, we found the angle between graphene lattice and the underlying Cu(111) lattice is $\theta = 0^\circ$. This indicates that graphene primarily grows in registry with the Cu(111) hexagonal lattice underneath, and it is further confirmed by the Low Energy Electron Diffraction (LEED) pattern in Fig. 2.10. In LEED pattern, the six brightest spots represent the combination of Bragg peaks of Cu(111) and the aligned graphene pieces. Besides this, a faint ring is also visible at the same diameter as the six Bragg peaks, representing the crystalline orientations of the remaining graphene pieces which are misoriented from Cu(111) lattice.

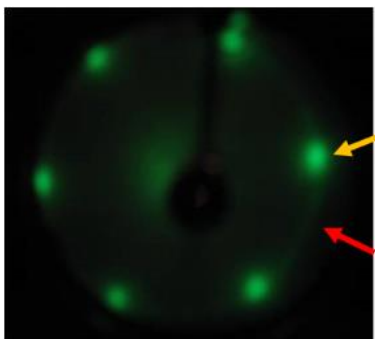


Fig. 2.10 LEED pattern of graphene/Cu(111) taken at beam energy of $\sim 70\text{eV}$. Yellow arrow pointing the Bragg lattice of Cu(111) and aligned graphene domains, and red arrow highlighting the ring from the LEED pattern of mis-oriented graphene domains.

In the presence of graphene domains with different crystalline orientations, it is natural to ask where and how these domains stitch together. Fig. 2.11a and Fig. 2.11b are two interesting cases where a grain boundary is found on the surface of graphene/Cu(111) surface. Fig. 2.11a shows an image taken on an area of the sample where a number of nm-scale impurities are present. The super-structure orientations and wavelengths are clearly different across the line of impurities, showing that graphene grain boundaries can be stabilized by such large-scale impurities. In Fig. 2.11b, we see that a graphene grain boundary exists at the step edge of an atomic terrace of Cu(111). However, the large-scale impurities in Fig. 2.10a and the step edges in Fig. 2.10b are not necessary for the formation of grain boundary. Instead, a more common case of graphene grain boundaries is shown in Fig. 2.11c where the two mis-oriented honeycomb lattices merges together through atomic scale defects. Due to the electronic component in STM topography, it is hard to directly visualize the structure of the defects through STM. Later on Transmission Electron Microscopy (TEM) results revealed that the grain boundaries are primarily made of pentagons and heptagons [20]. The domains of graphene usually runs across the steps of Cu(111) without any

disruption in graphene lattice. As shown in Fig. 2.11d, the Moiré pattern extends continuously from the upper terrace to the lower one, indicating the continuity of the honeycomb lattice of graphene.

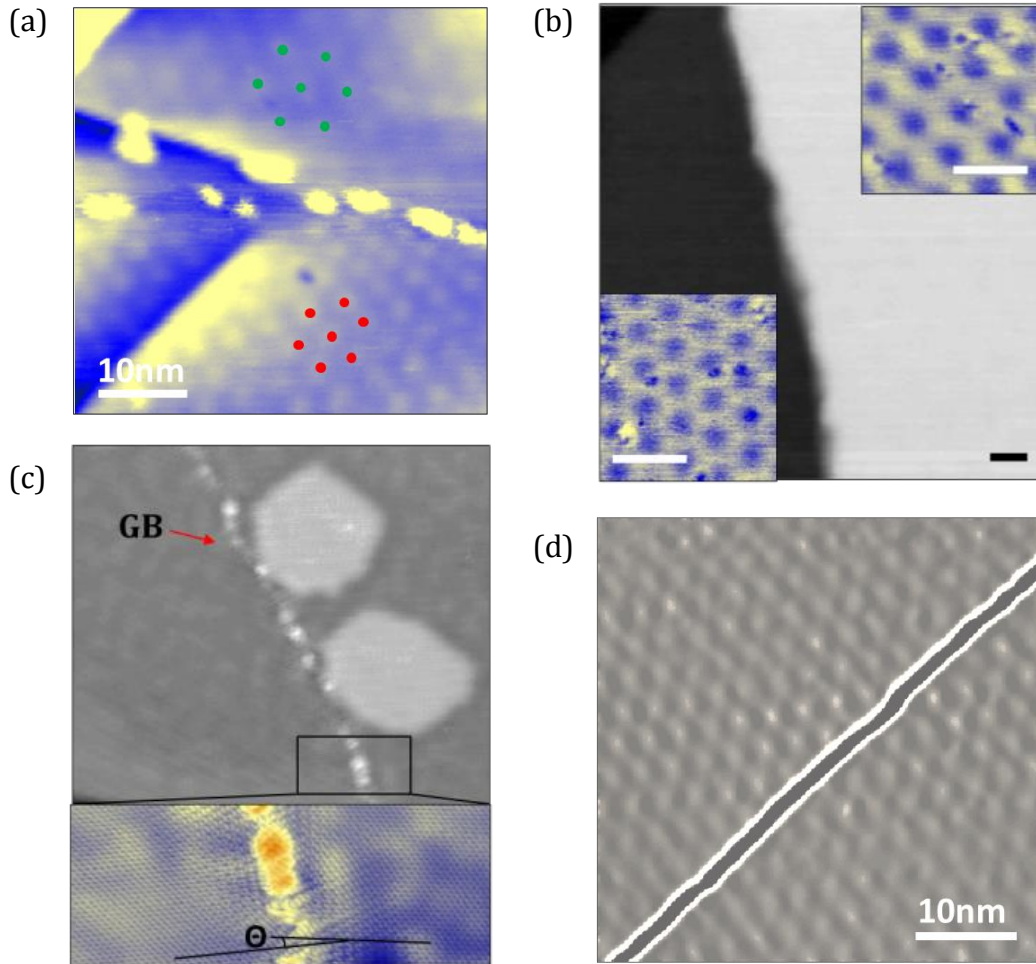


Fig. 2.11 Grain boundaries in graphene films grown on Cu(111) surface. (a) One grain boundary stabilized by nano-scale impurities, with red and green hexagons highlight the two Moiré patterns on two sides of the grain boundary; (b) One grain boundary at the step edge, proven by two different Moiré patterns on the two terraces, with scale bar of 5nm; (c) One grain boundary on the terrace of Cu. Inset is a zoom-in across the grain boundary (d) A graphene domain runs continuously over a Cu step (derivative image). Scanning conditions: $V_{bias} = 0.8V$ and $I_{set} = 0.6nA$.

In several previous experiments [38, 39], graphene has been reported to be impervious to many gases and chemicals, and thus provides an atomically-thin protective coating for the surface to which it adheres. We have probed this property of graphene on the Cu(111) surface by exposing the graphene-covered Cu(111) crystal to the ambient atmosphere for about one month and then imaging the surface without performing any cleaning cycles. Under normal circumstances, the reactive surface of Cu would be completely oxidized, but we found (in Fig. 2.12) that the superstructure of graphene on Cu(111) can still be easily imaged, indicating that both graphene and Cu(111) surfaces survive from oxidation in air.

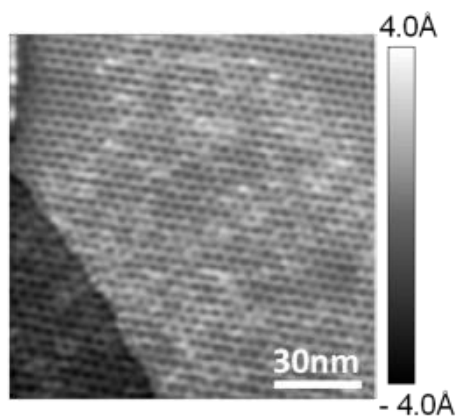


Fig. 2.12 Graphene on Cu(111) after exposure to air for one month. Moiré pattern indicates that graphene prevents Cu(111) surface from getting oxidized in ambient atmosphere. Scanning conditions: $V_{bias} = 1.0V$ and $I_{set} = 0.5nA$.

After taking careful investigations on the topographic structures of graphene/Cu(111), we further studied the electronic properties of such system by performing STM measurements at different energy levels. Shown in Fig. 2.13a –c are a sequence of STM topographs taken over the same area of the surface at various tip-sample bias voltages. Three prominent features are observable in these images – point-like defects, electronic “rings” around the point defects and the

hexagonal superstructure. The point-like defects have been shown to be sulfur defects in Cu(111) substrates [35] and graphene runs across them continuously. The second feature observed in the graphene/Cu(111) surface is the presence of “rings” around the sulfur defects at bias energies greater than -500meV (referenced to the Fermi level of graphene/Cu(111)). These “rings” are similar to the scattering interference patterns seen on pristine Cu(111) surface [35]. Fig. 2.13d displays the wave vectors of the “ring” features in Fig. 2.13a and b respectively. As we see, the wave vectors are not symmetric about Fermi levels, and their value of $\sim 3.5 \text{ nm}^{-1}$ is much larger than that of graphene near Dirac points, $[0, 1.0] \text{ nm}^{-1}$ for the energy window of $[E_D, E_D + 1.0 \text{ eV}]$. Therefore, it is convincing that these ripples are scattering interference patterns from Cu(111) surface states, instead of from graphene. Furthermore, comparing the wave vectors in Fig. 2.13d with that of pristine Cu(111) at the same energies, they still differ a little from each other. This indicates the influence of the existence of the adjacent monolayer graphene films on the electronic structure of Cu(111) surface. We have delivered a full set of STS map measurements to probe the interactions between graphene and Cu(111) surface states when they are put into proximity, and found that the band edge of Cu(111) surface states is shifted up for about 100meV and the effective mass of Cu(111) surface states is renormalized to 1.5 times of the pristine one. Later on in this session, we will have detailed descriptions of these findings. The third feature seen prominently in Fig. 2.13 is the hexagonal pattern which we described earlier. We note that while the wavelength of the superstructure is not energy dependent, the intensity of the pattern is strongly dependent on the bias energies and becomes very weak below -500meV where happens to be about the band edge of Cu(111) surface states. This indicates that the Moiré pattern between graphene and Cu(111) is not only a result of geometry, but also coupled with electronic interactions.

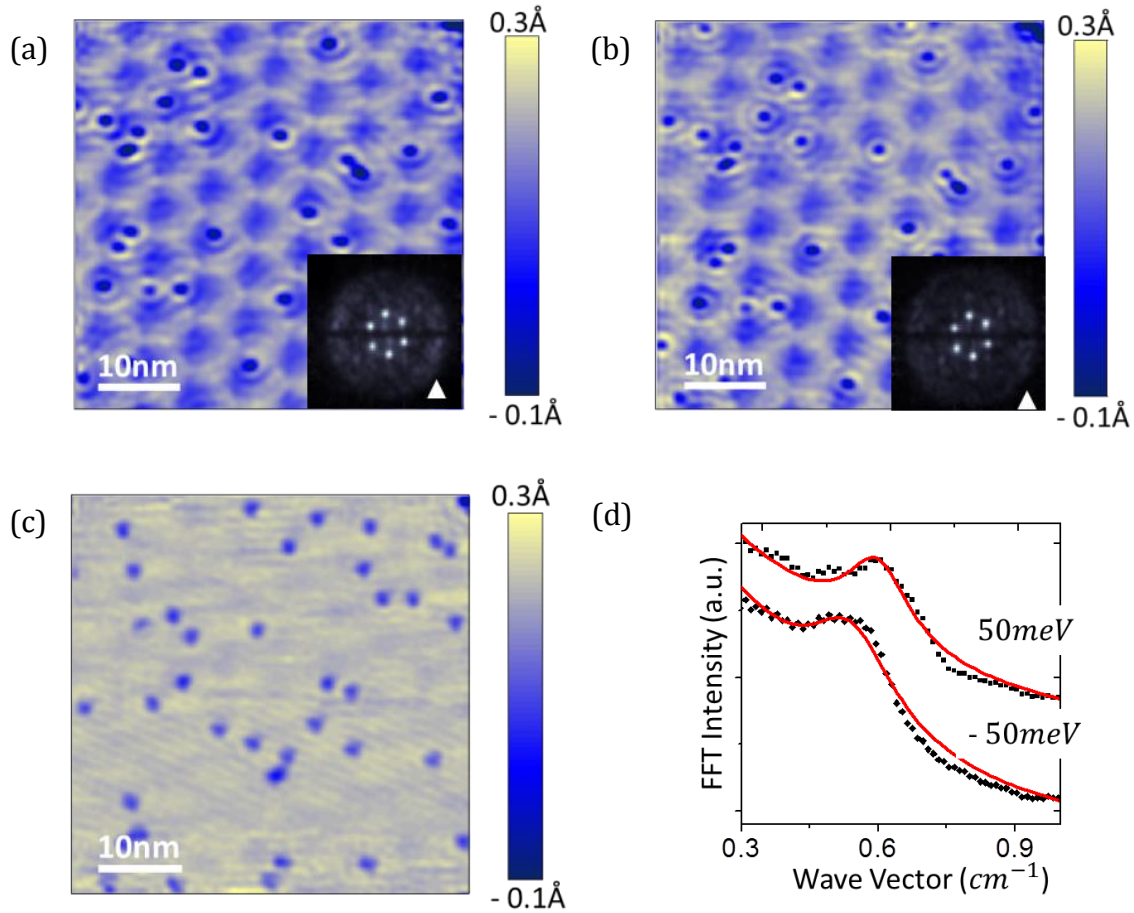


Fig. 2.13 Bias dependent topographs of graphene/Cu(111). (a)-(c) STM topography images taken at different bias energies of -50 meV, 50 meV, -500 meV respectively. Insets of (a) and (b) showing Fourier transformation of their corresponding topography; (d) Plot of angular averaged FFT intensity V.S. wave vector.

As seen from the topography in last paragraph, the ring-like feature originated from the quantum interferences of Cu(111) surface states has a strong energy dependence. To quantify such an energy dependence as well as to compare the result with pure Cu(111) surface states, we performed careful differential conductance maps (dI/dV maps) at various bias energies and did fast Fourier transformation (FFT) of each map to obtain the wavelength of the ring feature. We show

one of such maps taken at an area of $100 \times 100 \text{ nm}^2$ at a bias energy of 0.2 eV in Fig. 2.14 and its FFT in the inset of Fig. 2.14. Clearly, we observe two rings in the FFT image. One guess could be that one of them results from the quantum interference pattern of Cu(111) surface states and the other one from graphene. Whether this guess is the fact will be further testified by the plot of energy V.S. wave vector.

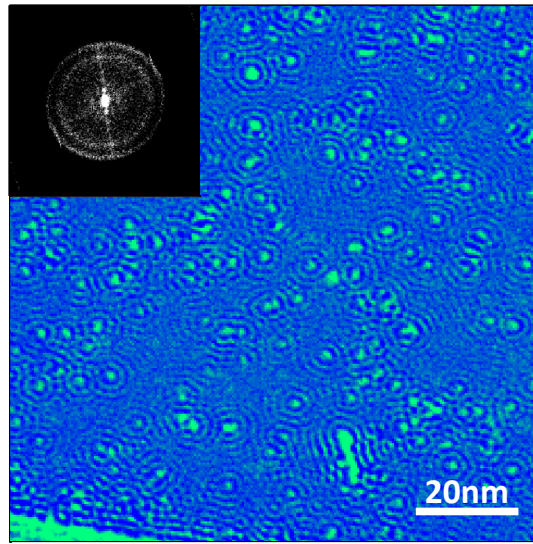


Fig. 2.14 Quantum interference pattern map of graphene/Cu(111) surface at an area of $100 \times 100 \text{ nm}^2$. Scanning conditions: $V_{bias} = 0.2 \text{ V}$ and $I_{set} = 0.2 \text{ nA}$. Inset shows the FFT of this map, with two sets of rings clearly seen.

Fig. 2.15(a) displays the FFT images for various bias energies. The two-ring feature shows up in all positive bias voltages (i.e. above Fermi level) and is absent in all negative bias energies. The relation between bias energies and the wave vectors extracted from FFT maps is plotted in Fig. 2.15(b). There are two prominent features shown in the plot. First, one wave vector (red diamond) of the two rings above Fermi level stays constant over the positive bias energies while the other set (green diamond) of plot is well fit by a parabolic function (blue dashed line). This fact states that

one ring with parabolic band structure indeed originates from the scattering of Cu(111) surface states while the other one with constant wave vector is not related with quantum interferences in graphene. The interference pattern with constant wave vector was previously reported in Au(111) surface states [40, 41]. However, the exact reason of this feature remains unknown. Some guess is the in-elastic tunneling of Cu(111) surface states electrons with higher tunneling energies, or the elastic tunneling of Cu(111) bulk electrons. Second, as a comparison with pure Cu(111) surface states (red circles and solid black fitting line), the band structure of Cu(111) surface states is strongly modified by the presence of a layer of graphene film on top. The fitted results show that the effective mass increases from $0.4m_e$ to $0.58m_e$ ($\sim 50\%$ incensement) and the band edge shifts from $-0.45V$ to $-0.3V$. Such dramatic changes in the band structure indicate the interactions between graphene layer and Cu(111) surface states. One obvious confinement resulting from this overlying geometry is the Moiré pattern superstructures. Therefore, we studied the modified band structures of the Cu(111) surfaces in multiple areas with different Moiré pattern periodicities, and show our results in Fig. 2.15(c). Clearly, the modified band structure of Cu(111) surface states is independent on the Moiré pattern wavelengths. This is different from the findings in the literature on an adhesion layer of metal atoms on top of Cu(111) [42, 43] where it is stated that the superstructure is the origin of band structure modification. However, in the literature, the band structure modification is more of a shift in band edges, rather than a big change in effective mass.

At this stage, we do not have a definite answer to why the presence of graphene monolayer modifies Cu(111) surface states so dramatically. As we know, graphene is a true two-dimensional electron gas (2DEG) which behaves as massless Dirac fermions, while Cu(111) surface states is a quasi-2DEG whose band structure obeys Schrödinger equation. When these two 2DEG are put into

proximity, the interactions/screenings between their electrons must play an important role in determining the resulted electronic structures.

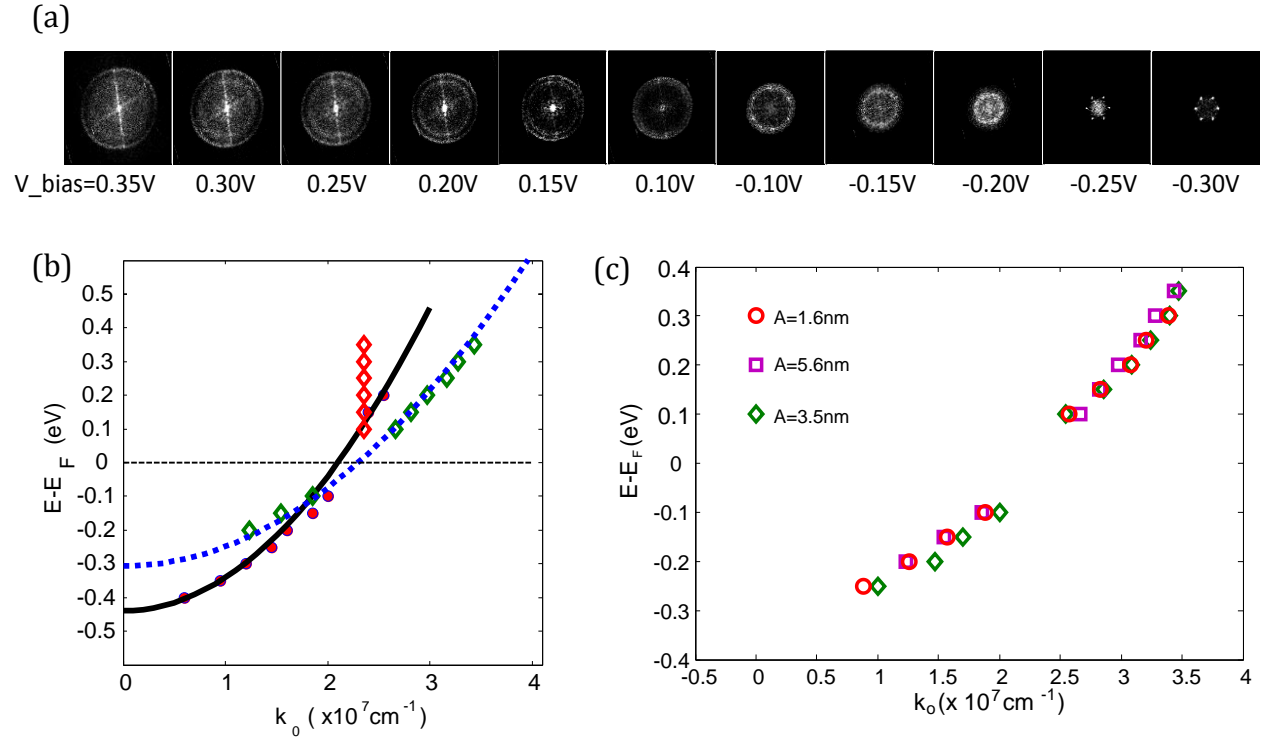


Fig. 2.15 Modified band structure of Cu(111) surface states in the presence of graphene monolayer. (a) A set of FFT of dI/dV maps taken over bias energies from -0.35V to 0.35 V. (b) Band structure of graphene/Cu(111). (c) Band structure of graphene/Cu(111) taken at multiple areas with different Moiré pattern periodicities.

2.3.2 Graphene/Cu(100)

Besides Cu(111), Cu(100) is another crystalline facet commonly seen in Cu polycrystals [44-46]. Therefore, it is important as well to understand the graphene growth on Cu(100) surface. Here, the crystal structure of Cu(100) is a square lattice, which has a totally different symmetry compared to the honeycomb lattice of graphene.

The same recipe of producing large-area monolayer graphene on Cu(111) single crystal was employed here to grow graphene on Cu(100). As a result, we find that while most of the Cu(100) surface (>95%) is covered by with graphene films, the microscopic structure of graphene shows nano-scale valleys in graphene reaching down to the surface of Cu(100) substrate, as shown in the large scale STM topography in Fig. 2.16a and the line profile in Fig. 2.16b. These results certainly indicate a much poorer quality of graphene grown on Cu(100) surface, as compared to that on Cu(111).

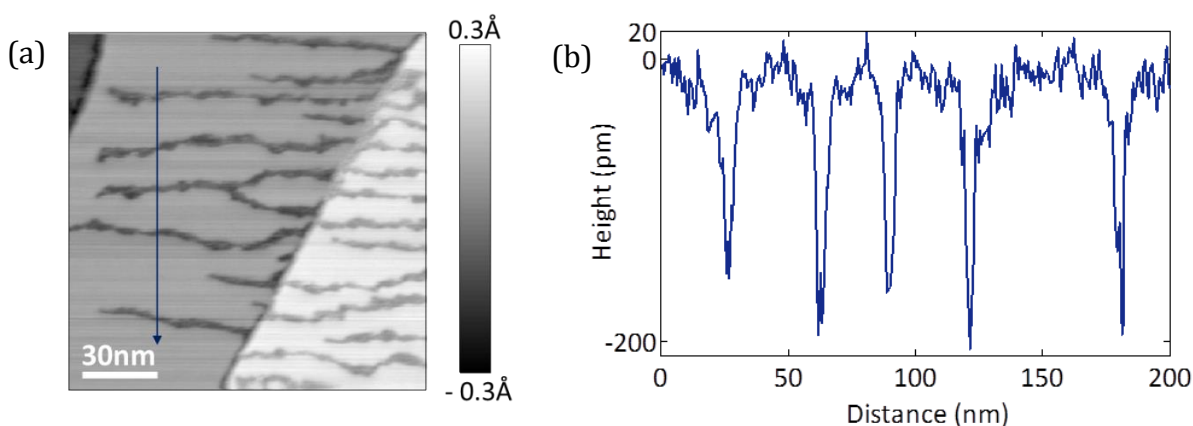


Fig. 2.16 Graphene grown on Cu(100). (a) Large scale STM image of graphene/Cu(100) showing cracks in graphene films. (b) Line profile along the blue arrow in (a), showing the crack in graphene film reaches the surface of Cu(100).

The graphene layer itself on Cu(100) mostly displays a linear superstructure of $\sim 11\text{\AA}$ periodicity, as shown in Fig. 2.17a. We can clearly observe the honeycomb lattice of graphene on top of this linear superstructure, and find the angle mismatch of approximately 2° (in case of Fig. 2.17a) between the linear pattern and the honeycomb lattice. To visualize the origin of this linear superstructure, we can put a layer of honeycomb lattice on top of a layer of square lattice with their crystalline orientation aligned at $\sim 2^\circ$, as shown in Fig. 2.17b. Aside from the majority of the linear

pattern, we do occasionally observe some “quasi-hexagonal” superstructures, such as the one shown in Fig. 2.17c, as well. This “quasi-hexagonal” forms by properly choosing the mis-alignment between graphene lattice and Cu(100) lattice, as shown in Fig. 2.17d.

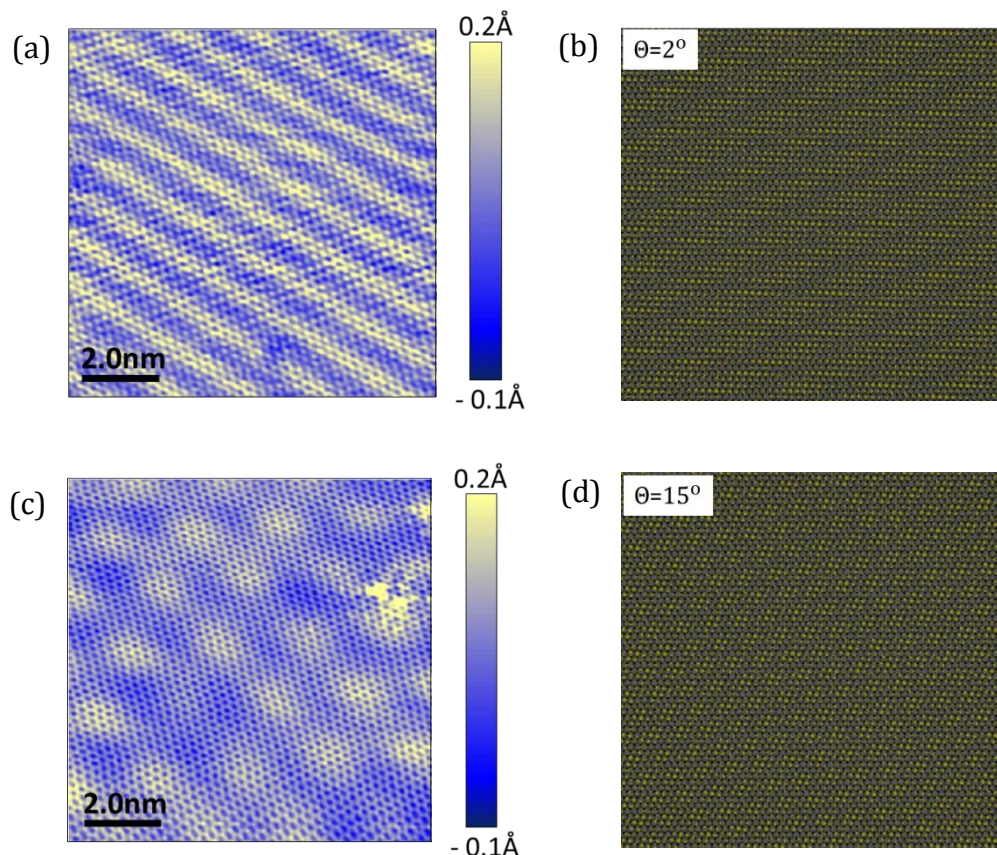


Fig. 2.17 Moiré pattern of graphene on Cu(100) surface. (a) and (c) STM topography of graphene on Cu(100), displaying linear Moiré pattern and “quasi-hexagonal” Moiré pattern; (b) and (d) Cartoon diagrams, visualizing Moiré pattern from mismatching Cu(100) lattice with graphene lattice.

Based on the symmetries of honeycomb lattice of graphene and square lattice of Cu(100), there are two ways to align graphene lattice with Cu(100) lattice. One alignment is to match one reciprocal lattice vector of graphene to a-axis of Cu(111), as shown in Fig. 2.18a, and the other one

to align graphene lattice vector along with b-axis of Cu(111), as illustrated in Fig. 2.18b. A LEED pattern of graphene/Cu(100), in Fig. 2.18c, indeed shows two sets of hexagons and they are 30° rotated with each other. With the help of illustration from Fig. 2.18a and Fig. 2.18b, we assign the two sets of hexagons are two sets of graphene Bragg lattice which are aligned with a-axis and b-axis of Cu(100) surface respectively. The strong intensity of the two hexagons indicates that graphene growth on Cu(100) surface prefers to be in registry with Cu(100) crystalline directions. Besides these two sets of hexagons, a faint ring feature also shows at the same radius as the two hexagons in the LEED pattern. This ring feature signals for the other graphene domains whose orientations are off from a- and b-axis of Cu(100), which is in good agreement of observations of “quasi-hexagonal” superstructures in STM images in Fig. 2.17c.

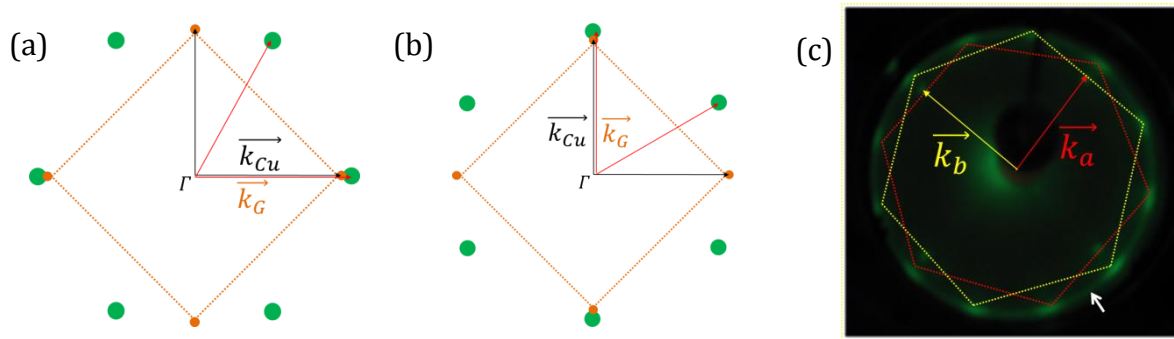


Fig. 2.18 LEED pattern of graphene on Cu(100) surface. (a) and (b) Cartoon diagrams for graphene aligning with Cu(100) lattice; (c) LEED pattern of graphene/Cu(100), displaying two sets of hexagons aligned with two crystalline orientations of Cu(100), \vec{k}_a and \vec{k}_b .

2.3.3 Graphene/Cu foils

The Cu foils used in typical CVD graphene growth in tube furnaces are polycrystalline, where much more crystalline facets of Cu are in presence [32]. Based on our comparisons between graphene

growth on Cu(111) and Cu(100) single crystals, we find that graphene growth faster and better on Cu(111) than on Cu(100) with the same growth recipe, and predict that it requires much stronger conditions to produce good quality of graphene on Cu foils than on Cu(111)/Cu(100) single crystals. As a test, we attempted to produce graphene on Cu foil with the same growth conditions as on Cu single crystals, and rarely found any graphene flakes grown. Fig. 2.19 shows an optical image of a piece of graphene flake on SiO₂/Si substrate which was grown on Cu foil in UHV conditions. As we see, the coverage of growth is very low since we only find such isolated flakes after the growth. Moreover, the growth front is rather complicated due to the un-isotropy of the carbon diffusion on Cu foil, as compared to the zigzag growth front and the hexagonal island of graphene/Cu(111) as shown in Fig. 2.5b.

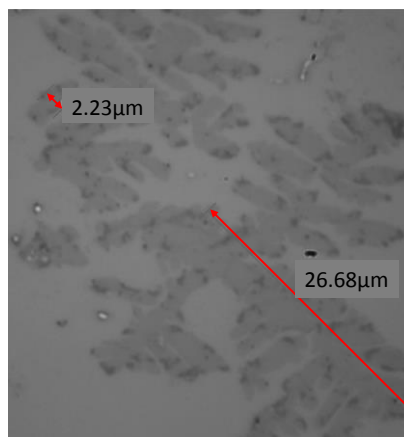


Fig. 2.19 Optical image of graphene flake grown on Cu foil in UHV and transferred to SiO₂/Si substrate, displaying dendritic structure of the graphene island.

After comparing graphene films grown in UHV conditions on Cu(111), Cu(100) single crystals and Cu foils, it is worth to take a microscopic look at the graphene films grown in tube furnace with the standard recipe. So we sent a piece of as-grown graphene/Cu foil, applied a gentle annealing treatment at ~350°C for 3-4 hours, and imaged with STM afterwards. Fig. 2.20a displays

a large scale STM topography of graphene on Cu foil. The overall roughness results from the polycrystalline nature of Cu foil which preserves even after 1000°C high temperature treatment during graphene growth. A close look at the graphene on a terrace of Cu foil, in Fig. 2.20b, clearly shows the perfect honeycomb lattice, as well as a faint Moiré pattern. We did notice that there are no atomic defects observed in the domains of graphene produced by this CVD method.

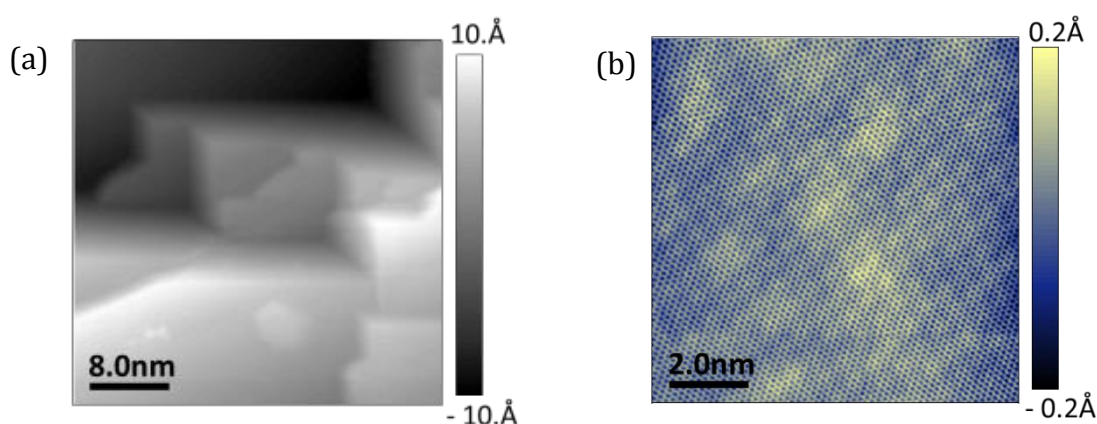


Fig. 2.20 STM topography images of graphene on Cu foil grown by conventional CVD recipe. (a) Large scale topography displaying Cu foil roughness; (b) Zoom-in image on a terrace of Cu foil, showing perfect honeycomb lattice and a faint superstructure on top of it.

2.4 Raman Spectroscopy of Graphene/Cu Substrates

Raman spectroscopy has been a necessary technique to characterize graphene ever since it demonstrated its unique capability in 2006 [47]. Here, after performing microscopic level studies on graphene grown on Cu single crystal and polycrystalline substrates via STM, we also characterized these systems by raman spectroscopy from a micron-meter scale perspective.

After the growth and STM characterizations in-situ, we took graphene/Cu substrates out of UHV chamber and performed raman measurements on them without any further treatment ex-situ.

Fig. 2.21 upper panel shows a Raman spectroscopy taken on graphene/Cu(111). The presence of D peak in the spectrum indicates defects in the surveyed area which is the spot size of laser, $\sim 20\mu\text{m}$ in diameter [48-50]. As STM topography images have proved that there are no atomic defects within the domains of graphene films, the defects detected here must originate from the ones at grain boundaries. A rough estimation of defect concentration from Raman spectroscopy is by the equation reported by Ruinstra and Koenig [51],

$$\sqrt{\frac{1}{\rho}} = \frac{560}{E_l^4} \left(\frac{I_D}{I_G} \right)^{-1}, \quad (2.6)$$

where ρ is the concentration per nanometer-square and E_l is the excitation laser energy used in the Raman measurements in eV. We used green laser with wave length of 534 nm ($\sim 2.3\text{eV}$) in the experiment, and measured the value of $\frac{I_D}{I_G} = 0.7$. With the fact that the defects are at the edge of each domain, we have the relation between domain size and defect concentration,

$$\rho = \frac{\rho_c \cdot \pi \cdot \Delta R \cdot R}{\pi R^2}, \quad (2.7)$$

where ρ_c is the proper atomic density at graphene boundaries in unit of nm^{-2} , R is radius of the domain, and ΔR is the width of the domain boundaries. Here we set $\Delta R = 2\text{\AA}$ and $\rho_c \sim 10\text{nm}^{-2}$, and put them into Eq. 2.6 and Eq. 2.7, we get $R \cong 1.0\mu\text{m}$. Therefore, the estimated domain size of graphene grown on Cu(111) is in order of $1\mu\text{m}$, which is slightly smaller than the ones ($\sim 3\text{-}4\mu\text{m}$) from CVD tube growth.

In Fig. 2.21 lower panel, a Raman spectroscopy of graphene grown on Cu(100) shows a much larger $\frac{I_D}{I_G}$ ratio, indicating a much smaller domain size of graphene or much more defects in

the film. In conjunction with the valley-features in STM topography images (Fig. 2.14a and b), a much worse quality of graphene grown on Cu(100) is further confirmed.

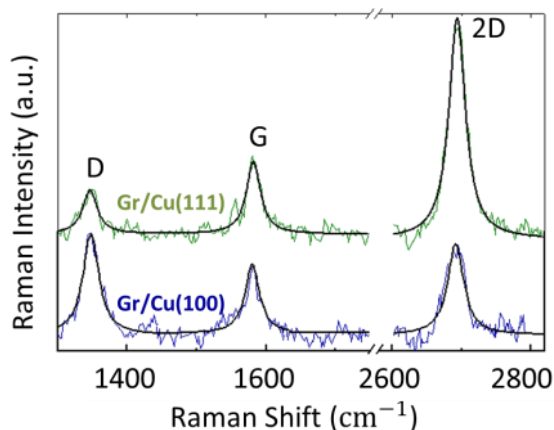


Fig. 2.21 Raman spectra taken on graphene/Cu(111) and graphene/Cu(100). G and 2D peak showing monolayer graphene on Cu substrates, while D peak indicating the presence of defects in graphene films on Cu substrates. Larger D peak intensity of graphene/Cu(100) indicating worse quality of graphene on Cu(100) than on Cu(111).

Insightful analysis of Raman spectrum on graphene/Cu(111) and Cu(100) suggests large non-uniform physisorbed strain in graphene films that depends on both the crystalline structure of Cu substrates and the registry between graphene and substrate [52]. The details are not covered in this thesis, and further information can be found in Ref. [52].

In summary of the STM and Raman studies on graphene grown on different Cu substrates, we demonstrated that Cu crystalline structure plays an important role in the quality and speed of CVD graphene growth on them. Graphene grows primarily in registry with the underlying Cu lattice for both Cu(111) and Cu(100) cases. The graphene has a hexagonal superstructure on Cu(111) with a significant electronic component, whereas it has a linear superstructure on Cu(100). The film quality is limited by the grain boundaries, and the best growth is obtained on the Cu(111) surface.

2.5 References

1. Li, X., et al., *Large-Area Synthesis of High-Quality and Uniform Graphene Films on Copper Foils*. Science, 2009. 324(5932): p. 1312-1314.
2. Kim, K.S., et al., *Large-scale pattern growth of graphene films for stretchable transparent electrodes*. Nature, 2009. 457(7230): p. 706-710.
3. Berger, C., et al., *Ultrathin epitaxial graphite: 2D electron gas properties and a route toward graphene-based nanoelectronics*. J. Phys. Chem. B, 2004. 108(52): p. 19912-19916.
4. Bae, S., et al., *Roll-to-roll production of 30-inch graphene films for transparent electrodes*. Nat Nano, 2010. 5(8): p. 574-578.
5. Novoselov, K.S., et al., *A roadmap for graphene*. Nature, 2012. 490(7419): p. 192-200.
6. Avouris, P., *Graphene: Electronic and Photonic Properties and Devices*. Nano Letters, 2010. 10(11): p. 4285-4294.
7. Sakhaee-Pour, A., M.T. Ahmadian, and A. Vafai, *Potential application of single-layered graphene sheet as strain sensor*. Solid State Communications, 2008. 147(7-8): p. 336-340.
8. Schwierz, F., *Graphene transistors*. Nat Nano, 2010. 5(7): p. 487-496.
9. Levendorf, M.P., et al., *Transfer-Free Batch Fabrication of Single Layer Graphene Transistors*. Nano Letters, 2009. 9(12): p. 4479-4483.
10. Reina, A., et al., *Growth of Large-Area Single- and Bi-Layer Graphene by Controlled Carbon Precipitation on Polycrystalline Ni Surfaces*. Nano Research, 2009. 2(6): p. 509-516.
11. Park, H.J., et al., *Growth and properties of few-layer graphene prepared by chemical vapor deposition*. Carbon, 2010. 48(4): p. 1088-1094.
12. Martoccia, D., et al., *Graphene on Ru(0001): A 25x25 supercell*. Phys. Rev. Lett., 2008. 101(12): p. 126102.
13. Sutter, P.W., J.-I. Flege, and E.A. Sutter, *Epitaxial graphene on ruthenium*. Nature Materials, 2008. 7(5): p. 406-411.
14. Sutter, P., et al., *Electronic Structure of Few-Layer Epitaxial Graphene on Ru(0001)*. Nano Letters, 2009. 9(7): p. 2654-2660.
15. Moritz, W., et al., *Structure Determination of the Coincidence Phase of Graphene on Ru(0001)*. Phys. Rev. Lett., 2010. 104(13): p. 136102.
16. Coraux, J., et al., *Structural Coherency of Graphene on Ir(111)*. Nano Letters, 2008. 8(2): p. 565-570.
17. Lacovig, P., et al., *Growth of Dome-Shaped Carbon Nanoislands on Ir(111): The Intermediate between Carbide Clusters and Quasi-Free-Standing Graphene*. Phys. Rev. Lett., 2009. 103(17): p. 179904.
18. Balog, R., et al., *Bandgap opening in graphene induced by patterned hydrogen adsorption*. Nature Materials, 2010. 9(4): p. 315-319.
19. Chen, H., W.G. Zhu, and Z.Y. Zhang, *Contrasting Behavior of Carbon Nucleation in the Initial Stages of Graphene Epitaxial Growth on Stepped Metal Surfaces*. Phys. Rev. Lett., 2010. 104(18): p. 186101.
20. Huang, P.Y., et al., *Grains and grain boundaries in single-layer graphene atomic patchwork quilts*. Nature, 2011. 469(7330): p. 389-392.
21. Kim, K., et al., *Grain Boundary Mapping in Polycrystalline Graphene*. ACS Nano, 2011. 5(3): p. 2142-2146.

22. Kim, K., et al., *Raman Spectroscopy Study of Rotated Double-Layer Graphene: Misorientation-Angle Dependence of Electronic Structure*. Physical Review Letters, 2012. 108(24): p. 246103.
23. Havener, R.W., et al., *Angle-Resolved Raman Imaging of Interlayer Rotations and Interactions in Twisted Bilayer Graphene*. Nano Letters, 2012. 12(6): p. 3162-3167.
24. Tsen, A.W., et al., *Tailoring Electrical Transport Across Grain Boundaries in Polycrystalline Graphene*. Science, 2012. 336(6085): p. 1143-1146.
25. Tsen, A.W., et al., *Polycrystallinity and Stacking in CVD Graphene*. Accounts of Chemical Research, 2012.
26. Petrone, N., et al., *Chemical Vapor Deposition-Derived Graphene with Electrical Performance of Exfoliated Graphene*. Nano Letters, 2012. 12(6): p. 2751-2756.
27. Vlassiouk, I., et al., *Role of Hydrogen in Chemical Vapor Deposition Growth of Large Single-Crystal Graphene*. ACS Nano, 2011. 5(7): p. 6069-6076.
28. Li, X., et al., *Large-Area Graphene Single Crystals Grown by Low-Pressure Chemical Vapor Deposition of Methane on Copper*. Journal of the American Chemical Society, 2011. 133(9): p. 2816-2819.
29. Zhang, Y., et al., *Vapor Trapping Growth of Single-Crystalline Graphene Flowers: Synthesis, Morphology, and Electronic Properties*. Nano Letters, 2012. 12(6): p. 2810-2816.
30. Li, Z., et al., *Low-Temperature Growth of Graphene by Chemical Vapor Deposition Using Solid and Liquid Carbon Sources*. ACS Nano, 2011. 5(4): p. 3385-3390.
31. Dai, G.-P., P.H. Cooke, and S. Deng, *Direct growth of graphene films on TEM nickel grids using benzene as precursor*. Chemical Physics Letters, 2012. 531(0): p. 193-196.
32. Wood, J.D., et al., *Effects of Polycrystalline Cu Substrate on Graphene Growth by Chemical Vapor Deposition*. Nano Letters, 2011. 11(11): p. 4547-4554.
33. Han, G.H., et al., *Influence of Copper Morphology in Forming Nucleation Seeds for Graphene Growth*. Nano Letters, 2011. 11(10): p. 4144-4148.
34. Zhao, L., et al., *Influence of copper crystal surface on the CVD growth of large area monolayer graphene*. Solid State Communications, 2011. 151(7): p. 509-513.
35. Crommie, M.F., C.P. Lutz, and D.M. Eigler, *Imaging standing waves in a two-dimensional electron gas*. Nature, 1993. 363(6429): p. 524-527.
36. Eom, D., et al., *Structure and Electronic Properties of Graphene Nanoislands on Co(0001)*. Nano Letters, 2009. 9(8): p. 2844-2848.
37. Castro Neto, A.H., et al., *The electronic properties of graphene*. Reviews of Modern Physics, 2009. 81(1): p. 109-162.
38. Bunch, J.S., et al., *Impermeable Atomic Membranes from Graphene Sheets*. Nano Letters, 2008. 8(8): p. 2458-2462.
39. Stolyarova, E., et al., *Observation of Graphene Bubbles and Effective Mass Transport under Graphene Films*. Nano Letters, 2008. 9(1): p. 332-337.
40. Petersen, L., et al., *Screening waves from steps and defects on Cu(111) and Au(111) imaged with STM: Contribution from bulk electrons*. Physical Review B, 1998. 58(11): p. 7361-7366.
41. Schouteden, K., P. Lievens, and C. Van Haesendonck, *Fourier-transform scanning tunneling microscopy investigation of the energy versus wave vector dispersion of electrons at the Au(111) surface*. Physical Review B, 2009. 79(19): p. 195409.
42. Wessendorf, M., et al., *Electronic surface structure of n-ML Ag/Cu (111) and Cs/n-ML Ag/Cu (111) as investigated by 2PPE and STS*. Applied Physics A, 2004. 78(2): p. 183-188.

43. Bendounan, A., et al., *Modification of Shockley states induced by surface reconstruction in epitaxial Ag films on Cu (111)*. Physical Review B, 2003. 67(16): p. 165412.
44. Ogawa, Y., et al., *Domain Structure and Boundary in Single-Layer Graphene Grown on Cu(111) and Cu(100) Films*. The Journal of Physical Chemistry Letters, 2011. 3(2): p. 219-226.
45. Cho, J., et al., *Atomic-Scale Investigation of Graphene Grown on Cu Foil and the Effects of Thermal Annealing*. ACS Nano, 2011. 5(5): p. 3607-3613.
46. Zhang, Y., et al., *Defect-like Structures of Graphene on Copper Foils for Strain Relief Investigated by High-Resolution Scanning Tunneling Microscopy*. ACS Nano, 2011. 5(5): p. 4014-4022.
47. Ferrari, A.C., et al., *Raman Spectrum of Graphene and Graphene Layers*. Physical Review Letters, 2006. 97(18): p. 187401.
48. Dresselhaus, M.S., et al., *Perspectives on Carbon Nanotubes and Graphene Raman Spectroscopy*. Nano Letters, 2010. 10(3): p. 751-758.
49. Malard, L.M., et al., *Raman spectroscopy in graphene*. Physics Reports, 2009. 473(5-6): p. 51-87.
50. Ferrari, A.C., *Raman spectroscopy of graphene and graphite: Disorder, electron-phonon coupling, doping and nonadiabatic effects*. Solid State Communications, 2007. 143(1-2): p. 47-57.
51. Tuinstra, F. and J.L. Koenig, *Raman Spectrum of Graphite*. The Journal of Chemical Physics, 1970. 53(3): p. 1126-1130.
52. He, R., et al., *Large Physisorption Strain in Chemical Vapor Deposition of Graphene on Copper Substrates*. Nano Letters, 2012. 12(5): p. 2408-2413.

Chapter 3

Visualizing Individual Nitrogen Dopants in N-doped Graphene

3.1 Overview of Nitrogen Doped Graphene

Chemical doping is a powerful way to tailor the electronic properties of a host material via proper introductions of heteroatoms [1]. This technique has been used not only in semi-conductor industry as everyone knows [2], but also in graphitic materials such as graphite [3-7] and carbon nanotubes [8-11]. More recently, the discovery of graphene [12] made it possible to introduce this chemical doping method into inherently two dimensional (2d) systems [13], and it is expected to have fundamentally different consequences in altering the properties of such 2d host materials. In the last a couple of years, significant progresses in nitrogen doped (N-doped) graphene have been made in producing large-scale samples [14-34], characterizing structural/electronic properties [14, 16, 18, 24, 27], and initiating potential applications [26-28].

3.1.1 Fabrications of Nitrogen Doped Graphene

In recent years, several experimental techniques have been developed to dope the carbon lattices. These include methods applied during growth of large-area graphene films [15, 16, 18, 19, 22, 25, 26, 33, 34], and ways to modify the carbon materials after its growth [14, 17, 21, 23, 26, 29-32], as well as a new one-pot procedure to produce highly doped, few-layer graphitic structures [20].

The main approach used to directly synthesize large-area N-doped graphene is chemical vapor deposition (CVD) [16, 22, 24, 25]. In addition to the precursors that are used during pristine graphene growth, we introduce another precursor which includes nitrogen element. Shown in Fig. 3.1 is a typical CVD set up for synthesis of large-area N-doped graphene films on Cu foil substrates. The gray colored components stand for the ones same as in pristine graphene growth [35] while the yellow colored parts highlight the new ones specifically for N-doped graphene growth. The N-doped graphene films that we use in our experiment are grown in such a setup, with Cu foil as the substrate, methane as the carbon source, and ammonia as the nitrogen source. By tuning the ratio between methane and ammonia, we can well control the nitrogen concentration in the resulted graphene films. To be specific, the partial pressure of methane during growth is monitored to be 1.8torr while that for ammonia is selected to be any value in the range from 0.01torr to 0.15torr. As a result of these growth parameters, the nitrogen doping level in the graphene films ranges from $\sim 0\%$ to $\sim 0.5\%$. It is hard to achieve even higher nitrogen doping level, because the ammonia precursor starts to react strongly with Cu substrate and prevents the graphene growth when the ammonia partial pressure exceeds 0.15torr in this setup.

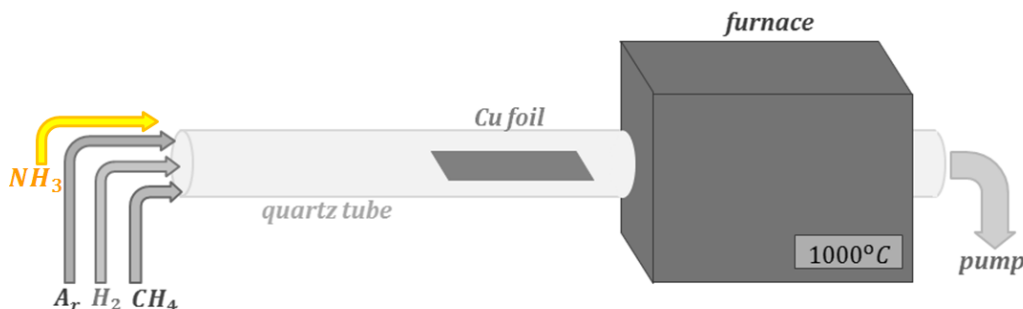


Fig. 3.1 Cartoon for Nitrogen doped graphene CVD growth setup, including three precursor gases, a quartz tube, a piece of Cu foil, a furnace and a mechanical pump. The gray background parts for pristine graphene growth while the yellow highlighted part for N-doped growth.

Apart from our recipe for N-doped graphene growth, other substrates [24] or precursors [25] have also been employed in producing N-doped graphene films. In fact, different growth recipes result in different doping forms of nitrogen dopants. It has been reported that using nickel (Ni) film as substrate and methane/ammonia ratio of 5:1 as precursor results in mainly pyridinic and pyrrolic nitrogen dopants in the graphene lattice [24]; however, if mixture of ethylene and ammonia is used as precursor while Cu foil is used for substrate, then the majority of the nitrogen dopants are in the pyridinic doping form [25]. Moreover, an atmospheric-pressure CVD growth with a mixture of methane and ammonia on Cu substrate is shown to produce di-graphitic-nitrogen dopants in graphene lattice [22]. Contrasting to these reports, our growth recipe produce graphitic nitrogen doped graphene films. Shown in Fig. 3.2 is a diagram including different nitrogen doping forms.

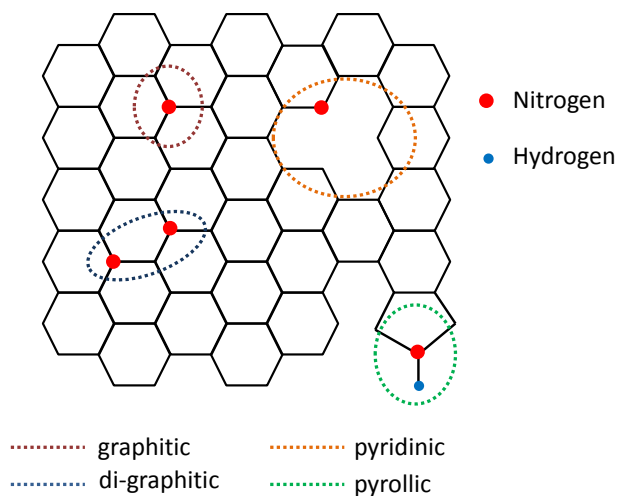


Fig. 3.2 Cartoon for different doping forms of nitrogen dopants in doped graphene films.

Post treatment is an alternative, other than direct synthesis, to produce N-doped graphene films, especially on the insulating substrates, such as mechanically exfoliated graphene on SiO_2/Si

substrate and epitaxial grown graphene on SiC substrate. There are a few approaches that are reported to dope pristine graphene films after their synthesis, mainly including thermal reaction [21, 32], ion implantation [21, 23, 29], and plasma treatment [30, 31]. Thermal reaction refers to heating graphene samples in ammonia environment at high temperature ($\geq 800^{\circ}\text{C}$), in which the nitrogen doping level is controlled by the annealing time and the ammonia pressure. It has been proven that this method mainly incorporate nitrogen into graphene lattice via pyridinic doping form [21]. In an ion implantation treatment, high energy ($\sim 50\text{-}500\text{eV}$) nitrogen ions (N^+) shoot onto the graphene surface, and then a post annealing ($\sim 800^{\circ}\text{C}$) process is applied in UHV. This method leads to a coexistence of pyridinic and graphitic nitrogen dopants. Depending on the energy and the flux of nitrogen ions, the ratio between the two doping forms and the overall nitrogen doping level are adjustable [29]. Plasma treatment is a popular way used to produce N-doped carbon nanotubes, and has been recently employed to synthesize N-doped graphene films, in which the carbon materials are placed in a nitrogen plasma atmosphere. The nitrogen concentration in graphene is controlled by the plasma strength and the exposure time as well. Different from the other two methods above, plasma treatment not only incorporates nitrogen into graphene as desired, but also introduce oxygen as a side effect. Notably, there is no up limit for the nitrogen doping level in these post treatment as long as the films preserve to be graphene-like. The reported values for nitrogen concentration reach up to $\sim 10\%$ [32] which is hardly possible for CVD approaches.

Of course, in addition to what we have mentioned, there are much more chemical ways to synthesize N-doped graphene films, for instance, segregation growth approach [33], arc-discharge approach [18], hydrazine solvo-thermal approach [34] and so on. More details can be found in a

recent review article about N-doped graphene in Ref. [26]. But in the following part of this chapter, we will focus on CVD grown samples.

3.1.2 Characterizations of Nitrogen Doped Graphene

Several characterization techniques, including x-ray photoemission spectroscopy (XPS) [24, 27], Raman spectroscopy [14, 16, 18], and transmission electron microscopy (TEM) [36], have been used to analyze the effects of the doping process in graphene.

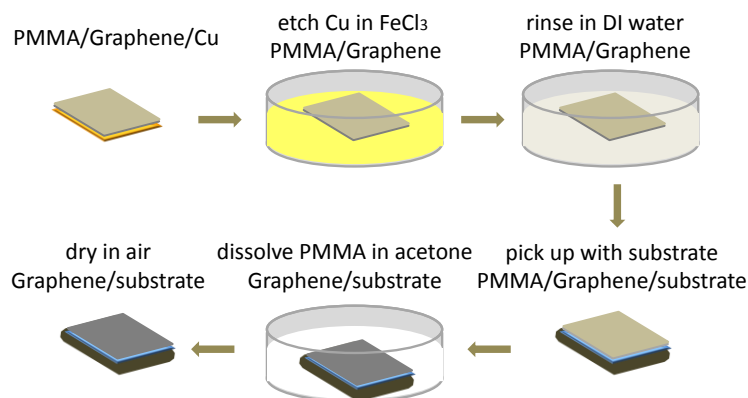


Fig. 3.3 Cartoon for transferring CVD grown graphene from Cu foil substrate to target substrate

Before walking through these reported characterizations on N-doped graphene, it is worth to briefly describe the procedure for transferring graphene from a growth substrate to an insulating substrate, as it is prerequisite for certain techniques such as Raman spectroscopy. Shown in Fig. 3.3 is a cartoon diagram of how to transfer graphene from a metal substrate to a target substrate. Firstly, coat a thin layer of polymer (2-6%PMMA dissolved in anisole) on the surface of graphene and dry it. Secondly, etch away the metal substrate by chemical solutions until PMMA/graphene floats on the solution. FeCl_3 solution or $(\text{NH}_4)_2\text{SO}_4$ solution is typically used for removing Cu and Ni

substrates. Thirdly, wash the PMMA/graphene in DI water a few times. Forth, scoop PMMA/graphene with the target substrate and dry them in air. Finally, etch away PMMA in acetone and dry it again in air.

XPS is the first choice to characterize N-doped graphene because it provides the species, concentrations, and configurations in the material. Specifically, the peaks at $\sim 400\text{eV}$ and $\sim 285\text{eV}$ in the XPS spectrum of N-doped graphene correspond to the transitions from N1s and C1s to π bands of graphene respectively. The ratio of N1s peak intensity to C1s one is used to determine the nitrogen doping level in the film. Moreover, the N1s peak can be further deconvoluted to several individual peaks which are assigned to pyridinic N ($\sim 398.6\text{eV}$), pyrrolic N ($\sim 400.5\text{eV}$) and graphitic N ($\sim 401.8\text{eV}$). Similarly, the ratio of the peak intensities between these N-related peaks indicates the concentration of each doping form.

Raman spectroscopy is an essential technique in N-doped graphene studies due to its power in graphene researches [37]. Although it could not provide specific element analysis, it is a good tool to probe the effects from chemical doping, such as impurity concentration and carrier doping level [38-40]. On one side, the incorporation of nitrogen atoms into graphene lattice is always accompanied by the introduction of defects, even for the graphitic doping form. Such defects lead to the appearances of D and D' peak in Raman spectra. According to Tuinstra-Koenig relation [41], the impurity concentration can be determined from the intensity ratio between D peak and G peak. On the other side, the nitrogen dopants are supposed to contribute free charge carriers into graphene whose concentration can be monitored by the G peak frequency shift [42, 43].

Comparing to XPS and Raman spectroscopy, TEM directly visualizes the structures of the nitrogen dopants in graphene lattice. Due to the local charge redistribution, a graphitic nitrogen

dopant shows as a triangle which is formed by the three nearest neighboring carbon atoms from the dopant site. Such graphitic nitrogen dopants are observed on the N-doped graphene grown by methane and ammonia precursors on Cu foil substrate [36]. In contrast to this, no nitrogen dopants are observed on the sample prepared on Ni films. Instead, a good number of stone-wales defects are detected [44].

3.1.3 Our Approaches to Study Nitrogen Doped Graphene

As learned from the literature, nitrogen dopants may get incorporated in graphene lattice in various doping forms, and their local distribution is expected to be inhomogeneous. Till now, a microscopic understanding of the atomic and low-energy electronic structure induced by the doping process in monolayer graphene is still lacking, so does the correlation between them. In our experiment, we used the atomic-resolution imaging capabilities of the scanning tunneling microscopy (STM) to probe the local structure in the vicinity of a nitrogen dopant in monolayer graphene and spectroscopic (STS) imaging to measure the density of states and carrier concentration at the nanoscale. Furthermore, the capability of taking STM/S at the same area correlates the structural and electronic characters of N-doped graphene. As a supplement to STM/S measurement, we also employ scanning Raman spectroscopy, core-level x-ray spectroscopy and first-principles calculations to characterize the effect of nitrogen-doping on the graphene films.

3.2 Topographic Characterizations of Nitrogen Doped Graphene

3.2.1 Structure of Individual Nitrogen Dopants

As soon as the N-doped graphene films are grown, they are transferred from CVD tube furnace into UHV chamber through ambient for STM/S characterizations. Then a gentle annealing process at

$\sim 350^\circ\text{C}$ for ~ 3 -4 hours is applied to the sample in order to get rid of any physisorbed species on the sample surface.

Shown in Fig. 3.4a is a large scale topographic image taken on N-doped graphene/Cu foil. Despite the background roughness from the Cu foil substrate, a good number of bright features are observed in addition to the honeycomb lattice. These bright features are almost identical and extend for a few atomic spacings [20, 45]. As a comparison, Fig. 3.4b shows a topography image taken on pristine graphene on Cu foil, where no extra features other than honeycomb lattice are observable. This indicates that these bright features in Fig. 3.4a are associated with nitrogen dopants. By counting the number of bright features at this area and associating each with a single nitrogen dopant, we arrive at a nitrogen doping concentration per carbon atom of 0.34%. We have taken same measurements across several similar samples and got nitrogen concentrations between 0.23 and 0.35%. More discussions of this will be shown in Section 3.2.2.

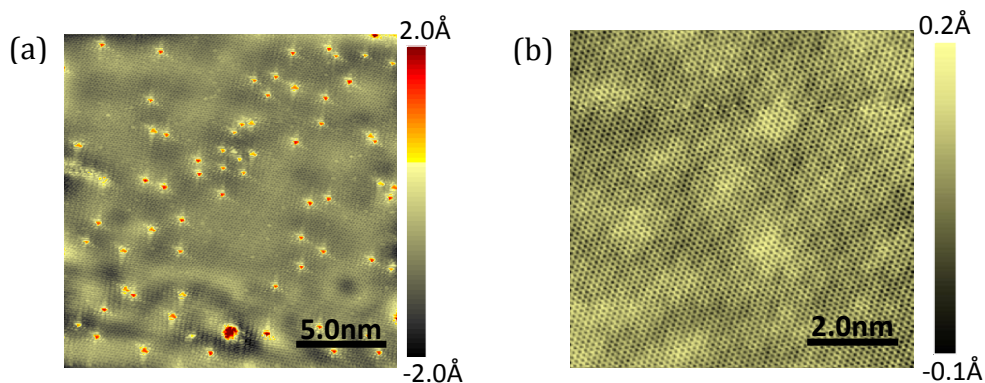


Fig. 3.4 Topography comparison between N-doped and pristine graphene. (a) STM image of N-doped graphene. Bright features are associated with nitrogen dopants. (b) STM topography of pristine graphene, showing perfect honeycomb lattice. $V_{bias} = 0.6\text{V}$, $I_{set} = 0.5\text{nA}$

A close-up topography of one of these doping features (shown in Fig. 3.5a) reveals three bright spots forming a triangle pattern. The distance between the bright spots is equal to the

graphene lattice constant of 2.46\AA . Far away from the doping feature, the honeycomb lattice of the graphene is recovered. As shown in Fig. 3.5b, we overlaid a lattice mesh on top of Fig. 3.5a, where the vortexes stand for the hollow positions of the honeycomb. Following the superimposed honeycomb lattice through the doping structure situates each of the three bright spots on a carbon atom of the

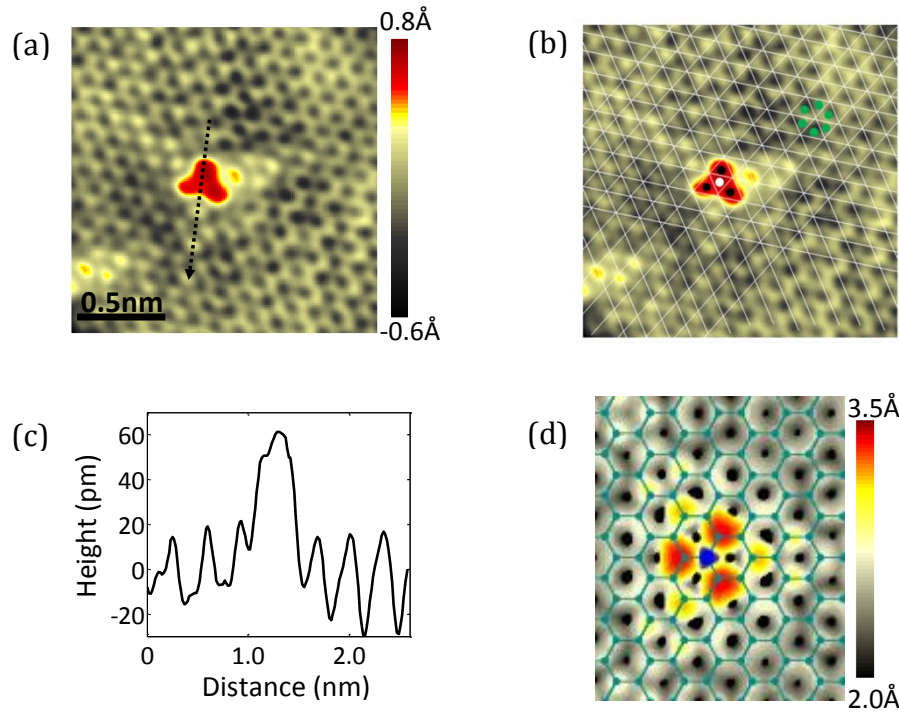


Fig. 3.5 Topography of individual graphitic nitrogen dopants. (a) STM topography of a single graphitic nitrogen dopant in graphene. (b) Graphene lattice overlaid on top of image in (a), the white dot marking the nitrogen position, three black spots labeling three nearest neighbors of N atom, and six green dots for six atoms in a Benzene ring. $V_{bias} = 0.6V$, $I_{set} = 0.5nA$ (c) Line profile across the nitrogen dopant, as marked in (a). (d) Simulated STM topography of a graphitic nitrogen dopant.

same sublattice (dark markers in Fig. 3.5b) and the center of the triangle on a carbon site in the opposite sublattice (white marker in Fig. 3.5b). A STM line scan through the dopant (Fig. 3.5c) yields a maximum apparent out-of-plane height of $0.6 \pm 0.2\text{\AA}$ and would be consistent with the

scenario of a nitrogen atom substituting for a carbon atom and staying in the plane of the graphene film. Therefore, we attribute such three-spot triangle features to the individual substitutional/graphitic nitrogen dopants in the honeycomb lattice. From sampling areas on several different N-doped graphene samples, we observe that more than 90% of the dopants are of this form. Moreover, the observed STM image closely matches our simulated STM image (Fig. 3.5d) computed from the local density of states for graphitic doping where one nitrogen atom replaces a single carbon atom, as well as other recent calculations[46]. The calculated STM image shows the bright features (red spots in Fig. 3.5d) on the nearest neighbor carbon atoms to the nitrogen dopant (blue marker in Fig. 3.5d). Visible features extend to several lattice spacings from the nitrogen dopant with an overall triangular symmetry, which all fit with the experimental results.

A larger area STM image, shown in Fig 3.6a, locates 14 dopants all in the graphitic doping form. Apart from the local structure around each dopant, we also see long three “tails” extending from each dopant. The “tails” are aligned 30° off the crystalline directions of the honeycomb lattice. In fact, these features arise from the inter-valley electron scattering induced by the nitrogen dopant, and similar features have been seen before in other experiments [47, 48]. The fast Fourier transform (FFT) of Fig. 3.6a is displayed in Fig. 3.6b, showing evidence of this strong inter-valley scattering. Two sets of points arranged in hexagons are observed in Fig. 3.6b. Whereas the outer hexagon of points in the FFT corresponds to the atomic lattice, the inner hexagon of spots in this FFT locates at the six Brillion Zone (BZ) corners, K_s and K' s. This indicates the origin of the inner hexagon is the electron scattering between Dirac cones. Further discussions about scattering physics of graphene in the vicinity of nitrogen dopants will be shown in Section 3.3.4.

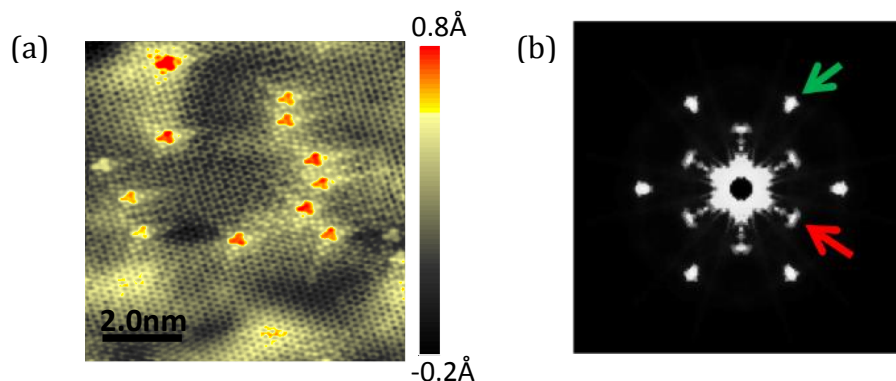


Fig. 3.6 “Tail” features in STM topography of N-doped graphene. (a) STM topography with 14 graphitic N dopants, showing three “tails” extending from each dopant site. (b) FFT of image (a), with outer hexagon for atomic lattice and inner hexagon for inter-valley scattering, the origin of the “tail”-feature in topography (a). $V_{bias} = 0.6V$, $I_{set} = 0.8nA$

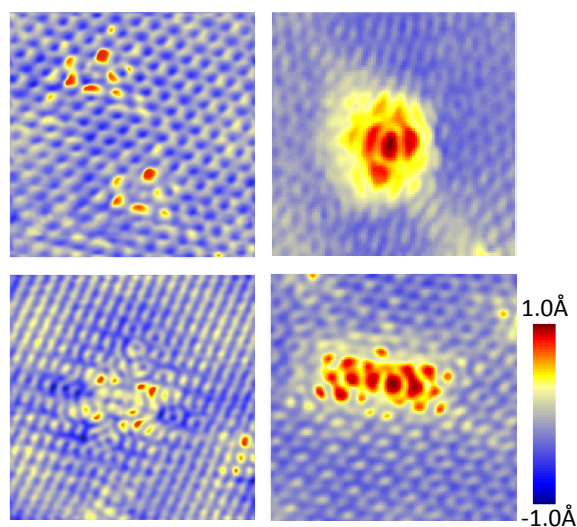


Fig. 3.7 STM topography of other defects observed in N-doped graphene films.

The STM topography surveys over multiple N-doped graphene films show that the majority of the doping occurs via graphitic substitutions. However, we indeed come across a few much more

complicated features in the samples. Shown in Fig. 3.7 are four examples of these complicated structures. The feature sizes are much larger than that of the graphitic nitrogen dopant, indicating that they may contain more than one nitrogen/impurity in the structures. In the literature, the other two commonly observed doping forms in N-doped graphene are pyridinic and pyrrolic forms. However, these features are nowhere close to an individual pyridinic N dopoant or a pyrrolic one. Since they only occur at a very low concentration, we have not taken deep investigations over them.

3.2.2 Distribution of Nitrogen Dopants

Having taking a careful look at the structure of individual nitrogen dopants, we zoom out to a larger scale to investigate their distributions in space, and in honeycomb lattice as well.

Large scale STM images, such as those in Fig. 3.4a and Fig. 3.6a, can give us information on whether clustering of nitrogen dopants occurs during growth. To analyze the possibility of dopant clustering, we use STM images to calculate the averaged cumulative number of dopants ($N(r)$) as a function of distance (r) from a dopant site. A statistical uniform distribution requires a quadratic relation between these two quantities, i.e. $N(r) = \rho r^2$. In fact, we surveyed eight different areas on different samples with various concentrations of nitrogen dopants, and plotted the relation for each area in Fig. 3.8. All of the eight plots fall in the same trend in Fig. 3.8, as highlighted by the gray band, although they may have slightly shifts from one to the other in x(or y) direction. The trend of the plot corresponds to the distribution form, while the slight shift arises from the different nitrogen concentrations. Fitting from plot in Fig. 3.8 indeed gives a power of two which is consistent with quadratic distribution. This confirms that the nitrogen dopants are uniformly distributed in space during the growth of N-doped graphene films.

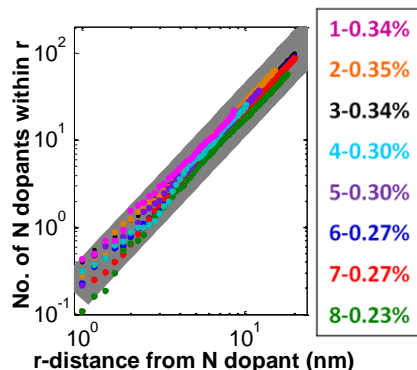


Fig. 3.8 Spatial distribution of nitrogen dopants on Cu foil with various N concentrations. The plot of cumulative number of N atoms as a function of distance from a N site falls in quadratic power law, indicating N dopants are uniformly distributed over the surface.

However, the nitrogen dopants are embedded in the honeycomb lattice of graphene, which endorses another freedom, sublattices, in the consideration of nitrogen distribution. In principle, nitrogen dopants can be in either A or B sublattice of graphene lattice, and the triangle feature formed by the nearest neighboring carbon atoms has 180° rotation with respect each other. Shown in Fig. 3.9 a and b are two cartoons displaying substitutions in A and B sublattices respectively and the orientations of resulted triangles.



Fig. 3.9 Cartoon for N dopants in A or B sublattice of graphene lattice. The triangle formed by the nearest neighboring carbon atoms is rotated 180° respective to each other.

The orientation of the triangle pattern is therefore used as an indicator for identifying in which sublattice the nitrogen dopants are. Noticing in Fig. 3.10a, all the 14 triangles orient in the same direction, indicating that all the 14 nitrogen dopants substitute the carbon atoms in the same

sublattice. To make a reliable statement on this surprising finding of sublattice segregation, we surveyed a number of different larger areas ($\sim 40 \times 40 \text{ nm}^2$) and present a typical one in Fig. 3.10b. There are in total 119 nitrogen dopants, in which 32 of them are in one sublattice and the remaining 87 are in the other sublattice. The uneven number of nitrogen dopants in two sublattices, together with their distribution in Fig. 3.10b, clearly supports that the nitrogen dopants prefer to substitute the carbon atoms in the same sublattice locally, at a length scale of at least 40nm.

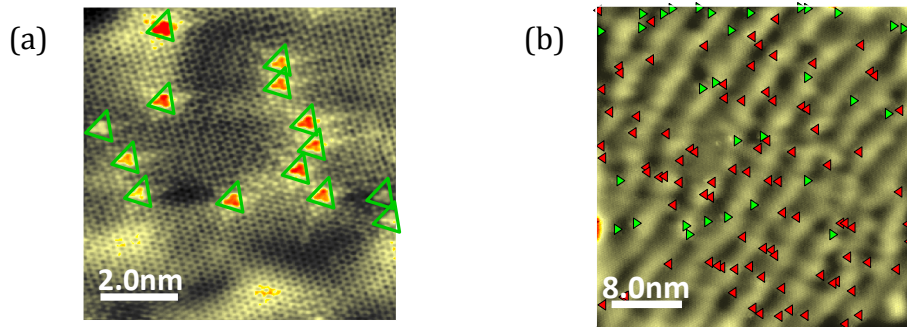


Fig. 3.10 N dopant distribution between A-B sublattices. (a) STM topography of 14 N dopants all in one sublattice of the honeycomb lattice. (b) Large scale STM image of 119 N dopants, with 87 of them in one sublattice and the other 32 in the opposite sublattice. Scanning conditions: $V_{bias} = 0.6V$, $I_{set} = 0.8 \text{ nA}$

A more thorough study on nitrogen dopant distribution between two sublattices reveals that nitrogen dopants in the same sublattice form domains with sizes beyond 100nm, and the boundaries between these domains are rather sharp, narrower than the average nearest dopants distance. The details of this study are not included in this thesis, but will be found in Ref. [49].

3.3 Electronic Characterizations of Nitrogen Doped Graphene

A chief purpose of chemically doping graphene is to modulate its electronic properties. Therefore, we performed detailed spectroscopic measurements of the differential conductance dI/dV to learn

the effect of the nitrogen atoms on the low-energy electronic structure of the doped graphene films. Here, dI/dV is the derivative of the current with respect to the voltage obtained using a lock-in amplifier. As described in Section 1.3.1, dI/dV spectrum is proportional to the local density of states (LDOS) where the spectrum is taken. Here, we not only performed individual dI/dV spectrum at fixed locations, but also dI/dV maps to probe the spatial variations in the LDOS.

3.3.1 Charge Carrier Injection from Nitrogen Dopants

The most prominent feature seen in all of the dI/dV curves, which have been observed previously in monolayer graphene on SiO_2/Si and BN [50, 51], are two depressions near zero bias and -300meV relative to the tip potential. An example of such dI/dV curves is shown in Fig. 3.11a, where the black spectrum is obtained by averaging over 64×64 dI/dV curves taken over a $40 \times 40\text{nm}^2$ area. The first depression at zeros bias (marked by yellow arrow in Fig. 3.11a) occurs when the energies of the tunneling electrons are too low to excite the optical phonon mode at a momentum of K in graphene monolayers that can enhance the tunneling current [50]. The second depression at -300meV (marked by red arrow in Fig. 3.11a) occurs near Dirac point where the DOS is low [12]. As reported in Ref. [50], the actual Dirac point shift relative to Fermi level (zero bias energy) should be the energy value for the second depression subtracted by the optical phonon energy (63meV).

Apart from this phonon-assisted inelastic tunneling process, there are reports about direct tunneling process in STM measurements of graphene [52-54], in which only one depression is observable in dI/dV spectrum and happens at the Dirac point. In fact, the total tunneling current is the summation of currents from both tunneling processes, but the ratio between the two tunneling probabilities are determined by the tip geometry. Based on the Heisenberg uncertainty rule, electrons tunneling from a blunt tip have a narrow distribution of parallel momentum around zero.

Due to the momentum conservation in the tunneling process, these electrons can only tunnel into the states at Dirac cones of graphene by gaining the desired momentum of K through inelastic scattering with optical phonons at momentum of K. However, the electrons from a sharp tip have a wide distribution of the parallel momentum, some of which may have large enough parallel momentum to directly tunnel into the states at Dirac cones. Shown in Fig. 3.11b is a cartoon for the dI/dV spectrum resulted from the two tunneling processes, where the two Dirac associated depressions are 63meV apart from each other. In a real situation, when both tunneling processes

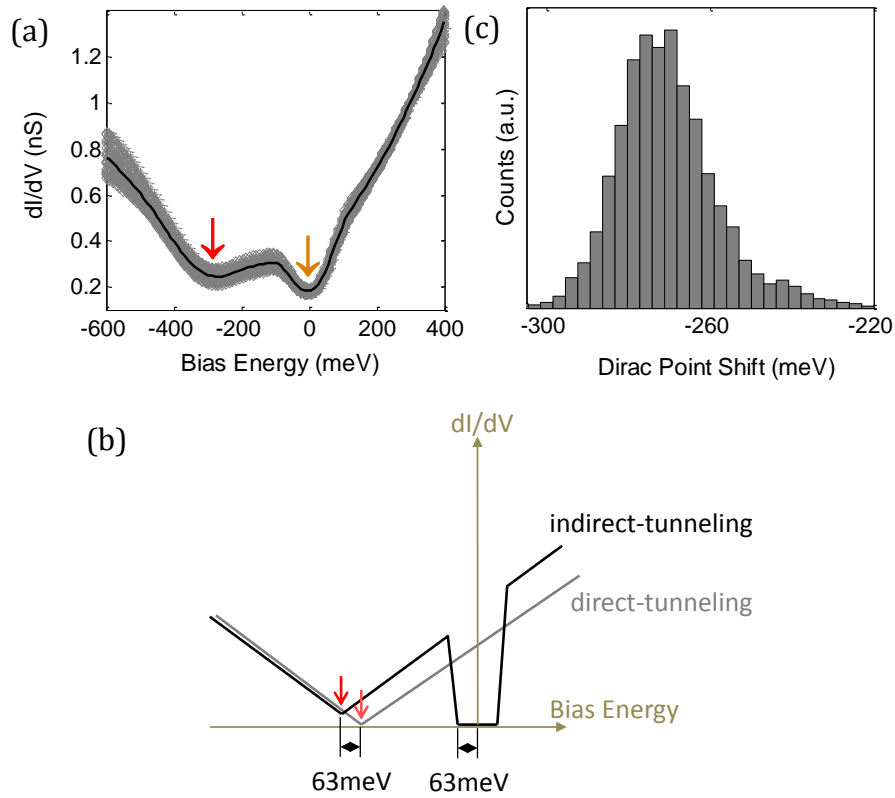


Fig. 3.11 Dirac point shift relative to Fermi level in vicinity of graphitic N dopants. (a) Spatially averaged dI/dV spectrum (dark line) with variations (gray band) over the area ($40 \times 40 \text{ nm}^2$) where the measurements were taken, with red arrow and orange arrow indicating the Dirac-associated and phonon-induced depressions in the spectrum. Scanning conditions: $V_{bias} = 0.5V$ and $I_{set} = 0.8nA$ (b) Cartoon diagram showing two tunneling processes. (c) Histogram of spatial variations of Dirac point shifts in the area.

have comparable chances to happen, the Dirac-related depression could be at any energy between the two extreme cases. Our results belong to such a catalogue since the gap at zero bias is not well defined as that in Ref. [50]. The fitted value for the position of second depression is at $\sim -300\text{meV}$, but we took the value in middle of $(-300\text{meV}, -240\text{meV})$ as the real Dirac point shift with an uncertainty of 30meV , $E_D = -270 \pm 30\text{meV}$. A statistical distribution of Dirac point energies extracted from the spectra in Fig 3.11a is shown in Fig. 3.11c, in which the mean is around -270meV , and the full width of half maximum (FWHM) is approximately 30meV . As the Dirac point is 270meV below the Fermi level, the N-doped graphene samples are electron-doped.

We use the energy of the Dirac point measured at each position of a sample to convert to a charge-carrier density at that location using the ideal graphene band structure, namely,

$$n = \frac{E_D^2}{\pi(\hbar v_F)^2}, \quad (3.1)$$

where n is the charge carrier density, E_D is the Dirac point shift with respect to Fermi level, and \hbar is Plank's constant h divided by 2π . Taking a value for the Fermi velocity $v_F = 1.0 \times 10^6\text{m/s}$, we arrive at an average charge-carrier density of $(5.42 \pm 0.83) \times 10^{12}$ electrons per cm^2 . Meanwhile, the nitrogen dopant concentration can be calculated by simply counting the number of observed dopants in the area where the measurements are performed. The observed nitrogen doping in this area corresponding to 0.34% nitrogen atoms per carbon atom, or equivalently, a nitrogen dopant density of $1.3 \times 10^{13}\text{cm}^{-2}$. Together with the charge-carrier density measured by STS, this results implies that each graphitic nitrogen dopant contributes (on average) $\sim 0.42 \pm 0.07$ mobile carriers to the graphene lattice. We have performed such detailed STM/S measurements across different samples with nitrogen concentrations varying from 0.23% to 0.35% (Fig. 3.12a) and found a strong correlation between the nitrogen dopant concentration and the extracted charge-carrier density.

The averaged charge-carrier doping rate per graphitic nitrogen is $\sim 0.5e/N$, as shown in the inset of Fig. 3.12a.

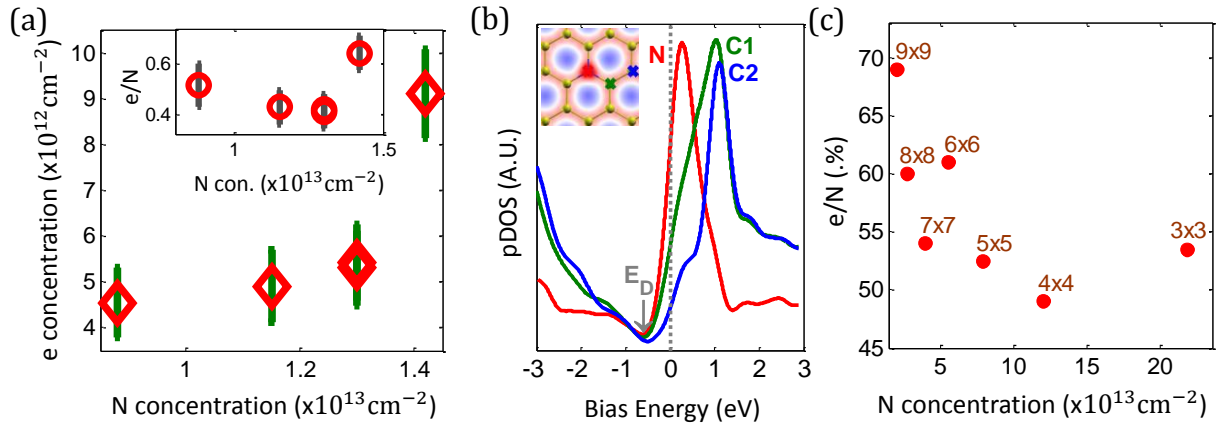


Fig. 3.12 Average charge carrier (electron) doping rate by N dopants. (a) Spatially-averaged charge carrier concentration as a function of N dopant concentration for five different samples. (Inset) Free charge carrier per N atom for each of the five samples. (b) Calculated projected DOS near Fermi level for 1% doping. (c) Calculated charge carrier doping rate for different N doping levels (obtained by varying the super-cell in calculations as indicated by the labels next to every plot)

Our DFT calculations provide insight to the electrostatic balance between the nitrogen dopants and free carriers in the graphene sheet. Focusing on a single, graphitic nitrogen dopant, the projected nitrogen density of state (pDOS) on the π -system (Fig. 3.12b) revealed a resonance caused by the nitrogen p_z orbital centered 0.3eV above the Fermi level. The pDOS for the carbon nearest neighbor exhibited a shoulder caused by its electronic coupling to the nitrogen, with a reduced shoulder on the next nearest neighbor. The occupied fraction of these resonances represented the localized charge near the nitrogen centers. The balancing charge went to the rest of the π states. The Dirac point still appeared in the pDOS, shifted to below Fermi level, as also seen in our total DOS and in other recent calculations [46, 55]. Furthermore, we studied nitrogen

concentrations from 0.6% to 5.6% by varying the super cell size for a single nitrogen dopant. Using the Dirac point shift in the total DOS as a measure of free electron concentration, we estimate that 50% to 70% of the extra electron from a N dopant is delocalized (Fig. 3.12c), with oscillations indicative of electronic interference effect in the simulation cells that we used. A value of $\sim 60\%$ would be consistent with the experiment values shown in Fig. 3.12a.

To draw comparisons with other measurements of doping in graphene films, it is important to understand the effect of the Cu foil substrate on the carrier concentration via charge transfer [56, 57], as well as by changing the charge screening in the graphene layer. We performed STM measurements of pristine graphene films on Cu foils and estimated that the doping induced by the Cu foil substrate into the graphene film is less than 10^{12} electrons/cm², as shown in Fig. 3.13a. The Cu substrate can also modify the charge screening length in the graphene film, we studied nitrogen doped graphene films transferred to a SiO₂/Si dielectric substrate [58], a process that may leave residue on or below the graphene surface. Typical STM and atomic force microscopy images display surface roughness of a few nanometers, but occasionally we found a small region of the sample where the graphene honeycomb lattice could be resolved. Fig. 3.13b shows the averaged dI/dV spectrum taken over one of such clean areas (the STM image is shown in the inset in the derivative mode to remove the overall roughness of the substrate and enhance the atomic contrast). The overall features in the spectrum are preserved, but now $E_D = -330 \pm 30 \text{ meV}$ ($n = 8 \times 10^{12} \text{ cm}^{-2}$). The transfer processes, as well as the SiO₂ substrate itself, introduce an unknown doping concentration into the film; thus, it is not possible to directly compare the doping level of the two samples. However, the spectrum of doped graphene on SiO₂ is broadly consistent with the spectrum of doped graphene on Cu foil, indicating the absence of a strong hybridization between the graphene and underlying Cu substrate.

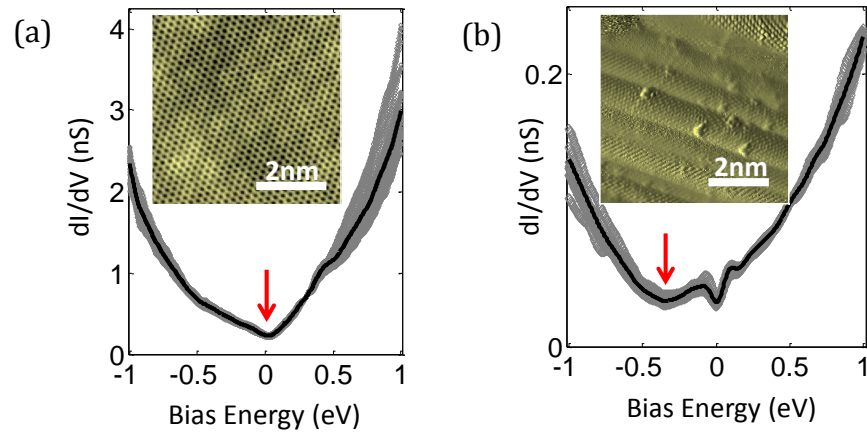


Fig. 3.13 Effects of Cu foil on the electronic structures of N-doped graphene films. (a) Spatially averaged dI/dV (dark line) spectrum with variations (gray band) taken over a $12 \times 12 \text{ nm}^2$ area on pristine graphene/Cu foil. (Inset) STM topo of pristine graphene/Cu foil. $V_{bias} = 1.0 \text{ V}$, $I_{set} = 1.5 \text{ nA}$ (b) Spatially averaged dI/dV spectrum (dark line) with variations (gray band) taken on a $12 \times 12 \text{ nm}^2$ area on N-doped graphene/ SiO_2 . (Inset) STM topo of such transferred sample. $V_{bias} = 1.0 \text{ V}$, $I_{set} = 0.1 \text{ nA}$.

3.3.2 Band Gap Opening or Not?

Recent literatures claim that sufficient doping of nitrogen in graphene films leads to a band gap opening around Dirac point, because the presence of nitrogen atoms breaks the A-B sublattice symmetry of honeycomb lattice [59]. Therefore, it is worth to revisit our results from this perspective when writing this thesis.

Indeed, from STM topography of the single graphitic nitrogen dopants, it is clear that the sublattice symmetry has been broken at least around the dopant site. In Fig. 3.14, we highlighted the bright spots around a nitrogen dopant with green dots, and found that these spots are all at carbon sites on the same sublattice of graphene lattice. Only a couple of lattice constants away from the dopant site, the sublattice symmetry got recovered as evidence by the equal apparent heights at A and B sites (i.e. perfect honeycomb structure).

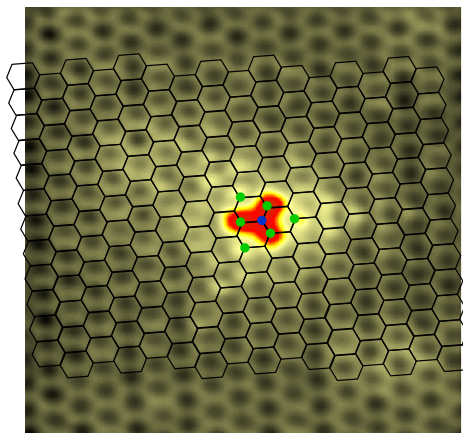


Fig. 3.14 Sublattice asymmetry induced by the presence of graphitic N dopant. A STM image with honeycomb lattice overlaid on top shows that the intensity on one sublattice around N dopant is stronger than that on the other sublattice (as marked by green dots) while the equal intensity on both sublattices is found far away from the dopant site (perfect honeycomb lattice).

Whether such local A-B sublattice asymmetry introduces a band gap around Dirac point is investigated by taking dI/dV spectrum carefully around the nitrogen dopant site. As shown in Fig. 3.15, the dI/dV curves were measured at nitrogen site, first, second, fourth bright spots and $\sim 2\text{nm}$ away from the feature. The two-depression feature is clearly visible in all the spectrum and the positions of the Dirac points are aligned at the same energy, indicating the delocalized nature of the charge carriers. However, there is no “GAP”-feature around Dirac point in any of the spectrum, even the ones where the sublattices are asymmetric.

The absence of energy gap at Dirac point, against the recent theory predictions [59], can be explained by the combination of low nitrogen concentration and lack of energy resolution in our setup. Graphitic nitrogen dopants in graphene breaks sublattice symmetry in such a weak way that nitrogen doping level as high as $\sim 2\%$ only introduces a sublattice asymmetry of $\sim 100\text{meV}$, equivalently, a band gap of $\sim 100\text{meV}$ [59]. According to this, a doping level of $\sim 0.3\%$ is supposed to

open a band gap of $\sim 10\text{meV}$. Unfortunately, two factors in our STM setup may limit us to observe such a band gap even if it is in presence. The first one is thermal broadening effect. Our experiments are performed at 77K, where the thermal energy is in order of $kT \sim 7\text{meV}$, comparable size of the gap feature. Secondly, the activation energy used in Lock-in measure dI/dV spectrum was set to $\sim 10\text{meV}$, which may also obscure the band gap feature.

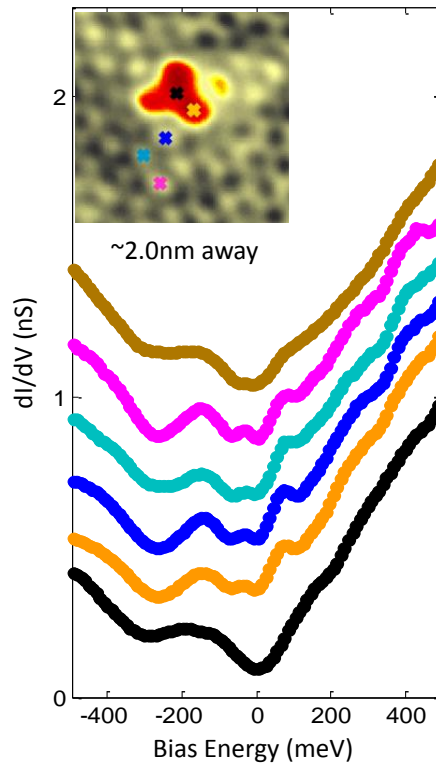


Fig. 3.15 dI/dV spectra taken on a N atom and the bright topographic features around N atom on N-doped graphene/Cu foil, offset vertically for clarity. The top curve is taken $\sim 2\text{nm}$ far away from the N dopant site. (Inset) Positions where the spectra were taken. Scanning conditions: $V_{bias} = 0.8V$, $I_{set} = 1.0nA$.

3.3.3 Perturbation to Local Electronic Structures

As evidenced in the STM topography of a graphitic nitrogen dopant (shown in Fig. 3.15), the electronic structure around the dopant site has been perturbed due to the presence of nitrogen,

which may affect the electronic nature of the doped graphene film. In the following, we analyze such local electronic perturbations around a dopant through STS map measurements.

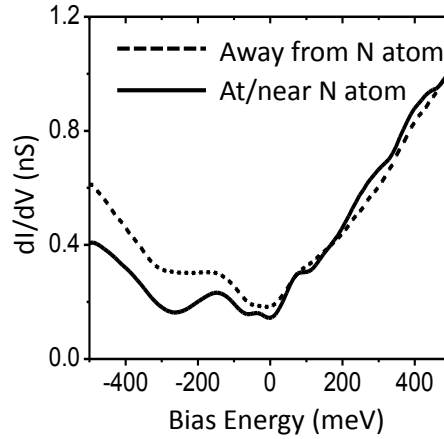


Fig. 3.16 dI/dV spectra taken on a N atom and $\sim 2\text{nm}$ away from the N atom on N-doped graphene/Cu foil, showing an enhancement of electron-hole asymmetry at/around dopant site. Scanning conditions: $V_{bias} = 0.8V$, $I_{set} = 1.0nA$.

In Fig. 3.16, we show spectra obtained on and far away ($\sim 2\text{nm}$) from a dopant atom. Although the overall features of the spectra were preserved on the nitrogen atom, the electron-hole asymmetry in the local density of states (LDOS) was much stronger on the nitrogen atom, in accord with the DFT calculations (Fig. 3.12b). This enhanced electron-hole asymmetry at the dopant site can be explained by sub-critical Coulomb interaction in a Dirac fermion system [60], in which the nitrogen dopants can be considered as a positive charged impurity and an extra electron. The absence of resonances in dI/dV spectra indicates no quasi-bound states formed around the nitrogen dopants, consistent with the theory of a subcritical Coulomb impurity. Moreover, the nitrogen dopants tend to attract negative charged carriers (above E_D) and repel positive charge carriers (below E_D), which requires more (less) DOS below (above) Dirac point to host the excess (depletion) of charge carriers, resulting in the enhanced electron-hole asymmetry.

To study the spatial evolution of this electron-hole asymmetry, we performed STS mapping in a 2.5-nm area centered at one graphitic nitrogen dopant. Shown in Fig. 3.17a are a set of these maps, acquired at bias voltages from -1.0V to +1.0V. The maps did not show much contrast at high positive bias, but the LDOS around the nitrogen atom was strongly suppressed at energies below the Fermi level. The LDOS recovered its background value within a few lattice constants from the dopant site. We plotted, in Fig. 3.17b, the radial distribution of the dI/dV intensity from the set of maps in Fig. 3.17a as a function of distance from the nitrogen atom, normalizing the background value of the dI/dV to unity for each energy. The variations in the intensity of spectral weight that are caused by the nitrogen dopant were energy dependent, but the decay lengths were $\sim 7\text{\AA}$ for all energies, as shown in Fig. 3.17c.

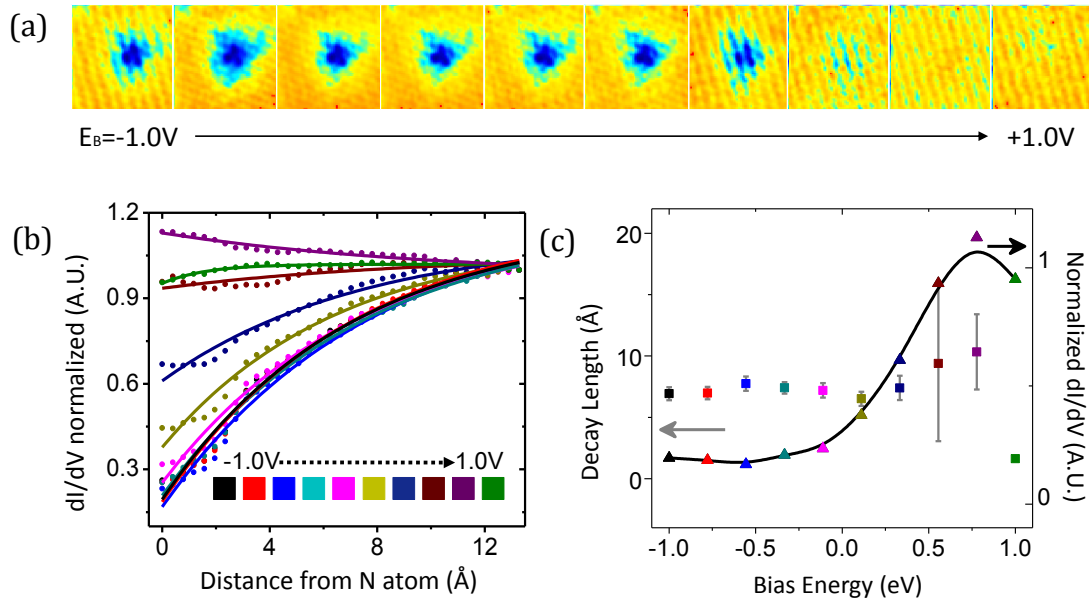


Fig. 3.17 Spectroscopic mapping around a single dopant. (a) STS maps taken in vicinity of a single N dopant ($2.5 \times 2.5\text{nm}^2$) at various bias energies from -1.0V to +1.0V. (b) Radially averaged differential conductance as a function of distance from N atom site, normalized to unity at distance far away from N site. (c) Extracted decay (squares) length for all the energies and the ratio (triangles) of the dI/dV on N site to the background. Scanning conditions: $V_{bias} = 0.8V$, $I_{set} = 1.0nA$.

3.3.4 Quantum Interferences in the Presence of Nitrogen Dopants

Scattering is another electronic effect that results from the presence of impurities/defects in a host lattice [1]. Revisiting the electronic band structures of graphene, two kinds of scattering processes may occur in the vicinity of nitrogen dopants. One is the scattering happening within a Dirac cone, which involves small momentum changes. The other one happens between two Dirac cones with large momentum changes. The diagrams of the two scattering processes are shown in Fig. 3.18. Usually, the former is referred to as intra-valley scattering while the latter is inter-valley scattering.

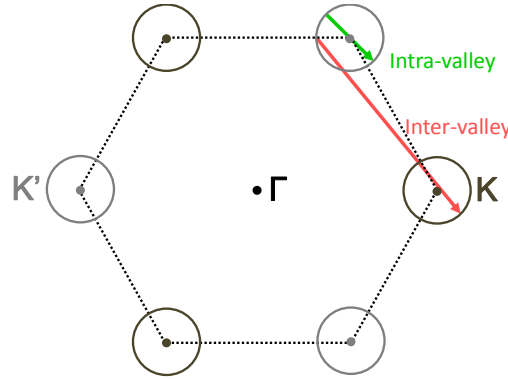


Fig. 3.18 Cartoon diagram for intra-valley and inter-valley scatterings.

Shown in Fig. 3.19a and b are a STM topography on a $50 \times 50 \text{ nm}^2$ area and the dI/dV map taken at the same area respectively. The tiny bright spots in Fig. 3.19a are individual graphitic nitrogen dopants, one of which is highlighted with a red arrow. A FFT of Fig. 3.19b is displayed in Fig. 3.19c. The hexagon of six spots results from the inter-valley scattering (the short wavelength pattern hardly visible in Fig. 3.19b) while the center brightness is related to intra-valley scattering (the long wavelength fluctuations in Fig. 3.19b). Since the two scattering processes happen at quite

different real-space length scales, we will discuss them separately in the following at proper length scales.

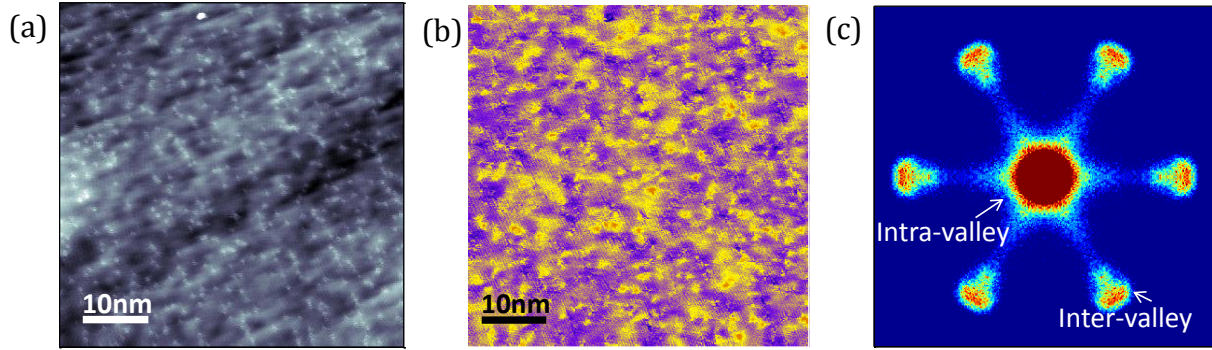


Fig. 3.19 Coexistence of inter-valley and intra-valley scattering in N-doped graphene films. (a) STM topography of a $50 \times 50 \text{ nm}^2$ area on N-doped graphene/Cu foil. (b) Differential conductance map at the area in (a). (c) FFT of image (b) showing wave vectors of both inter- and intra-valley scattering. Scanning conditions: $V_{bias} = 0.1 \text{ V}$, $I_{set} = 0.2 \text{ nA}$

Inter-valley scattering happens at a wavelength of $\sqrt{3}a$ ($a = 2.46 \text{ \AA}$). Therefore, a proper scale of STM/S image to visualize it in real space is $\sim 10 \text{ nm}$. Fig. 3.20a and b display topographic and dI/dV images on an area of $12.5 \times 12.5 \text{ nm}^2$, with 22 graphitic nitrogen dopants. A FFT (inset in Fig. 3.20b) of Fig. 3.20b shows an outer set of hexagon for atomic lattice and an inner set of hexagon for inter-valley scattering. To focus on the inter-valley scattering, we filtered out the information of atomic lattice from Fig. 3.20b, and show only the scattering pattern in Fig. 3.20c. The intensity of inter-valley scattering pattern clearly varies over space. Thus, we plotted the auto-correlation (Fig. 3.20d) of Fig. 3.20c. In an auto-correlation map, the periodicity of the peaks indicates the wavelength of the inter-valley scattering interference pattern averaged over the imaged area, and the intensity indicates the decay trend of the interference pattern in real space. A line cut of through the center of this auto-correlation map is displayed at the bottom in Fig. 3.21a (+0.5 eV curve),

normalizing the first peak intensity to unity. Similarly, we plotted in Fig. 3.21a a set of line-cuts from auto-correlation maps at bias energies from -0.5eV to +0.5eV. All the spectra show similar periodicities and decaying envelopes. In Fig. 3.21b, we plot the normalized peak intensities as a function of peak positions for all the spectra in Fig. 3.21a. The plots all fall in the same trend, $\sim 1/r$, independent of bias energy, which is in accordance with the theory prediction of back-scattering in monolayer graphene [61-63].

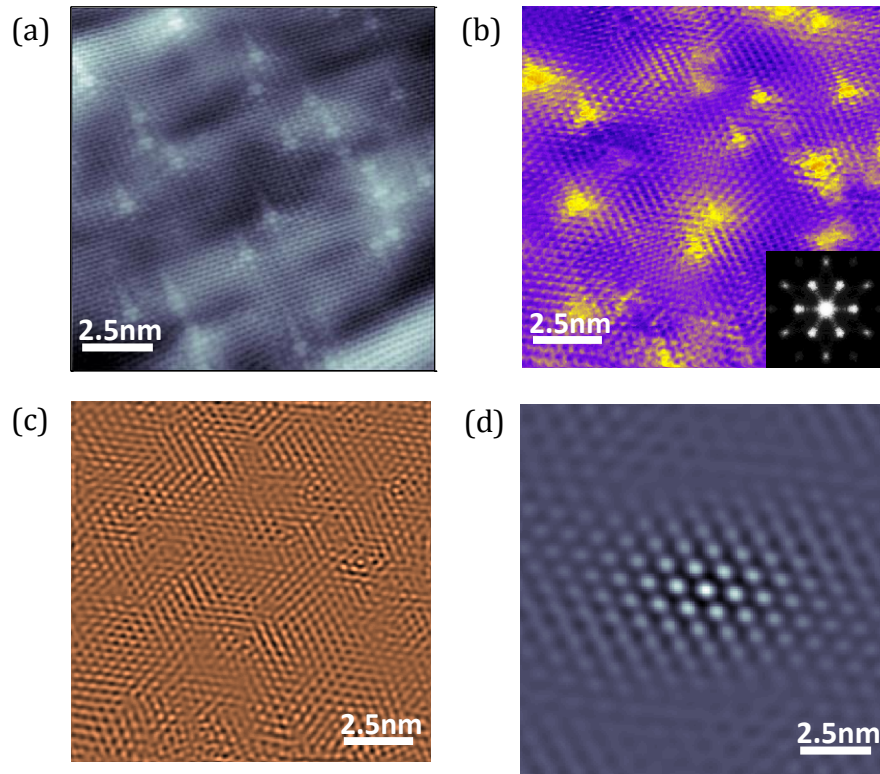


Fig. 3.20 Inter-valley scattering in N-doped graphene/Cu foil. (a) STM topography of an area with 22 graphitic N dopants. (b) dI/dV map taken at the same area as in (a). (Inset) FFT of image (b) showing an outer set hexagon for atomic lattice and an inner set hexagon for inter-valley scattering. (c) Filtered dI/dV map from (b) with only scattering information but not atomic information. (d) Auto-correlation of image (c) showing periodicity and decay pattern. Scanning conditions: $V_{bias} = 0.5V$, $I_{set} = 1.0nA$

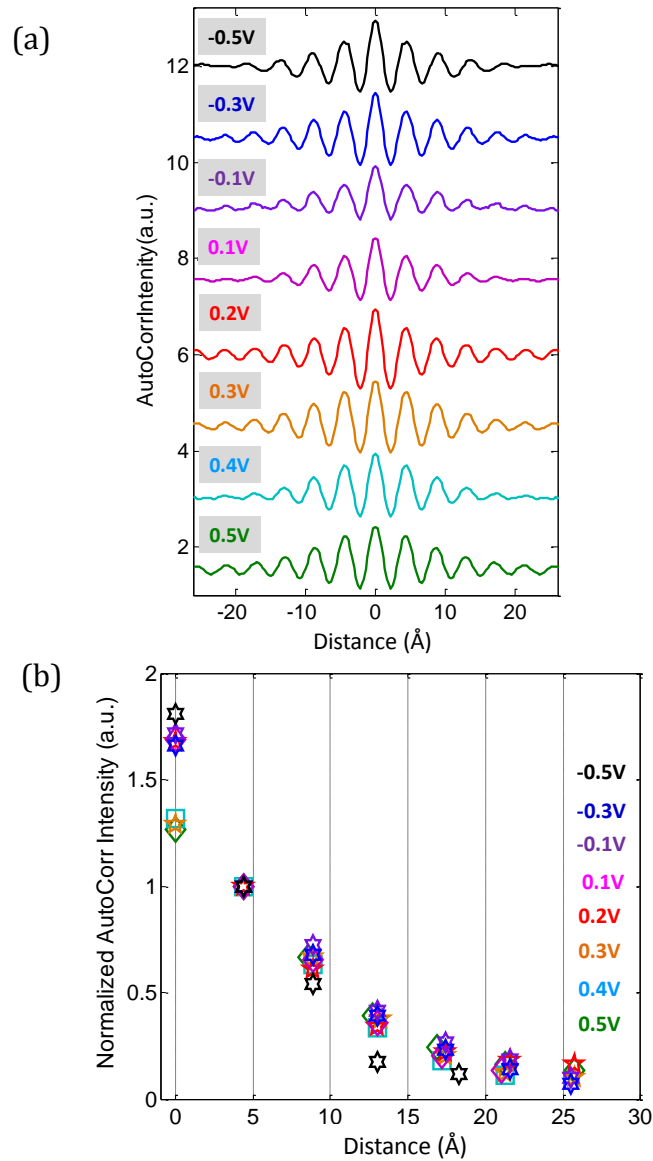


Fig. 3.21 Decay of inter-valley scattering. (a) Line-cuts through the center of auto-correlation maps at various bias energies. (b) Extracted peak values and positions in the line-cuts in (a) at different bias energies, normalized to unity at the first peak.

Intra-valley scattering interference patterns for monolayer graphene have been shown to have periodicity of a few nanometers [47, 64]. Zooming out to a larger scale of $50 \times 50 \text{ nm}^2$, we show a set of dI/dV maps at bias energies from -0.5V to +0.5V taken at the same area in Fig. 3.22.

The FFT of each map is also shown in the inset of the corresponding map. The FFT shows an obscure disk in the center, rather than a well-defined ring-like feature as reported in Ref. [64]. However, the radius of the disk does depend on the energy, which decreases gradually from +0.5V to ~ -0.3 V and increases again from -0.3V to -0.5V. This observation indicates the Dirac point is at ~ -0.3 eV respect to Fermi level, which is consistent with our findings Section 3.3.1.

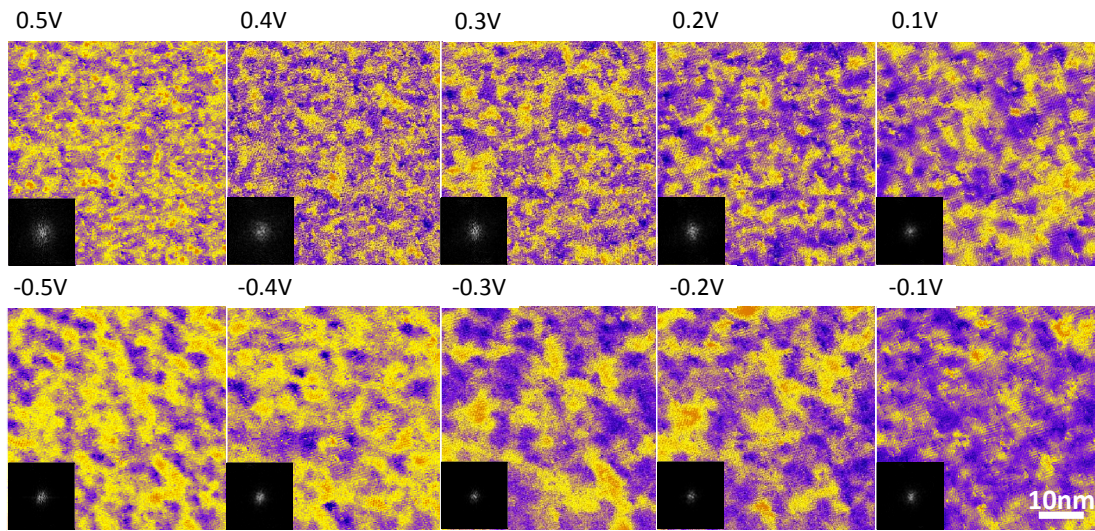


Fig. 3.22 Intra-valley scattering in N-doped graphene/Cu foil. dI/dV maps taken at an area of 50nm by 50nm on N-doped graphene/Cu foil, at different bias energies ranging from -0.5V to +0.5V. (Inset) FFT of each dI/dV map showing a disk-like pattern with its radius changing over bias energies.

In fact, there are a couple of arguments about intra-valley scattering in monolayer graphene in the literature. Ref. [61] predicts that the intra-valley scattering in monolayer graphene decays as $1/r^2$, different from the conventional materials that decays at $1/r$. As a result, the FFT of inter-valley scattering interference pattern shows a disk-like feature. This prediction has been proven by *G.M. Rutter et al* that only a disk feature in FFT is observed for monolayer graphene on SiC while a ring feature in FFT is captured in bilayer graphene [47]. However, in contrast with this, *Y.B. Zhang et al*

reported a ring feature in FFT for monolayer graphene on SiO₂/Si [64]. At this stage, it seems our results are in agreement with Ref. [47] and [61].

3.4 Raman Characterizations of Nitrogen Doped Graphene

While STM/S is a powerful technique with which to extract the information about electronic structure and doping on nanoscale, it is also important to characterize the electronic homogeneity of the films on the micrometer scale [38, 40, 65]. To address this issue, we performed scanning Raman spectroscopy measurements on three samples including pristine graphene, nitrogen doped graphene with ammonia partial pressure of 0.1 torr and 0.13 torr (short written as PG, NG10, NG13).

Shown in Fig. 3.23a are typical Raman spectra taken at different locations on NG10. All the spectra show the G and 2D bands for pristine graphene [37], as well as the D and D' bands usually seen in the presence of defects [38]. However, we see that different locations of the sample exhibit different peak magnitudes and frequencies. In particular, some spectra display characteristics of a low carrier/defect density (bottom curve – high 2D/G ratio, small D/G and D'G ratios), while other spectra show the presence of more dopants (top curve). To better understand the spatial inhomogeneity, we performed these spectroscopic measurements at every 1 μm of the PG, NG10 and NG13 samples over a $80 \times 80 \mu\text{m}^2$ areas. Shown in Fig. 3.23b are maps of the ratio of 2D/G peak heights, extracted from the spectral maps. In previous studies on pristine graphene, this ratio was shown to be sensitive to the carrier and defect concentration in the film. We see firstly that the PG sample shows a much higher 2D/G ratio on average, indicating fewer defects or dopants in the film. The doped samples clearly show the presence of micrometer-sized patches with higher nitrogen concentration on average. Furthermore, we noticed that the size of the patches is doping level

dependent, indicating that the patches are truly related to the local dopant concentration. These conclusions are supported by the analysis of the G band frequency which is correlated to the amount of charge carriers present in the sample [66, 67]. Shown in Fig. 3.23c are maps of G peak frequency taken at the same area as in Fig. 3.23b. Histogram of G peak frequencies for each sample is shown in Fig. 3.23d. We see a clear shift in the frequency of the G peak across the samples, consistent with the fact that charge carrier concentration increases as nitrogen doping level increases. The G peak shift of $\sim 1.8\text{cm}^{-1}$ between pristine graphene and NG10 (which is used for STM measurements) corresponds to a carrier concentration of $\sim 5 \times 10^{12}\text{cm}^{-2}$, which agrees very well with STM findings of $5.4 \times 10^{12}\text{cm}^{-2}$.

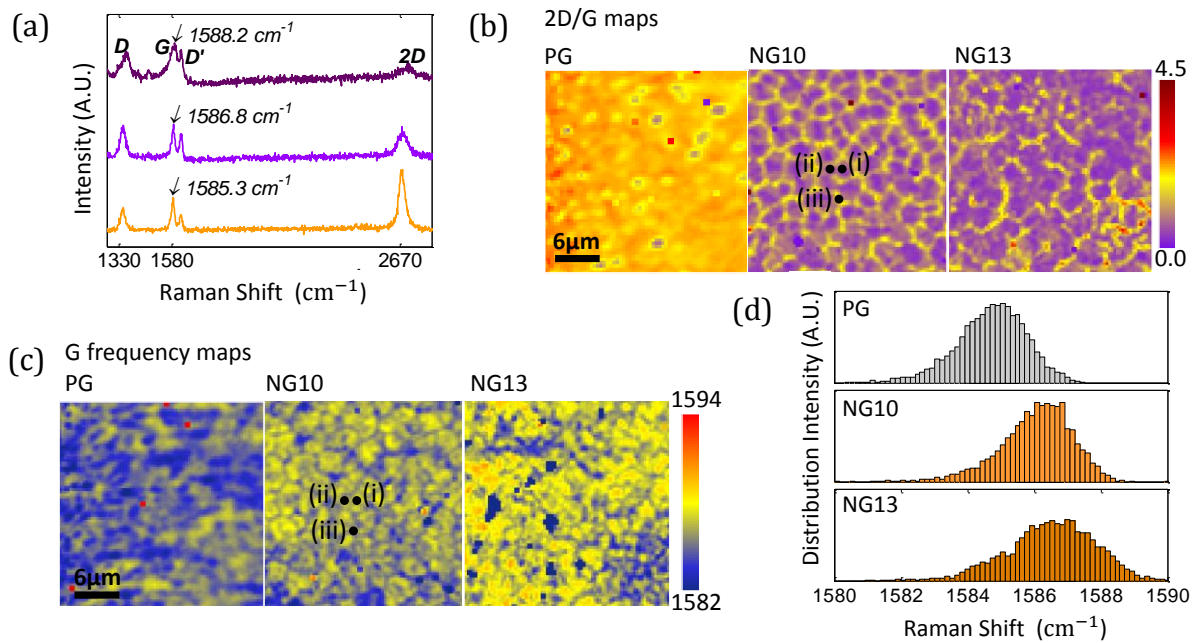


Fig. 3.23 Raman spectra of N-doped graphene/ SiO_2/Si . (a) Three Raman spectra taken at various spots on sample NG10, showing differences in the signature peaks. (b) 2D/G maps for pristine, NG10, and NG13 samples. (c) G peak frequency maps taken on pristine, NG10 and NG13 samples. (d) Statistics of G peak frequency for pristine, NG10 and NG13 samples, showing a blue shift as the N concentration increases.

More details about spatial inhomogeneity of nitrogen concentration will be discussed in Chapter 5.

3.5 NEXAFS Characterization of Nitrogen Doped Graphene

STM/S and Raman spectroscopy both provide indirect evidence of the presence of nitrogen dopants due to the lack of ability in element analysis.

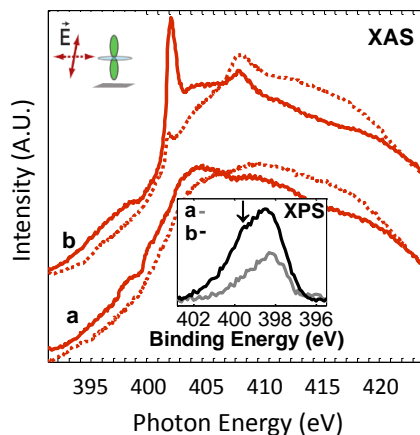


Fig. 3.24 NEXAFS (total electron yield) for pristine and NG10 sample on Cu foil at N K-edge. N-doping results in a new peak at 400.7 eV in the spectrum due to graphitic N dopants. (Inset) XPS for pristine and NG10 sample, showing a higher binding energy component in N-doped graphene (marked as the dark arrow).

Therefore, we confirmed the nitrogen incorporation into graphene lattice by performing x-ray photoemission spectroscopy (XPS) and near-edge x-ray absorption fine structure (NEXAFS) at the nitrogen K-edge for a pristine graphene and NG10 doped sample, results shown in Fig. 3.24. The addition of NH_3 in the graphene growth resulted in sharp peaks at 400.7 eV and 408 eV in the NEXAFS spectrum, corresponding to $1s\text{-to-}\pi^*$ and $-\sigma^*$ transitions respectively, for a single molecular species. The sharpness and strong polarization dependence of the peaks indicate that this species has well-defined, in-plane N-C bonds in the graphene lattice. Based on previous studies [68-70], the

peak can be assigned to sp^2 -bonded graphitic nitrogen with three nearest carbon neighbors. Representative N1s XPS shows a higher-binding energy components (black line) for the NH_3 -grown samples, indicating the formation of more electronegative N-C bonds in the graphene lattice as opposed to at edges or defects (gray line). This higher-binding energy peak is generally considered as a signature of graphitic nitrogen in studies of modified carbon films [17, 32, 70, 71].

3.6 References

1. Ashcroft, N.W. and N.D. Mermin, *Solid state physics*. 1976, New York,: Holt. xxi, 826 p.
2. Schroder, D.K., *Semiconductor material and device characterization*. 2006: John Wiley & Sons.
3. Turnbull, J., M. Stagg, and W. Eeles, *Annealing studies of boron-doped graphite by electron microscopy and X-ray diffraction*. Carbon, 1966. 3(4): p. 387-392.
4. Sidik, R.A., et al., *O₂ reduction on graphite and nitrogen-doped graphite: experiment and theory*. The Journal of Physical Chemistry B, 2006. 110(4): p. 1787-1793.
5. Kim, D.P., et al., *Electronic properties of nitrogen-doped graphite flakes*. Chemistry of Materials, 1991. 3(4): p. 686-692.
6. Maldonado, S., S. Morin, and K.J. Stevenson, *Structure, composition, and chemical reactivity of carbon nanotubes by selective nitrogen doping*. Carbon, 2006. 44(8): p. 1429-1437.
7. Hishiyama, Y., et al., *Structure, Raman scattering, and transport properties of boron-doped graphite*. Physical Review B, 2001. 63(24): p. 245406.
8. Han, W., et al., *Boron-doped carbon nanotubes prepared through a substitution reaction*. Chemical physics letters, 1999. 299(5): p. 368-373.
9. Redlich, P., et al., *B · C · N nanotubes and boron doping of carbon nanotubes*. Chemical physics letters, 1996. 260(3): p. 465-470.
10. Golberg, D., et al., *Single-walled B-doped carbon, B/N-doped carbon and BN nanotubes synthesized from single-walled carbon nanotubes through a substitution reaction*. Chemical Physics Letters, 1999. 308(3): p. 337-342.
11. Jang, J.W., et al., *Structural study of nitrogen-doping effects in bamboo-shaped multiwalled carbon nanotubes*. Applied physics letters, 2004. 84(15): p. 2877-2879.
12. Castro Neto, A.H., et al., *The electronic properties of graphene*. Reviews of Modern Physics, 2009. 81(1): p. 109-162.
13. Novoselov, K., et al., *Two-dimensional atomic crystals*. Proceedings of the National Academy of Sciences of the United States of America, 2005. 102(30): p. 10451-10453.
14. Wang, X.R., et al., *N-Doping of Graphene Through Electrothermal Reactions with Ammonia*. Science, 2009. 324(5928): p. 768-771.
15. Gierz, I., et al., *Atomic Hole Doping of Graphene*. Nano Letters, 2008. 8(12): p. 4603-4607.
16. Wei, D.C., et al., *Synthesis of N-Doped Graphene by Chemical Vapor Deposition and Its Electrical Properties*. Nano Letters, 2009. 9(5): p. 1752-1758.

17. Lin, Y.-C., C.-Y. Lin, and P.-W. Chiu, *Controllable graphene N-doping with ammonia plasma*. Applied Physics Letters, 2010. 96(13): p. 133110-3.
18. Panchokarla, L.S., et al., *Synthesis, Structure, and Properties of Boron- and Nitrogen-Doped Graphene*. Advanced Materials, 2009. 21(46): p. 4726-+.
19. Sun, Z.Z., et al., *Growth of graphene from solid carbon sources*. Nature, 2010. 468(7323): p. 549-552.
20. Deng, D., et al., *Toward N-Doped Graphene via Solvothermal Synthesis*. Chemistry of Materials, 2011. 23(5): p. 1188-1193.
21. Guo, B., et al., *Controllable N-Doping of Graphene*. Nano Letters, 2010. 10(12): p. 4975-4980.
22. Lv, R., et al., *Nitrogen-doped graphene: beyond single substitution and enhanced molecular sensing*. Scientific reports, 2012. 2.
23. Joucken, F., et al., *Localized state and charge transfer in nitrogen-doped graphene*. Physical Review B, 2012. 85(16): p. 161408.
24. Qu, L., et al., *Nitrogen-Doped Graphene as Efficient Metal-Free Electrocatalyst for Oxygen Reduction in Fuel Cells*. ACS Nano, 2010. 4(3): p. 1321-1326.
25. Luo, Z., et al., *Pyridinic N doped graphene: synthesis, electronic structure, and electrocatalytic property*. Journal of Materials Chemistry, 2011. 21(22): p. 8038-8044.
26. Wang, H., T. Maiyalagan, and X. Wang, *Review on Recent Progress in Nitrogen-Doped Graphene: Synthesis, Characterization, and Its Potential Applications*. ACS Catalysis, 2012. 2(5): p. 781-794.
27. Wang, Y., et al., *Nitrogen-Doped Graphene and Its Application in Electrochemical Biosensing*. ACS Nano, 2010. 4(4): p. 1790-1798.
28. Reddy, A.L.M., et al., *Synthesis Of Nitrogen-Doped Graphene Films For Lithium Battery Application*. ACS Nano, 2010. 4(11): p. 6337-6342.
29. Zhao, W., et al., *Production of Nitrogen-Doped Graphene by Low-Energy Nitrogen Implantation*. The Journal of Physical Chemistry C, 2012. 116(8): p. 5062-5066.
30. Shao, Y., et al., *Nitrogen-doped graphene and its electrochemical applications*. Journal of Materials Chemistry, 2010. 20(35): p. 7491-7496.
31. Imran Jafri, R., N. Rajalakshmi, and S. Ramaprabhu, *Nitrogen doped graphene nanoplatelets as catalyst support for oxygen reduction reaction in proton exchange membrane fuel cell*. Journal of Materials Chemistry, 2010. 20(34): p. 7114-7117.
32. Li, X., et al., *Simultaneous Nitrogen Doping and Reduction of Graphene Oxide*. Journal of the American Chemical Society, 2009. 131(43): p. 15939-15944.
33. Zhang, C., et al., *Synthesis of Nitrogen - Doped Graphene Using Embedded Carbon and Nitrogen Sources*. Advanced Materials, 2011. 23(8): p. 1020-1024.
34. Choucair, M., P. Thordarson, and J.A. Stride, *Gram-scale production of graphene based on solvothermal synthesis and sonication*. Nat Nano, 2009. 4(1): p. 30-33.
35. Li, X., et al., *Large-Area Synthesis of High-Quality and Uniform Graphene Films on Copper Foils*. Science, 2009. 324(5932): p. 1312-1314.
36. Meyer, J.C., et al., *Experimental analysis of charge redistribution due to chemical bonding by high-resolution transmission electron microscopy*. Nature Materials, 2011. 10(3): p. 209-215.
37. Ferrari, A.C., et al., *Raman spectrum of graphene and graphene layers*. Physical Review Letters, 2006. 97(18): p. 187401.
38. Ferrari, A.C., *Raman spectroscopy of graphene and graphite: Disorder, electron-phonon coupling, doping and nonadiabatic effects*. Solid State Communications, 2007. 143(1-2): p. 47-57.

39. Dresselhaus, M.S., et al., *Perspectives on Carbon Nanotubes and Graphene Raman Spectroscopy*. Nano Letters, 2010. 10(3): p. 751-758.
40. Dresselhaus, M.S., et al., *Defect characterization in graphene and carbon nanotubes using Raman spectroscopy*. Philosophical Transactions of the Royal Society a-Mathematical Physical and Engineering Sciences, 2010. 368(1932): p. 5355-5377.
41. Tuinstra, F. and J.L. Koenig, *Raman Spectrum of Graphite*. The Journal of Chemical Physics, 1970. 53(3): p. 1126-1130.
42. Yan, J., et al., *Electric Field Effect Tuning of Electron-Phonon Coupling in Graphene*. Physical Review Letters, 2007. 98(16): p. 166802.
43. DasA, et al., *Monitoring dopants by Raman scattering in an electrochemically top-gated graphene transistor*. Nat Nano, 2008. 3(4): p. 210-215.
44. Park, H.J., et al., *Growth and properties of chemically modified graphene*. physica status solidi (b), 2010. 247(11 - 12): p. 2915-2919.
45. Endo, M., et al., *Scanning tunneling microscope study of boron-doped highly oriented pyrolytic graphite*. Journal of Applied Physics, 2001. 90(11): p. 5670-5674.
46. Zheng, B., P. Hermet, and L. Henrard, *Scanning Tunneling Microscopy Simulations of Nitrogen- and Boron-Doped Graphene and Single-Walled Carbon Nanotubes*. Acs Nano, 2010. 4(7): p. 4165-4173.
47. Rutter, G.M., et al., *Scattering and interference in epitaxial graphene*. Science, 2007. 317(5835): p. 219-222.
48. Eric Cockayne, et al., *Rotational Grain Boundaries in Graphene*. arXiv:1008.3574v1, 2010.
49. Flynn, A.Z.-K.L.Z.L.P.M.S.H.D.R.R.A.N.P.G.W., *Segregation of Sublattice Domains in Nitrogen Doped Graphene*. In preparation.
50. Zhang, Y.B., et al., *Giant phonon-induced conductance in scanning tunnelling spectroscopy of gate-tunable graphene*. Nature Physics, 2008. 4(8): p. 627-630.
51. Decker, R., et al., *Local electronic properties of graphene on a BN substrate via scanning tunneling microscopy*. Nano letters, 2011. 11(6): p. 2291-2295.
52. Xue, J., et al., *Scanning tunnelling microscopy and spectroscopy of ultra-flat graphene on hexagonal boron nitride*. Nat Mater, 2011. 10(4): p. 282-285.
53. Deshpande, A., et al., *Spatially resolved spectroscopy of monolayer graphene on SiO₂*. Physical Review B, 2009. 79(20): p. 205411.
54. Yankowitz, M., et al., *Emergence of superlattice Dirac points in graphene on hexagonal boron nitride*. Nature Physics, 2012. 8(5): p. 382-386.
55. Lherbier, A., et al., *Charge transport in chemically doped 2D graphene*. Physical Review Letters, 2008. 101(3): p. 036808.
56. Giovannetti, G., et al., *Doping Graphene with Metal Contacts*. Physical Review Letters, 2008. 101(2): p. 026803.
57. Khomyakov, P.A., et al., *First-principles study of the interaction and charge transfer between graphene and metals*. Physical Review B, 2009. 79(19): p. 195425.
58. Kim, K.S., et al., *Large-scale pattern growth of graphene films for stretchable transparent electrodes*. Nature, 2009. 457(7230): p. 706-710.
59. Jindal, P.R.V.K., *Designing band gap of graphene by B and N dopant atoms*. arXiv, 2013. 1209(5228).

60. Wang, Y., et al., *Mapping Dirac quasiparticles near a single Coulomb impurity on graphene*. Nature Physics, 2012. 8(9): p. 653-657.
61. Bena, C., *Effect of a single localized impurity on the local density of states in monolayer and bilayer graphene*. Physical review letters, 2008. 100(7): p. 076601.
62. Chen, J.-H., et al., *Charged-impurity scattering in graphene*. Nature Physics, 2008. 4(5): p. 377-381.
63. Cheianov, V.V. and V.I. Fal'ko, *Friedel oscillations, impurity scattering, and temperature dependence of resistivity in graphene*. Physical review letters, 2006. 97(22): p. 226801.
64. Zhang, Y.B., et al., *Origin of spatial charge inhomogeneity in graphene (vol 5, pg 722, 2009)*. Nat. Phys., 2010. 6(1): p. 74-74.
65. Malard, L.M., et al., *Raman spectroscopy in graphene*. Physics Reports, 2009. 473(5-6): p. 51-87.
66. Yan, J., et al., *Electric field effect tuning of electron-phonon coupling in graphene*. Physical Review Letters, 2007. 98(16): p. 166802.
67. Das, A., et al., *Monitoring dopants by Raman scattering in an electrochemically top-gated graphene transistor*. Nature Nanotechnology, 2008. 3(4): p. 210-215.
68. Shimoyama, I., et al., *Evidence for the existence of nitrogen-substituted graphite structure by polarization dependence of near-edge x-ray-absorption fine structure*. Physical Review B, 2000. 62(10): p. R6053.
69. Hellgren, N., et al., *Nitrogen bonding structure in carbon nitride thin films studied by soft x-ray spectroscopy*. Applied Physics Letters, 2001. 79(26): p. 4348-4350.
70. Hellgren, N., et al., *Electronic structure of carbon nitride thin films studied by X-ray spectroscopy techniques*. Thin Solid Films, 2005. 471(1-2): p. 19-34.
71. Point, S., et al., *XPS and NEXAFS characterisation of plasma deposited vertically aligned N-doped MWCNT*. Diamond and Related Materials. 14(3-7): p. 891-895.

Chapter 4

Atomic and Electronic Structures of B-doped Graphene

4.1 Background of B-doped Carbon Lattices

Tailoring the electronic properties of monolayer graphene can unlock many potential electronic applications of graphene [1-3]. In pristine undoped graphene, the Fermi level coincides with the Dirac point, where the conductivity of the system is at its minimum [1]. By introducing free charge carriers, the conductivity increases linearly with the carrier density [4, 5]. Furthermore, tuning two regions of a single graphene sheet with electrons and holes respectively can produce p-n junctions [6, 7], the elementary building blocks of current electronic devices. Therefore, it is crucial to control the type and concentration of charge injected into graphene, especially in the absence of external fields.

In the last chapter (Chapter 3), we discussed the effects of nitrogen doping in monolayer graphene on its atomic and electronic structures, graphitic nitrogen dopants introducing $\sim 0.5e/N$ to the graphene lattice with only local electronic perturbations around dopant sites [8]. Boron, as the other neighbor of carbon in periodic table, is naturally selected to be the acceptor-dopant for introducing hole carriers into graphene. However, unlike nitrogen doped graphene, boron doped (B-doped) graphene has been much less explored experimentally [9-16] and basic questions about the dopant structure, dopant distribution and their effect on the electronic properties of graphene

films remain largely unanswered. Before going to our ways of seeking the answers to these questions, we will first take a look at what have been tried and obtained in the literature.

4.1.1 Literature of B-doped Carbon Allotropes

Even before the discovery of monolayer graphene, boron doping has been successfully used to modulate the electronic properties of other carbon materials, such as graphite [17-25], bucky balls [26, 27] and carbon nanotubes[28-31]. One of the most popular methods used to synthesize these B-doped carbon lattices is to cook the mixture of host carbon materials and elemental boron (or boron-containing powder, for instance, boron oxides) at elevated temperature of ~ 1400 - 1600°C for several hours [19, 20, 23, 25, 28-30]. In this procedure, the boron concentration can be tuned from less than 0.1% up to 3% depending on the reaction time [28]. Besides this method, ion implantation [22], arc discharge [27, 31] and chemical vapor deposition (CVD) [24] have also been employed to produce B-doped carbons.

Several experimental techniques have been used to characterize these B-doped carbon lattices, including x-ray diffraction (XRD) [23, 25], x-ray photoemission spectroscopy (XPS) [27], Raman spectroscopy [19, 23, 28], scanning tunneling microscopy (STM) [20], transmission electron microscopy (TEM) [29], and scanning electron microscopy (SEM) [25] as well. From a large scale, typically in a few tens of micrometers, SEM images show interstitial defect loops ($\sim 10\mu\text{m}$ in diameter) between layers in B-doped graphite [25]. When zooming into nanoscale, STM topographic images reveal single substitutional B dopants in B-doped graphite samples [20] while TEM images display signatures of defects induced by B incorporations in carbon nanotubes but without showing the defect structures in details [29]. From a more statistical point of view, Raman spectroscopy indicates the presence of defects by the appearance of D and D' defect modes [19, 23,

28], and XPS presents a rather broad B1s peak in the spectra of B-doped carbon lattices, indicative of multiple bonding configurations for the B dopants [27].

However, much less have been done in B doping monolayer graphene films so far. The chief reason seems to be the difficulty in synthesizing high-quality monolayer B-doped graphene, possibly because B-related gases/liquid are strongly reactive to water from ambient. Searching in the literature of B-doped graphene, a few attempts have been made in the direction of sample fabrication. The first one is to extract single layer B-doped graphene from pre-B-doped graphite via mechanical exfoliation [14]. Just as in the case of pristine graphene, the sample size is limited to, a few tens of micrometers at most, in this technique. Nevertheless, the quality of the sample has been testified by Raman spectroscopy and Raman mapping. The second way is to grow the doped films via CVD in which a B-containing precursor is introduced as the B source. *J. Gebhardt et al* synthesized B-doped graphene on Ni(111) substrate both in a CVD process with triethylborane as the source and by segregation of boron from bulk nickel [13], while *H. Wang et al* reported to grow monolayer B-doped graphene on Cu foil by the sole solid feedstock of phenylboronic acid ($C_6H_7BO_2$) [15]. Another alternative way to grow B-doped graphene layers is by arc discharge graphite in the presence of B-containing environment, for instance, B-doped graphite or in B_2H_6 vapor [16].

Similar as N-doped graphene and other B-doped carbon allotropes, several standard techniques, including XPS [15, 16], Raman spectroscopy [14, 16] and SEM [16], have been employed to investigate these B-doped graphene films. The presence of B dopants in carbon lattices is proven by the B1s peak at $\sim 190\text{eV}$ in XPS spectra, which can typically be decomposed into a few sub-peaks representing different bonding configurations [15, 16]. B dopants in graphene lattice act as defects, and thus D and D' bands show up in the Raman spectroscopy. It is worthwhile to point that D band

intensity is extremely enhanced due to the elastically scattered photo-excited electrons by B atoms before emitting a phonon [14]. A Raman spectrum for B-doped monolayer graphene with only $\sim 0.22\%$ B concentration is shown in Fig. 4.1a [14]. As a comparison, a Raman spectrum for N-doped graphene with similar N doping level is displayed in Fig. 4.1b, with a much shorter D band height. TEM and SEM images typically provide the large scale morphology of the B-doped graphene films. So far, no direct imaging on B dopant structures in monolayer graphene has been reported by any technique.

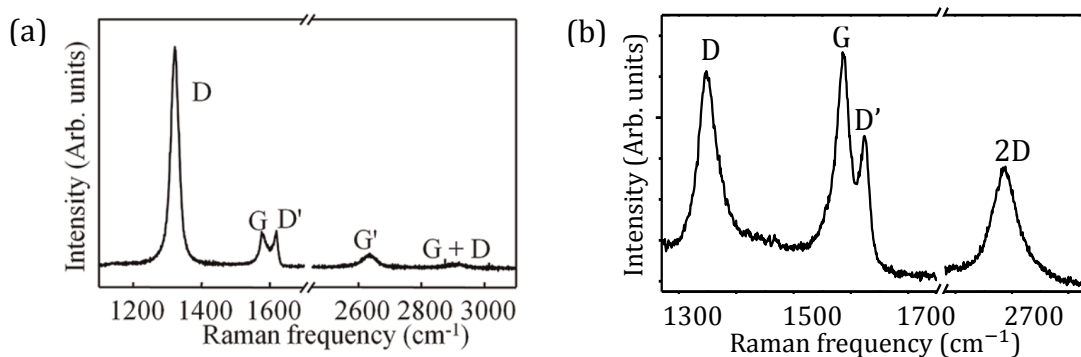


Fig. 4.1 Raman spectroscopy measurements on B-doped and N-doped graphene with dopant concentrations of $\sim 0.22\%$ and 0.3% respectively. (a) Raman spectrum taken from Ref. [14]; Note that G' peak is equivalent to 2D peak. (b) Raman spectrum taken on N-doped graphene films transferred on SiO₂/Si substrate. The significant difference in D peak intensities between B-doped and N-doped graphene indicate the different electron scattering rates induced by B and N dopants in graphene lattice.

4.1.2 Our Approaches for B-doped Graphene Preparations and Characterizations

The B-doped monolayer graphene films for our experiments were grown by the CVD method on polycrystalline copper foils using a mixture of CH_4 , H_2 and B_2H_6 gases at 1000°C in a quartz tube furnace [32, 33]. In the quest of understanding the B doping form, distribution and their effect on the electronic structures, we use STM/S in conjunction with x-ray absorption spectroscopy (XAS) to investigate the atomic and electronic structures of these B-doped monolayer graphene films. Moreover, we interpret our experimental results using first principle density function theory (DFT) calculations.

Our best-quality B-doped graphene films were produced by using quartz tubes that have been exposed to boron before growth, i.e. “tube-doped” manner. Specifically, in the process, the tube (with a piece of copper foil inserted) was first heated at 1000°C at 7.0 torr with a flow of 6 sccm of CH_4 and 1-5 sccm of B_2H_6 of 1% B_2H_6 in H_2 for 30 mins. Afterwards, a new piece of Cu foil was introduced into the tube and B-doped graphene growth was then performed using only 6 sccm of CH_4 and 100 sccm of H_2 . It is found that the prior exposure of the tube to boron is sufficient to dope the graphene in subsequent growths.

What we think it happens during this growth procedure is as follows. Due to its relatively high vapor pressure at 1000°C , some Cu is deposited onto the side walls of the quartz tube. Additionally, as the reaction temperature is effectively at the eutectic point of the B-Cu system [34], a significant amount (in terms of relative atomic %) of B is introduced into both the Cu foil and the Cu on the tube sidewalls. Subsequent growths are then exposed to B from the evolution of this sidewall alloy as opposed to direct flow of B_2H_6 . Given the nature of this process, it is difficult to provide a precise concentration for these “tube-doped” graphene growths. However, empirically we have found that the most successful B-doped graphene growth are performed directly after the

initial tube exposure, while successive syntheses are not as effective. A cartoon diagram for the growth set is shown in Fig. 4.2 with parts specific for B-doped graphene highlighted with bright colors.

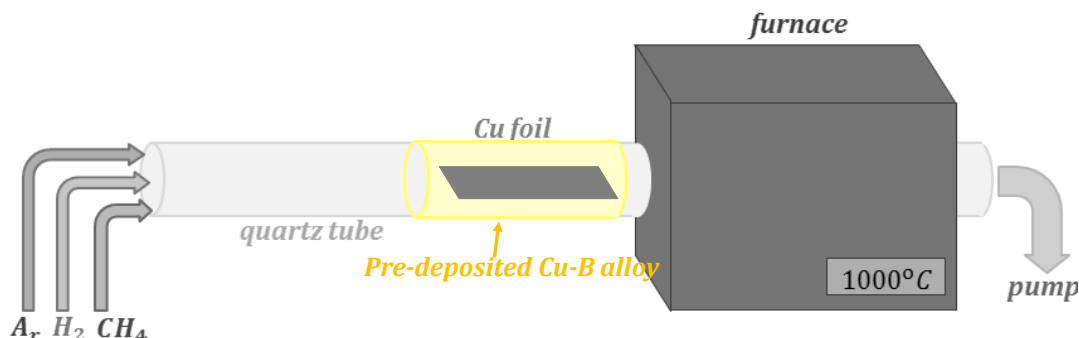


Fig. 4.2 Cartoon diagram of a CVD growth setup for B-doped (“tube-doped”) graphene growth. The yellow colored part highlight the one specifically for B-doped graphene growth, while the gray colored parts are the parts shared with pristine/N-doped graphene growth.

■ *B-doped graphene films/Cu foil are provided by Mark Levendorf in Park group @ Cornell U.*

Following the growths, as-grown B-doped graphene films on Cu foil were transferred for STM/S measurements from ambient conditions into an ultra-high-vacuum (UHV) chamber, and annealed at $\sim 350^\circ\text{C}$ for ~ 5 hours to clean the surface. STM/S measurements were taken at 77K.

4.2 Similarities with N-doped Graphene

Since boron and nitrogen are symmetric about carbon in the periodic table, they are expected to share some similarities in chemically doping graphene films. In the following of this section, we will discuss these similarities found in atomic structures and electronic properties. Here, we limit our discussions in 4.2.1 and 4.2.2 to the “tube-doped” samples since they have the best-quality among all the growth conditions.

4.2.1 Boron Doping Forms

A representative large scale topography is shown in Fig. 4.3. The appearance of bright features is associated with the Boron doping process since they are absent in the pristine graphene case. A careful examination through these features reveals that the majority of them (one of them marked by a red arrow) look identical while a few highlighted ones (marked by orange arrows) are much more complicate and extend further in space. We will first focus on the major ones and then move to the minor ones (details in Section 4.3.1).

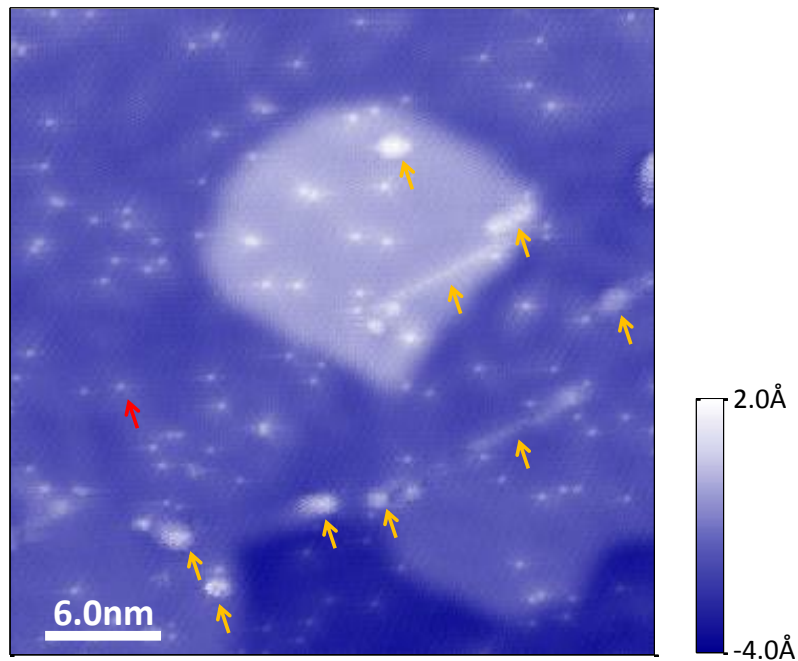


Fig. 4.3 A STM topographic image taken on an $30 \times 30 \text{ nm}^2$ area on “tube-doped” (B-doped) graphene films on Cu foil. The red arrow marks the one of the majority “bright” structures while the orange arrows highlight the complicate defect structures. Scanning conditions: $V_{bias} = -0.5 \text{ V}$ and $I_{set} = 0.5 \text{ nA}$

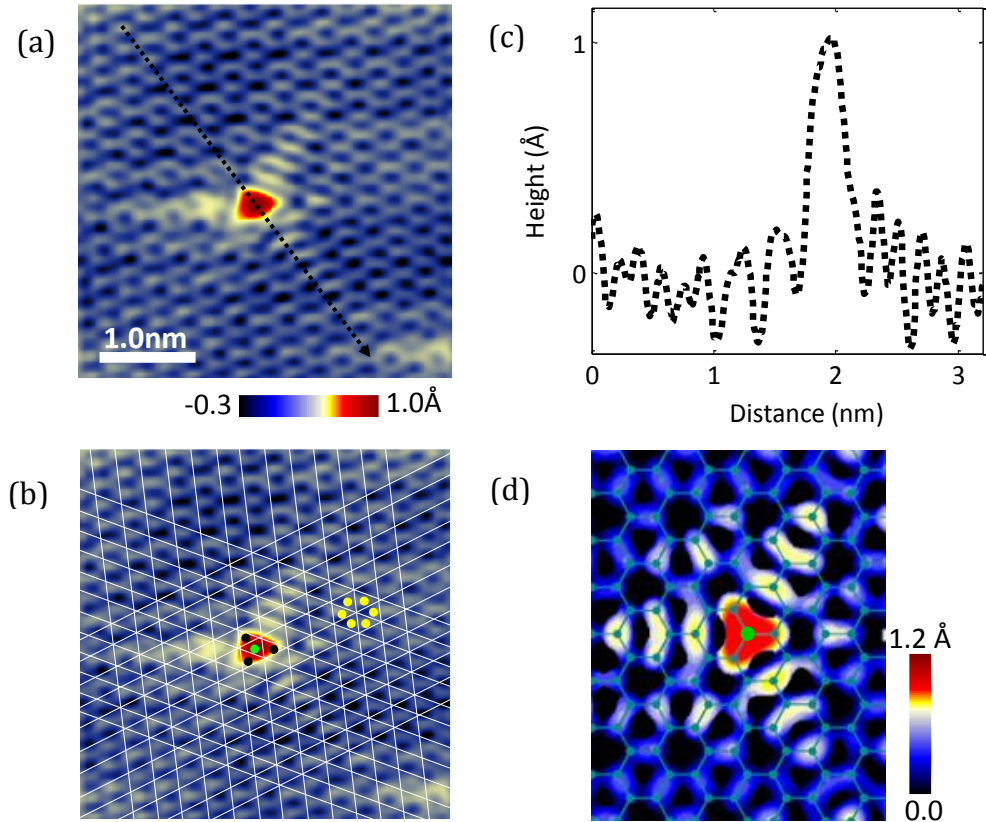


Fig. 4.4 Individual graphitic Boron dopant. (a) A STM topographic image taken on a single graphitic Boron dopants on “tube-doped” graphene on Cu foil. (b) Image in (a) overlaid with a lattice mesh, with the green dot indicating the center of the triangle at a Carbon site, the three dark spots at the apexes of the triangle sitting on the first three nearest neighboring Carbon sites and the six yellow spots highlighting the Carbon sites in a perfect honeycomb ring. (c) A line profile taken across the Boron dopant site, as indicated by the dark dashed line in (a). (d) DFT calculations simulated STM topography for a single graphitic dopant with bias voltage of -0.5eV . Scanning conditions for (a): $V_{bias} = -0.5\text{V}$ and $I_{set} = 0.5\text{nA}$

A close-up look at the common feature exhibits a triangular shaped core with three “tails” extending from the three edges of the triangle, as shown in Fig. 4.4a. This structure exhibits all the features expected from a graphitic dopants: by following the unperturbed honeycomb lattice from

the position far away from the dopant sites, as indicated in Fig. 4.4 b by the overlaid mesh on top of image in Fig. 4.4a, we can determine that the center of the triangle is at a carbon site (C_B) (green spot in Fig. 4.4b) and the three apexes are at the three nearest neighboring carbon sites (C_{1B}) (three dark spots in Fig. 4.4b). The line profile across this feature (Fig. 4.4c) shows an apparent height of $1.0 \pm 0.2 \text{ \AA}$ at the dopant site. Furthermore, DFT calculations [35, 36] simulating a single graphitic B dopant structure in free-standing graphene (shown in Fig. 4.4d) closely match the experimentally observed shape and the apparent height ($\sim 1.0 \text{ \AA}$ in theory calculations).

A survey over multiple areas in multiple samples shows that such substitutional B dopants take up $\sim 80\%$ of the “bright” features over the sample surfaces. The concentration of B dopants varies from sample to sample, ranging from $2.5 \times 10^{12} \text{ cm}^{-2}$ to $1.3 \times 10^{13} \text{ cm}^{-2}$, which results from the un-controllable doping level in the “tube-doped” growth process.

4.2.2 Electronic Structures

A chief reason to create B-doped graphene is to introduce hole carriers into the graphene sheet, in analogy with the case of electron doping for N-doped graphene [8]. So far, we have confirmed, over 80% of the features in B-doped graphene films are individual graphitic B dopants, which makes it possible to test the charge carrier injection efficiency.

In order to measure the charge carrier type and density contributed by the graphitic B dopants, we performed detailed STS measurements on multiple B-doped graphene samples. Fig. 4.5a shows a spatially averaged differential conductance (dI/dV) spectrum (dark curve) with variations (gray band) taken over an area of $30 \times 30 \text{ nm}^2$ on B-doped graphene films on Cu foil with spatial resolution of $\sim 0.5 \text{ nm}$. Similar as in the case of N-doped graphene [8], two depressions are

seen in the spectrum. One of them is at the Fermi level E_F (i.e. at zero bias voltage marked with the red arrow in Fig. 4.5a), which is associated with the phonon-assisted inelastic tunneling process [37]. The other one locates at $\sim 150\text{meV}$ above E_F , which is assigned to be Dirac point (E_D) where density of states (DOS) of graphene stays low. The fact that Fermi level is below Dirac point (i.e. $E_F < E_D$) indicates that the graphene film is indeed hole doped. The statistical histogram of Dirac points extracted from all the dI/dV spectra (about 3600 spectra) in Fig. 4.5a is displayed in Fig. 4.5b, with a mean value of $E_D = 110\text{meV}$ and full width half maximum (FWHM) of $\Delta E_D = 30\text{meV}$. Using the relation of

$$n_h = \frac{E_D^2}{\pi(\hbar v_F)^2}, \quad (4.1)$$

where $v_F \approx 10^6\text{m/s}$ [1, 4, 5], we estimated a hole carrier concentration of $n_h = (9.0 \pm 4.6) \times 10^{11}\text{cm}^{-2}$ in this area.

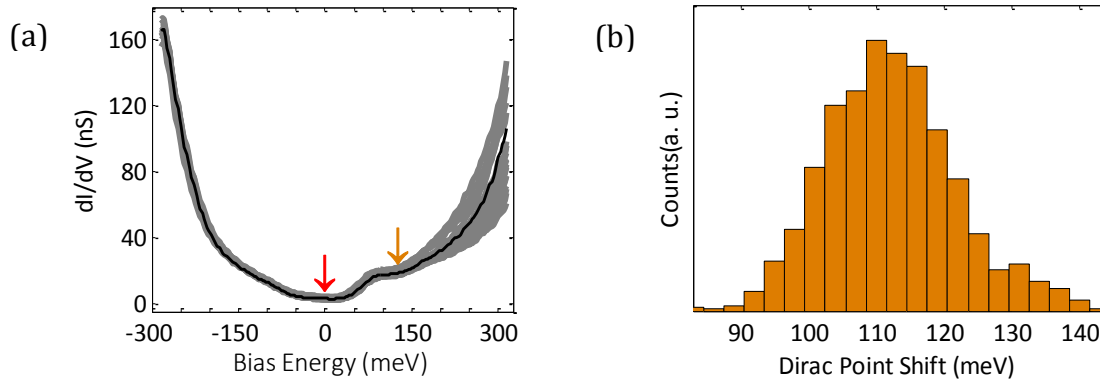


Fig. 4.5. Dirac point shifts in STS on “tube-doped” graphene on Cu foil. (a) Spatially averaged dI/dV spectra (black line) and variations (gray band) over an area of $30 \times 30\text{nm}^2$. Red arrow indicates the gap induced by insufficient energy for phonon-assisted inelastic tunneling process while the orange arrow points the apparent Dirac point position. (b) Histogram of the spatial variation of Dirac points for B-doped graphene in this $30 \times 30\text{nm}^2$ area. Scanning conditions for (a): $V_{bias} = -0.5\text{V}$ and $I_{set} = 0.3\text{nA}$.

By counting the number of B dopants at the same area as the dI/dV measurements, we have a B dopant concentration of $n_B = 2.27 \times 10^{12} \text{cm}^{-2}$. The ratio of n_h/n_B gives us the average number of hole carriers contributed by per B dopant, which is equal to $n_h = (0.40 \pm 0.20)h/B$ in this area. Detailed STM and STS measurements over multiple B-doped graphene samples with varying B doping levels (Fig. 4.6a) show similar doping rates of $\sim 0.5h/B$. Our experiment thus indicates that the magnitude of the electronic doping rate caused by graphitic B dopants is very similar to that of graphitic N dopants in graphene films. Our DFT calculations (Fig. 4.6b) confirm that graphitic B dopants induce a deficiency of charge in graphene sheet at an average withdrawing rate of $\sim 0.5h/B$ [38], consistent with our experimental results.

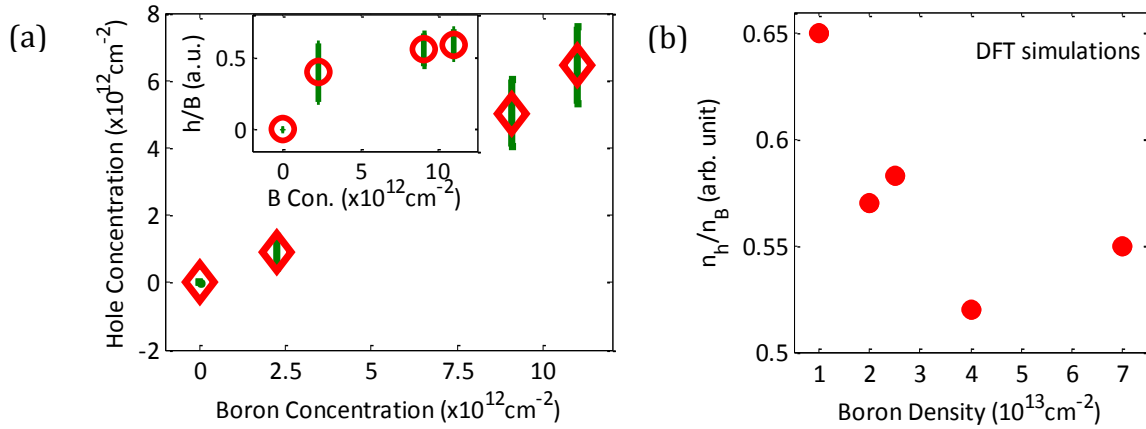


Fig. 4.6 Averaged carrier (hole) concentration as a function of B dopant density. (a) Spatially averaged hole carrier concentration as a function of averaged Boron doping level over four different samples. (Inset) Hole carrier per Boron dopant as each of the four samples, showing a hole carrier doping rate of $\sim 0.5h/\text{graphitic B}$. (b) DFT calculations of hole carrier concentration per Boron dopant calculated for five Boron doping levels by varying the supercell in the calculations.

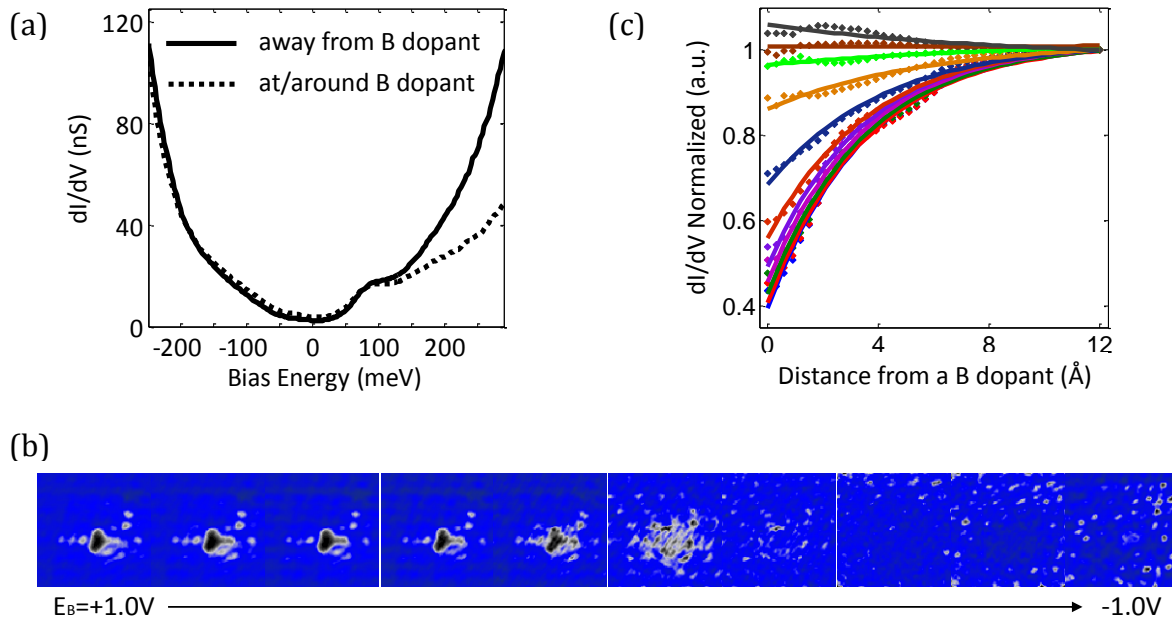


Fig. 4.7 Spectroscopic mapping around a single graphitic B dopant. (a) dI/dV spectra taken on/near the B dopant (dashed line) and far away from the B dopant (solid line) for B-doped graphene on Cu foil. Scanning conditions: $V_{bias} = -0.5V$ and $I_{set} = 0.3nA$; (b) A set of STM spectroscopic maps taken over an $2.5 \times 2.5nm^2$ area in the vicinity of a single graphitic B dopant for B-doped graphene films on Cu foil at different bias energies from $-1.0V$ to $+1.0V$. Scanning conditions: $V_{bias} = -0.8V$ and $I_{set} = 0.5nA$; (c) Radially averaged dI/dV (differential conductance) as a function of the distance from the B atom at different bias energies from $-1.0V$ to $+1.0V$, normalized to unity at distances far away from the B dopant site. The fits are to an exponential decay function.

Furthermore, we investigated the perturbations in electronic structures induced by the presence of B dopants. Same as in the case of N-doped graphene, B dopants break A-B sublattice symmetry locally around dopant sites, by showing stronger intensity on one sublattice than on the other one in the topographic images. We performed further dI/dV spectra and maps over a single dopant to focus on the electronic variations over space. Fig. 4.7a shows two dI/dV spectra taken on/around and far away from the B dopant. An enhancement in electron-hole asymmetry is clearly

observable in the spectrum taken around B dopants, due to the fact that B dopants attract positive charge carriers and repel negative charge carriers. A set of dI/dV maps taken around a B dopant at various bias energies from -1.0V to +1.0V, in Fig. 4.7b, shows intensity contrast between dopant neighborhood and background in local density of states (LDOS) at positive biases but not in negative biases, in accord with dI/dV spectra in Fig. 4.7a. The radially averaged dI/dV intensity as a function of distance from B dopant site is plotted in Fig. 4.7c for all ten energy levels measured in Fig. 4.7b, with the background dI/dV intensity normalized to unity. All of the spectra are well fit by exponential functions with similar decay lengths of $\sim 6\text{\AA}$ but different ratios of dI/dV intensity at dopant site to that of background. This indicates that the perturbation in LDOS in vicinity of B dopants is localized around dopant sites, just the same as N-doped case [8].

4.3 Differences to N-doped Graphene

Despite the similarities between graphitic B and N in graphene lattice, subtle differences between them have been reported in the literature. For instance, B-C bond is about 0.5% longer than C-C bond while N-C bond has about the same length as C-C bond [16]; elemental B interacts much stronger with Cu than N does [34]. How will these differences affect the properties of B- (N-) doped graphene films?

4.3.1 STM Topographic Features

As discussed in last section, the overall triangular symmetry of the graphitic B is very similar to the case of graphitic N dopants in graphene lattice. However, important differences exist in the details of the structure. This is best visualized in the angular averaged topographic line profile through graphitic B and N dopants, as displayed in Fig. 4.8a. While the topographic features for both kinds of

dopants extend to a radius of about 1.0nm, the topographic maximum occurs at different locations in the two cases. In the case of the B dopant, the maximum height is observed at the B dopant site (green diamond, inset Fig. 4.8a). However, in the case of N dopant, the maximum is seen close to the nearest neighboring carbon sites to the N dopant (green circle, inset Fig. 4.8a). This difference is further confirmed by high-resolution atomic images of graphitic B and N dopants, shown in Fig. 4.8 b and c.

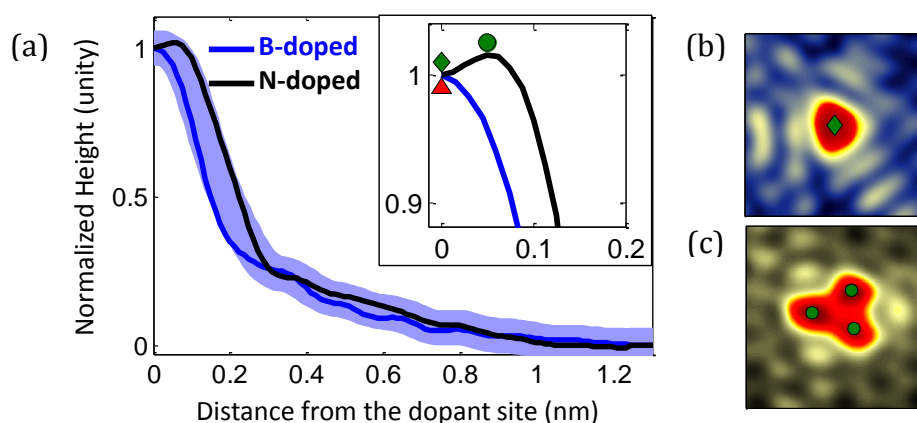


Fig. 4.8 STM topographic difference between graphitic B and N dopants. (a) Angular averaged line profile for graphitic B dopant (blue line) and N dopant (black line). The light blue band indicates the length scale over which the Boron and Nitrogen dopants perturb the local density of states of graphene. (Inset) Zoom-in of line profile shown in (a), with green diamond for the highest point in B dopant and green circle for the highest spot in N dopant. (b) and (c) High atomic resolution STM topographic images of single B ($V_{bias} = -0.5V$ and $I_{set} = 0.5nA$) and N ($V_{bias} = 0.5V$ and $I_{set} = 0.5nA$) dopants, with green markers highlighting the highest spots in the topography.

In a STM topographic image, an apparent height increase at a given atomic site can arise either from a real structural height increase, or from electronic effects if the tunneling amplitude is enhanced over the atom. In order to distinguish between these two possibilities, we performed DFT calculations of the bonding environment, charge density distribution and local density of states for

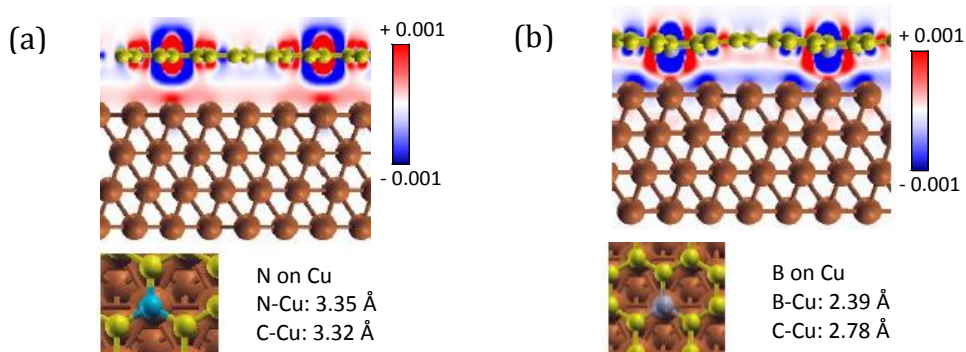


Fig. 4.9 DFT calculations of structures and charge density differences for graphitic N and B dopants on a commensurate Cu slab. (a) Structure and charge density differences in N-doped graphene commensurate with Cu(111), with the N dopant on top of a Cu atom. Red denotes excess of charge and blue for a deficit of charge. (b) Structure and charge density differences in B-doped graphene with B atom on top of a Cu atom.

■ Theory work was done by Lucia Pálová in Reichman's group at Columbia U.

graphitic B and N doped graphene on top of a commensurate slab of Cu(111) single crystal, as shown in Fig. 4.9a and Fig. 4.9b respectively. Our DFT calculations show that there is a substantial difference in the interactions between the Cu substrate and the B and N dopant. The N dopants are seen to not interact significantly with Cu substrate. They remain coplanar with the surrounding graphene, with the N-C nearest neighbor distance of 1.40Å, which is very close to the C-C nearest neighbor distance of 1.41Å in our calculations. Similarly, the vertical distances of N and C from the Cu plane are almost identical at 3.35Å and 3.32Å respectively. On the other hand, empty p_z states of B localized in the region around the dopant site drive strong interactions with Cu d_z^2 and s states. This interaction pulls B closer to the Cu substrate and drives a deformation of the initially flat graphene [20]. In particular, the vertical distances of B and C from the Cu plane are 2.39Å and 2.78Å respectively. The interaction is observed also from a more apparent charge modulation on top of

the Cu surface. This difference between N and B interaction with Cu is found independent of the registry to the Cu(111) surface. Our DFT calculations therefore indicate that the apparent height difference between B and N dopants in the STM topographic images is a purely electronic effect that arises from the fact that the p_z orbital of the B dopant extends further than that of the N dopant [36].

Apart from these individual graphitic B dopants, there are a good number of additional topological defects ($\sim 20\%$) in the graphene films. Fig. 4.10a shows a $30 \times 30 \text{ nm}^2$ scan displaying some of these defects (marked by white arrows), a few graphitic B dopants (marked by red/green triangles) as well as hexagonal Moiré pattern associated with mismatch between graphene lattice and the underlying Cu lattice [39]. Closer-up images of these defect structures shown in Fig. 4.10b reveal a variety of the defect forms. These include four pentagon-heptagon pairs surrounding a hexagon (inset 1, Fig. 4.10b) [40], a grain boundary loop composed of six pentagon-heptagon rings (inset 2, Fig. 4.10b) [41], and more complicated combinations of pentagon-heptagon defects (inset 3-6, Fig. 4.10b). The basic defect structure is the Stone-Wales (SW) defects that has been observed in graphene prepared by CVD growth on Nickel substrates [42, 43] and by epitaxial growth on SiC substrate [40, 44]. The SW defect is the topological defect with the lowest energy of formation per dislocation [40]. In both pristine graphene and N-doped graphene grown by CVD on Cu foil, we do not observe isolated or grouped SW defect structure. The $\sim 20\%$ concentration of SW defect structures in B-doped graphene is thus related to the introduction of B atoms during the CVD growth. Previous experiments on graphite have shown that the introduction of B atoms into graphite causes interstitial defect loops [25], and increases roughness in the graphitic basal plane [20, 45]. The similarities of our observation with these previous reports suggest that similar mechanisms are at work in our samples.

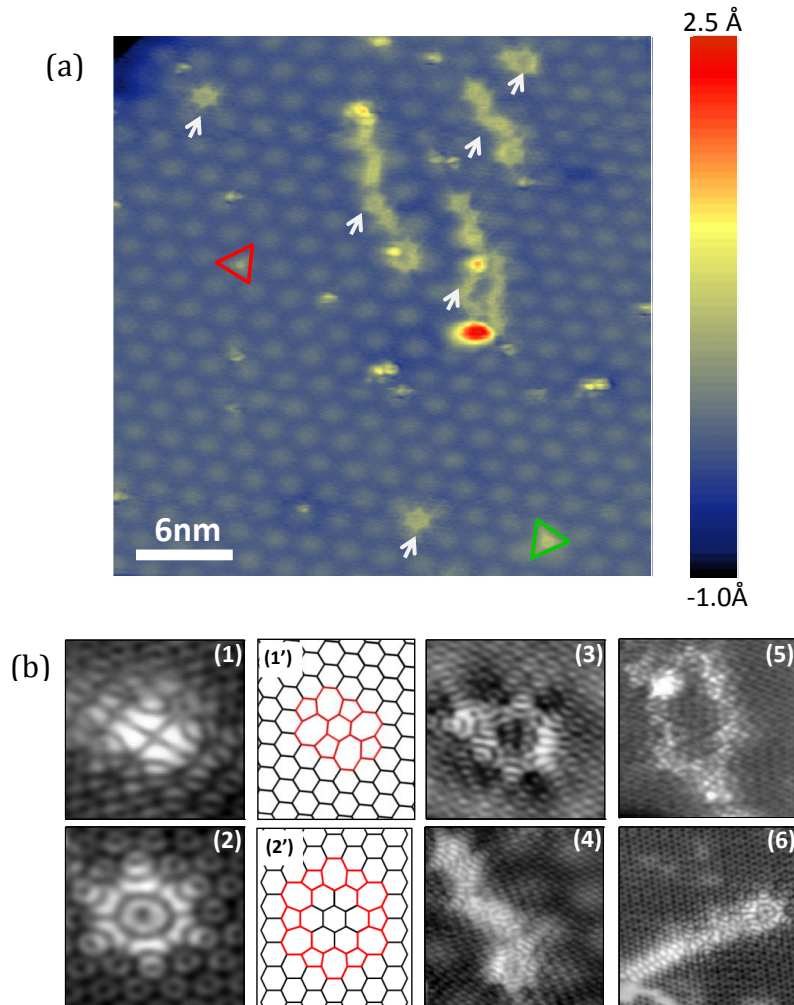


Fig. 4.10 Stone-Wales defect structures observed on “tube-doped” graphene films on Cu foils. (a) STM image of an $30 \times 30 \text{ nm}^2$ area exhibiting multiple defect forms. Red and green triangles indicate the graphitic B dopants in both sublattices. White arrows indicate the complicate defect forms composed by SW defect pairs. (b) STM images of different defect forms associated with pentagon-heptagon pairs. Inset (1') and (2'), proposed atomic structures for features in inset (1) and (2) respectively. Scanning conditions: $V_{bias} = -0.5 \text{ eV}$ and $I_{set} = 0.5 \text{ nA}$.

Topographic defects and grain boundaries are known to produce resonant states near the Dirac point in graphene [46-48]. Their effect on adding or withdrawing charge from the graphene sheet is less known. STS measurements of differential conductance (dI/dV) spectrum in Fig. 4.11a

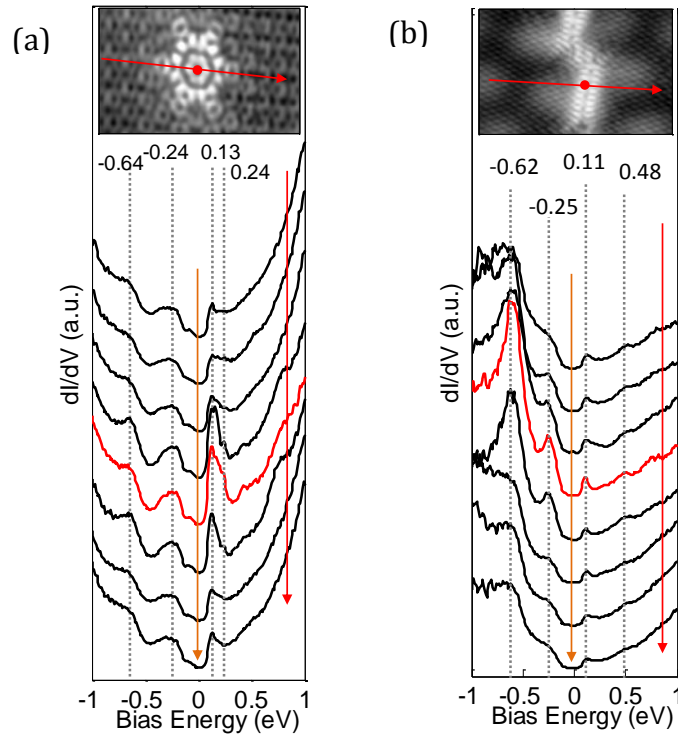


Fig. 4.11 Resonances in local density of states of graphene in the presence of SW defects. (a) dI/dV spectra taken across the “flower” feature in inset (2) of Fig. 4.10b with the red spectrum taken at the center of the feature. (b) dI/dV spectra taken across the “zipper” feature in inset (6) of Fig. 4.10b, with red spectrum taken at the center of the feature. Scanning conditions: $V_{bias} = -0.5\text{eV}$ and $I_{set} = 0.3\text{nA}$.

and Fig. 4.11b were taken across the features of a “flower” structure (Fig 4.10b inset 2) and a “zipper” structure (Fig. 4.10b inset 6) respectively. The Dirac point E_D is seen to be close to E_F for both cases, as indicated by the orange arrows. In this area, we also observe almost no graphitic dopants. This together with zero Dirac point shift in this area indicates that the SW defect structures do not contribute free charge carriers into graphene films. However, the defects do introduce resonances in the local DOS at bias voltages of $\sim -0.6\text{eV}$, $\sim -0.25\text{eV}$, $\sim 0.1\text{eV}$ and $\sim 0.25\text{eV}$ ($\sim 0.5\text{eV}$) as shown in the dI/dV spectra in Fig. 4.11a (b). The resonance energy varies with the geometry of the arrangement of SW defects, varying from $\sim 0.25\text{eV}$ for the “flower” structure to

$\sim 0.5\text{eV}$ for the “zipper” structure. The width of the regions for the resonance is approximately $\sim 5\text{nm}$, with the maximum intensity observed at the defect sites. The effect of such defects on transport properties depends on the details of the structure, and both weak and strong scattering is predicted from different defect configurations [49, 50].

4.3.2 Dopant Distributions between Sublattices

In discussions of the dopant distribution for both B-doped and N-doped graphene, we limit to the graphitic dopants since they are the major ones in both doped samples.

As revealed in the last section, the atomic scale interactions between B and Cu substrate are much stronger than that between N and Cu. Interestingly, such atomic-scale differences have a profound impact on the dopant distribution at larger length scales (\sim a few tens of nm). In general, graphitic substitution can occur in both graphene sublattices as shown in Fig. 4.12a. In each case, the nearest neighbors of the dopant atom come from the opposing sublattice, resulting in dopant features that have triangular symmetry rotated 180° from one another (as highlighted by the red and green triangles in Fig. 4.12a). STM topographic measurements indicate that the graphitic dopants distribution between two sublattices is very different in B and N-doped graphene films. Fig. 4.12b and Fig. 4.12c show typical $10 \times 10\text{nm}^2$ areas of B-doped and N-doped graphene surface respectively. In these two images, the dopants exist in both sublattices and their effects on the image morphology are highlighted by red and green triangles. In the case of B-doped graphene, the dopants are distributed randomly between the two sublattices, while N-doped graphene shows a strong tendency for the dopants to cluster locally on the same sublattice (as briefly mentioned in Chapter 3 for the N-doped case). This phenomenon is further confirmed in multiple samples and across large areas, as shown in Fig. 4.13a and Fig. 4.13b [8].

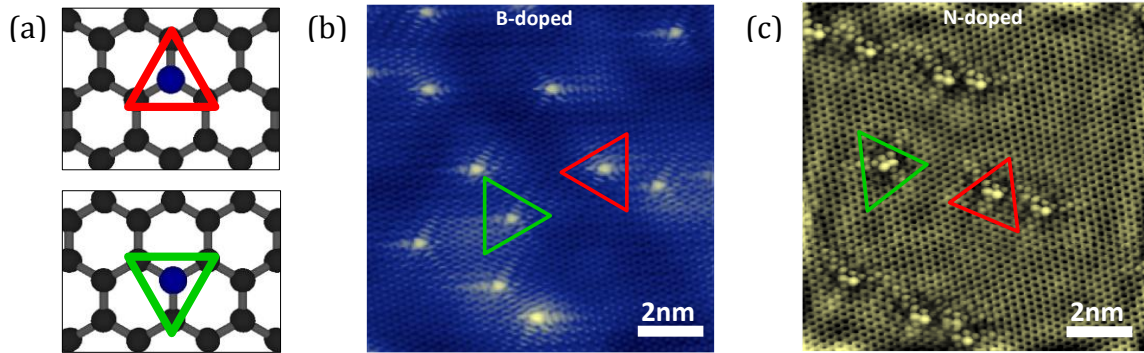


Fig. 4.11 Dopant distribution between A-B sublattices of graphene. (a) Cartoon diagrams for dopants in both sublattices and the orientations of the triangle pattern formed by the first three carbon atoms for the dopant sites. Red and green triangles highlight examples of dopants in both sublattices. (b) STM topography of an $12.5 \times 12.5 \text{ nm}^2$ area on B-doped graphene on Cu foil. Scanning conditions: $V_{bias} = -0.5 \text{ eV}$ and $I_{set} = 0.5 \text{ nA}$. (c) STM topography ($12.5 \times 12.5 \text{ nm}^2$) on N-doped graphene film on Cu foils. Scanning conditions: $V_{bias} = 0.5 \text{ eV}$ and $I_{set} = 0.5 \text{ nA}$.

To quantitatively characterize the spatial distribution of the dopants both within and between the two sublattices, we analyze statistically the positions of the dopants from large area STM images ($30 \times 30 \text{ nm}^2$ in Fig. 4.13a and Fig. 4.13b). We do this by calculating the probability that a given STM image is consistent with a random dopant distribution using two test methods. In the first test, we simply consider the ratio of the total number of dopants observed in each sublattice for a given image, and calculate the likelihood that a random distribution between sublattices of dopants will result with this ratio. This test can detect the sublattice segregation when the size of the STM image is smaller or comparable to the typical domain size of dopants being in one sublattice. For domains smaller than the typical STM image, we use the Moran Index [51] as a test of sublattice segregation. Both these tests produce p-values [52] which indicate the probability that a given STM image arises from a random dopant distribution between sublattices. A p-value greater than 0.05 indicates that the dopant distribution is within two standard deviation of the most

probable random distribution between two sublattices [52]. In the following, we will give a brief description of *ratio test*, *Moran Index test* and *p-value*.

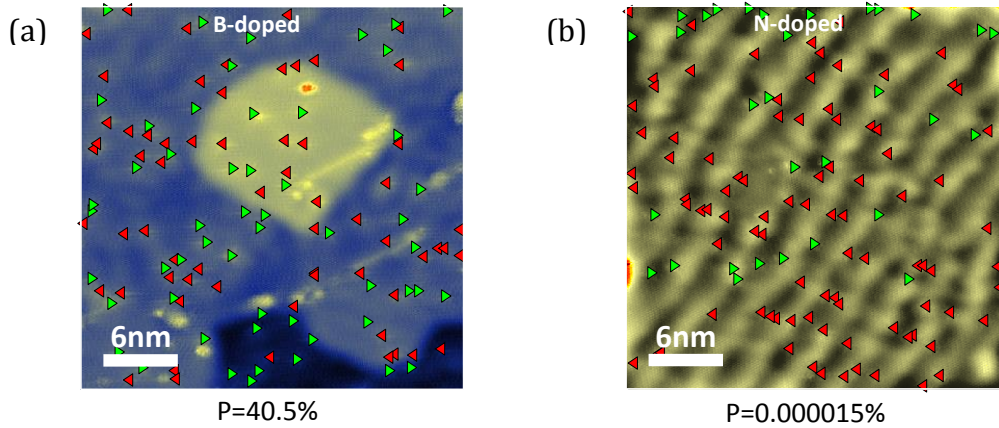


Fig. 4.13 Dopant distribution between A-B sublattices of graphene at larger scale of 30nm by 30nm. (a) STM topography of an $30 \times 30\text{nm}^2$ area on B-doped graphene on Cu foil, with red and green triangles marking the dopants in two sublattices. The ratio and Moran Index tests result in a probability of 40.5% for B dopants in this area randomly distributed between two sublattices. Scanning conditions: $V_{bias} = -0.5\text{eV}$ and $I_{set} = 0.5\text{nA}$. (b) STM topography ($12.5 \times 12.5\text{nm}^2$) on N-doped graphene film on Cu foils. The tests give a probability of $\sim 0.000015\%$ for random distribution of N dopants between two sublattices, indicating a sublattice cluster effect. Scanning conditions: $V_{bias} = 0.5\text{eV}$ and $I_{set} = 0.5\text{nA}$.

Ratio test – the ratio of the number N_r of dopants in one sublattice out of a total of N dopants is defined as

$$p = \frac{N_r}{N}. \quad (4.2)$$

Under the hypothesis of a dopant occurring in both sublattices with equal probability, the ratio p follows a normal distribution with mean of

$$E(p) = 0.5, \quad (4.3)$$

and standard deviation of

$$\sigma(p) = \sqrt{\frac{E(p) \times (1 - E(p))}{N}} \quad (4.4)$$

Moran Index test – in statistics, Moran Index is used to measure spatial autocorrelation, which is defined as

$$I = \frac{N}{\sum_i \sum_j w_{ij}} \frac{\sum_i \sum_j w_{ij} (X_i - \bar{X})(X_j - \bar{X})}{\sum_i (X_i - \bar{X})^2}. \quad (4.5)$$

In this formula, N is the number of spatial features which are indexed by i and j ; $X_i (i = 1 \sim N)$ are the variables of interest for the i^{th} feature; \bar{X} is the average of the variables; and w_{ij} is the spatial weight between the i^{th} and j^{th} features which is usually defined as the inverse of the distance between the two features.

The expected value of Moran Index under the null hypothesis of no spatial autocorrelation is defined as

$$E(I) = \frac{-1}{N-1}. \quad (4.6)$$

And its variance is

$$\sigma(I) = \frac{NS_4 - S_3S_5}{(N-1)(N-2)(N-3)(\sum_i \sum_j w_{ij})^2}, \quad (4.7)$$

where

$$S_1 = \frac{1}{2} \sum_i \sum_j (w_{ij} + w_{ji})^2; \quad (4.8)$$

$$S_2 = \sum_i \left(\sum_j w_{ij} + \sum_j w_{ji} \right)^2 ; \quad (4.9)$$

$$S_3 = \frac{\sum_i (X_i - \bar{X})^4 / N}{\left(\sum_i (X_i - \bar{X})^2 / N \right)^2} ; \quad (4.10)$$

$$S_4 = (N^2 - 3N + 3)S_1 - NS_2 + 3 \left(\sum_i \sum_j w_{ij} \right)^2 ; \quad (4.11)$$

$$S_5 = S_1 - 2NS_1 + 6 \left(\sum_i \sum_j w_{ij} \right)^2 . \quad (4.12)$$

p-value – as described above, both the ratio test and Moran Index test of a given set of experimental data follow a normal distribution with a mean value of $E(p)$ ($E(I)$) and a standard deviation of $\sigma(p)$ ($\sigma(I)$), under the null hypothesis of dopants distributing randomly between the two sublattices of honeycomb lattice. Therefore, $\frac{p-E(p)}{\sigma(p)}$ follows a standard normal distribution, which is

$$\frac{p - E(p)}{\sigma(p)} \sim N(0,1). \quad (4.13)$$

Here, $N(0,1)$ stands for a standard normal distribution, $N(0,1) = \frac{1}{\sqrt{2\pi}} e^{-x^2/2}$. To measure the consistency between experimental observations and the null hypothesis, the p-value is introduced as

$$P \left(|Z| > \frac{p_0 - E(p)}{\sigma(p)} \right), \quad (4.14)$$

where $Z = \frac{p-E(p)}{\sigma(p)} \sim N(0,1)$.

As an example of the application of these tests, we consider Fig. 4.13a and b for B-doped and N-doped cases respectively. In B-doped graphene such as in Fig. 4.13a, the p-value obtained from the ratio test is 0.405 and from the Moran Index test is 0.503. In contrast, the N-doped graphene (Fig. 4.13b) results in p-values of 1.5×10^{-7} from the ratio test and 3.1×10^{-6} from the Moran Index test. The test thus provide additional confirmation for what appears to be evident to the eye from the two figures – B-doped graphene does not show sublattice segregation down to the smallest length scales, whereas N-doped graphene does indeed segregate, with domain size at least larger than 30nm. We investigated multiple B and N-doped graphene samples, and took the smaller p-value of the two tests to represent the degree of randomness. These values are plotted in Fig. 4.14, where the p-values for B dopants for all the images obtained are above 0.1, while those for N dopants are all below 10^{-6} .

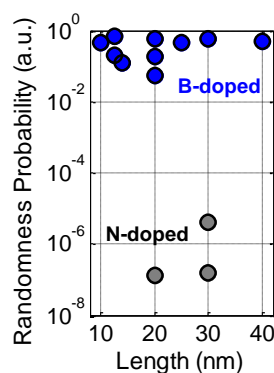


Fig. 4.14 Statistics of dopant distribution between two sublattice of graphene. P-values for 10 areas of B-doped graphene and 3 areas of N-doped graphene show several orders of magnitude difference in probabilities of dopants being random distribution between B-doped and N-doped graphene, statistically indicating sublattice segregation for N dopants and randomness for B dopants.

In order to understand this, we need to consider two possible interactions relevant to the phenomenon. First, in the context of doped, free-standing graphene, there exist small differences

between the structures of B-C and N-C bonds. Even though we observe significant long range electronic interactions [53], they do not affect the total energy significantly at the typical distance between dopants [54]. Second, the B, N and C atoms are all bound to surface Cu atoms during the growth process, and differences in the B-Cu and N-Cu interactions can cause differences in sublattice segregation [34, 55]. Our results shown in Fig. 4.9a and Fig. 4.9b illustrate that this affect can be quite different between B and N dopants once they are incorporated. While further studies would be required to confirm the exact cause for this behavior, the sublattice correlation that we observe in conjunction with different B-Cu versus N-Cu interactions may well reflect the hypothesized role of the metal substrate in the growth process [56, 57]. Systematic growth experiments on different substrates can potentially give more insights into this issue. Moreover, our observation of sublattice segregation in N-doped graphene is important for a number of exciting applications. For example, breaking the sublattice symmetry of graphene destroys the pseudospin degeneracy and introduces a band gap at Dirac points. Theoretical work has predicted that dopants in the same sublattice are most efficient in breaking the sublattice symmetry [58]. We have not observed such a band gap in our STM spectroscopy experiments thus far, chiefly because we are studying samples with low dopant concentrations. Further spectroscopy and transport measurements in heavily doped regime can be employed to elucidate band gap formation.

4.4 NEXAFS Characterizations on B-doped graphene

A confirmation that B is present in the structure is provided by near-edge x-ray absorption fine structure spectroscopy (NEXAFS) measurements. A NEXAFS spectrum (Fig. 4.15) taken on a “tube-doped” B-doped graphene/Cu foil at Boron 1s edge shows clear resonances at energies of 192.0 and 200.0eV. The intensity of the resonances is strongly dependent on the electric field polarization,

and both the energy and polarization dependence of the resonances are completely consistent with the π and σ states of sp^2 bonded graphitic boron [11].

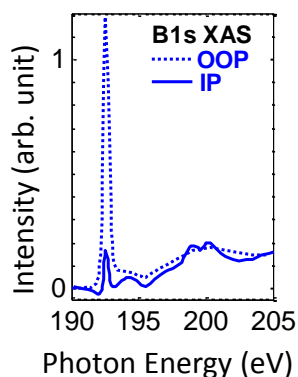


Fig. 4.15 NEXAFS of “tube-doped” graphene on Cu foil measured at B1s edge, with E-field polarization dependence.

4.5 Brief Discussions on “Flow-doped” Graphene

So far in this Chapter, we have focused on “tube-doped” graphene films. To make a complete story, we devote this section to brief discussions on the results from the “flow-doped” graphene samples. Here, the “flow-doped” term refers to inclusion of B_2H_6 flow during the graphene growth, as opposed to the absence of B_2H_6 flow in “tube-doped” graphene case. Typically, the flow rate of B_2H_6 is controlled to be from 1sccm to 5sccm while that for CH_4 and H_2 are 6sccm and 100sccm respectively.

Fig. 4.16a displays a large scale STM topographic image taken on the “flow-doped” graphene samples. We clearly see a much larger background corrugations and a much higher concentration of defect structures over this surface than on the “tube-doped” samples. This indicates that the presence of B_2H_6 flow reacts violently with the Cu substrate and therefore perturbs the

environment for graphene growths. A zoom-in image in Fig. 4.16b shows the morphology of these defects, some of which show a triangular symmetry (red arrow) just as graphitic Boron dopants while others display much more complicate patterns (yellow arrows). All of these suggest a poor quality of the graphene films and less control over the dopant structures.

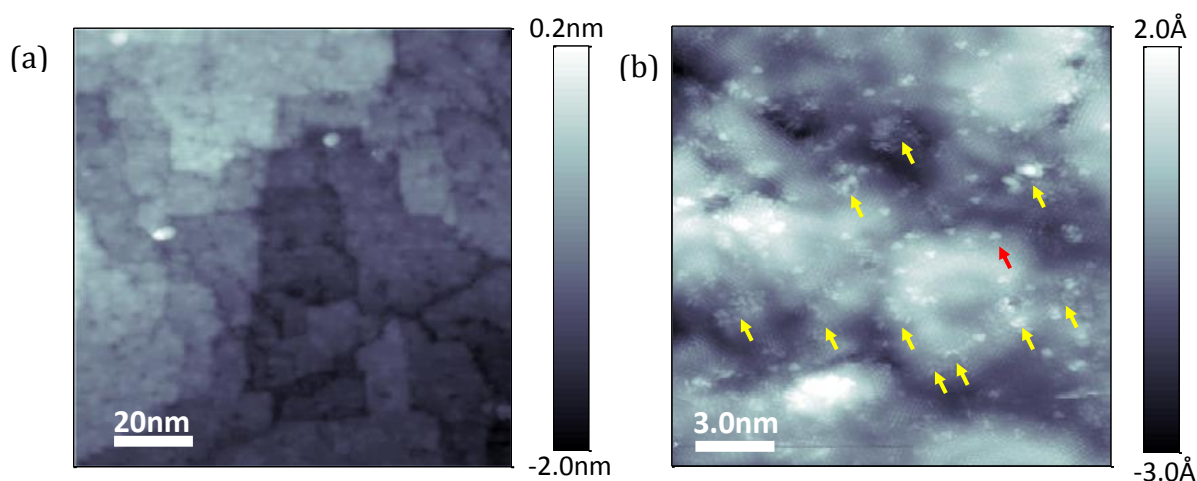


Fig. 4.16 STM topographic images for “flow-doped” graphene on Cu foil. (a) A STM image taken over an $80 \times 80 \text{ nm}^2$ area on “flow-doped” (high B-doped) graphene on Cu foil, showing copper substrate roughness due to the presence of diborane flow during graphene growth. (b) A zoom-in STM image ($15 \times 15 \text{ nm}^2$), with yellow arrows pointing the complicate defect structures, and a red arrow indicating one of the graphitic B dopants. The background copper substrate roughness is about a few Å. Scanning conditions: $V_{bias} = -0.8 \text{ V}$ and $I_{set} = 0.5 \text{ nA}$.

4.6 References

1. Castro Neto, A.H., et al., *The electronic properties of graphene*. Reviews of Modern Physics, 2009. 81(1): p. 109-162.
2. Geim, A.K. and K.S. Novoselov, *The rise of graphene*. Nat Mater, 2007. 6(3): p. 183-191.
3. Geim, A.K., *Graphene: Status and Prospects*. Science, 2009. 324(5934): p. 1530-1534.
4. Novoselov, K.S., et al., *Two-dimensional gas of massless Dirac fermions in graphene*. Nature, 2005. 438(7065): p. 197-200.
5. Zhang, Y., et al., *Experimental observation of the quantum Hall effect and Berry's phase in graphene*. Nature, 2005. 438(7065): p. 201-204.

6. Williams, J.R., L. DiCarlo, and C.M. Marcus, *Quantum Hall Effect in a Gate-Controlled p-n Junction of Graphene*. Science, 2007. 317(5838): p. 638-641.
7. Young, A.F. and P. Kim, *Quantum interference and Klein tunnelling in graphene heterojunctions*. Nat Phys, 2009. 5(3): p. 222-226.
8. Zhao, L., et al., *Visualizing Individual Nitrogen Dopants in Monolayer Graphene*. Science, 2011. 333(6045): p. 999-1003.
9. Sheng, Z.-H., et al., *Synthesis of boron doped graphene for oxygen reduction reaction in fuel cells*. Journal of Materials Chemistry, 2012. 22(2): p. 390-395.
10. Lin, T., et al., *A facile preparation route for boron-doped graphene, and its CdTe solar cell application*. Energy & Environmental Science, 2011. 4(3): p. 862-865.
11. Hanafusa, A., et al., *Local structure analysis of boron-doped graphite by soft x-ray emission and absorption spectroscopy using synchrotron radiation*. Journal of Applied Physics, 2011. 110(5): p. 053504-6.
12. Cattelan, M., et al., *Microscopic View on a Chemical Vapor Deposition Route to Boron-Doped Graphene Nanostructures*. Chemistry of Materials, 2013. 25(9): p. 1490-1495.
13. Gebhardt, J., et al., *Growth and electronic structure of boron-doped graphene*. Physical Review B, 2013. 87(15): p. 155437.
14. Kim, Y.A., et al., *Raman spectroscopy of boron-doped single-layer graphene*. ACS nano, 2012. 6(7): p. 6293-6300.
15. Wang, H., et al., *Synthesis of Boron - Doped Graphene Monolayers Using the Sole Solid Feedstock by Chemical Vapor Deposition*. Small, 2013.
16. Panchakarla, L.S., et al., *Synthesis, Structure, and Properties of Boron- and Nitrogen-Doped Graphene*. Advanced Materials, 2009. 21(46): p. 4726-4730.
17. Turnbull, J., M. Stagg, and W. Eeles, *Annealing studies of boron-doped graphite by electron microscopy and X-ray diffraction*. Carbon, 1966. 3(4): p. 387-392.
18. Ferro, Y., et al., *Adsorption, diffusion, and recombination of hydrogen on pure and boron-doped graphite surfaces*. The Journal of chemical physics, 2004. 120: p. 11882.
19. Hishiyama, Y., et al., *Structure, Raman scattering, and transport properties of boron-doped graphite*. Physical Review B, 2001. 63(24): p. 245406.
20. Endo, M., et al., *Scanning tunneling microscope study of boron-doped highly oriented pyrolytic graphite*. Journal of Applied Physics, 2001. 90(11): p. 5670-5674.
21. Mele, E. and J. Ritsko, *Electronic excitations in boron-doped graphite*. Physical Review B, 1981. 24(2): p. 1000.
22. Cermignani, W., et al., *Synthesis and characterization of boron-doped carbons*. Carbon, 1995. 33(4): p. 367-374.
23. Hagio, T., M. Nakamizo, and K. Kobayashi, *Studies on X-ray diffraction and Raman spectra of B-doped natural graphite*. Carbon, 1989. 27(2): p. 259-263.
24. Kouvetakis, J., M. McElfresh, and D. Beach, *Chemical vapor deposition of highly conductive boron-doped graphite from triphenyl boron*. Carbon, 1994. 32(6): p. 1129-1132.
25. Turnbull, J.A., M.S. Stagg, and W.T. Eeles, *Annealing studies of boron-doped graphite by Electron Microscopy and X-ray Diffraction*. Carbon, 1966. 3(4): p. 387-392.
26. Guo, T., C. Jin, and R. Smalley, *Doping bucky: formation and properties of boron-doped buckminsterfullerene*. The Journal of Physical Chemistry, 1991. 95(13): p. 4948-4950.

27. Muhr, H.-J., et al., *The boron heterofullerenes $C_{59}B$ and $C_{69}B$: generation, extraction, mass spectrometric and XPS characterization*. Chemical physics letters, 1996. 249(5): p. 399-405.
28. McGuire, K., et al., *Synthesis and Raman characterization of boron-doped single-walled carbon nanotubes*. Carbon, 2005. 43(2): p. 219-227.
29. Golberg, D., et al., *Single-walled B-doped carbon, B/N-doped carbon and BN nanotubes synthesized from single-walled carbon nanotubes through a substitution reaction*. Chemical Physics Letters, 1999. 308(3): p. 337-342.
30. Han, W., et al., *Boron-doped carbon nanotubes prepared through a substitution reaction*. Chemical physics letters, 1999. 299(5): p. 368-373.
31. Redlich, P., et al., *$B \cdot C \cdot N$ nanotubes and boron doping of carbon nanotubes*. Chemical physics letters, 1996. 260(3): p. 465-470.
32. Kim, K.S., et al., *Large-scale pattern growth of graphene films for stretchable transparent electrodes*. Nature, 2009. 457(7230): p. 706-710.
33. Li, X., et al., *Large-Area Synthesis of High-Quality and Uniform Graphene Films on Copper Foils*. Science, 2009. 324(5932): p. 1312-1314.
34. Chakrabarti, D.J. and D.E. Laughlin, *The B-Cu (Boron-Copper) system*. Bulletin of Alloy Phase Diagrams, 1982. 3(1): p. 45-48.
35. Perdew, J.P. and A. Zunger, *Self-interaction correction to density-functional approximations for many-electron systems*. Physical Review B, 1981. 23(10): p. 5048-5079.
36. Zheng, B., P. Hermet, and L. Henrard, *Scanning Tunneling Microscopy Simulations of Nitrogen- and Boron-Doped Graphene and Single-Walled Carbon Nanotubes*. ACS Nano, 2010. 4(7): p. 4165-4173.
37. Zhang, Y., et al., *Giant phonon-induced conductance in scanning tunnelling spectroscopy of gate-tunable graphene*. Nat Phys, 2008. 4(8): p. 627-630.
38. Woińska, M., K.Z. Milowska, and J.A. Majewski, *Electronic Structure of Graphene Functionalized with Boron and Nitrogen*. arXiv. 1301. 3956, 2012.
39. Wintterlin, J. and M.L. Bocquet, *Graphene on metal surfaces*. Surface Science, 2009. 603(10-12): p. 1841-1852.
40. Cockayne, E., et al., *Grain boundary loops in graphene*. Physical Review B, 2011. 83(19): p. 195425.
41. Cockayne, E., *Graphing and grafting graphene: Classifying finite topological defects*. Physical Review B, 2012. 85(12): p. 125409.
42. Park, H.J., et al., *Growth and properties of chemically modified graphene*. physica status solidi (b), 2010. 247(11-12): p. 2915-2919.
43. Meyer, J.C., et al., *Experimental analysis of charge redistribution due to chemical bonding by high-resolution transmission electron microscopy*. Nat Mater, 2011. 10(3): p. 209-215.
44. Guisinger, N.P., et al. *Atomic-scale investigation of graphene formation on 6H-SiC(0001)*. 2008. Seattle, Washington (USA): AVS.
45. Kim, E., I. Oh, and J. Kwak, *Atomic structure of highly ordered pyrolytic graphite doped with boron*. Electrochemistry Communications, 2001. 3(11): p. 608-612.
46. Peres, N.M.R., F. Guinea, and A.H. Castro Neto, *Electronic properties of disordered two-dimensional carbon*. Physical Review B, 2006. 73(12): p. 125411.

47. Červenka, J. and C.F.J. Flipse, *Structural and electronic properties of grain boundaries in graphite: Planes of periodically distributed point defects*. Physical Review B, 2009. 79(19): p. 195429.
48. Yazyev, O.V. and S.G. Louie, *Topological defects in graphene: Dislocations and grain boundaries*. Physical Review B, 2010. 81(19): p. 195420.
49. Yazyev, O.V. and S.G. Louie, *Electronic transport in polycrystalline graphene*. Nat Mater, 2010. 9(10): p. 806-809.
50. Grantab, R., V.B. Shenoy, and R.S. Ruoff, *Anomalous Strength Characteristics of Tilt Grain Boundaries in Graphene*. Science, 2010. 330(6006): p. 946-948.
51. Moran, P.A.P., *Notes on Continuous Stochastic Phenomena*. Biometrika, 1950. 37(1/2): p. 17-23.
52. Lehmann, E.L. and Springer, *Testing Statistical Hypotheses (Springer Texts in Statistics)*. 1997: Springer.
53. Lambin, P., et al., *Long-range interactions between substitutional nitrogen dopants in graphene: Electronic properties calculations*. Physical Review B, 2012. 86(4): p. 045448.
54. Xiang, H.J., et al., *Ordered Semiconducting Nitrogen-Graphene Alloys*. Physical Review X, 2012. 2(1): p. 011003.
55. Yoshimoto, Y. and S. Tsuneyuki, *First-principles study of inter-nitrogen interaction energy of Cu(100)-c(2 × 2)N surface*. International Journal of Quantum Chemistry, 2003. 91(2): p. 211-215.
56. Artyukhov, V.I., Y. Liu, and B.I. Yakobson, *Equilibrium at the edge and atomistic mechanisms of graphene growth*. Proceedings of the National Academy of Sciences, 2012.
57. Shu, H., et al., *Edge Structural Stability and Kinetics of Graphene Chemical Vapor Deposition Growth*. ACS Nano, 2012. 6(4): p. 3243-3250.
58. Rani, P. and V.K. Jindal, *Designing band gap of graphene by B and N dopant atoms*. arXiv. 1209.5228, 2012.

Chapter 5

Nitrogen Dopant Distribution in N-doped Graphene Polycrystal

5.1 Background of Impurity/Dopant Distribution

Most materials with sizes at macroscopic scales are inevitable to have grains and defect lines between grains (i.e. structural grain boundaries) [1, 2]. When impurities of heteroatoms are present in these materials, the interplay between the heteroatoms and intrinsic defects plays an important role in determining the electronic and structural properties of the host materials. This has been an intensely studied subject in three-dimensional polycrystalline materials [3-11], and recently is introduced into materials with lower dimensionality [12, 13] due to the realization of atomic thick materials [14].

5.1.1 Review of Dopant Distribution in Three-dimensional Polycrystals

Doping and functionalization are common strategies by which the electronic properties of the host materials can be tuned. Understanding the spatial homogeneity of the doping or functionalization process is key to achieving the control over the material's electronic properties. In three-dimensional polycrystalline materials such as ceramics [3, 4], semiconductors [5-8] and so on [15-18], atomic impurities and dopants are well known to migrate towards surfaces and grain

boundaries during the growth/doping processes, resulting in an inhomogeneous modification of the electronic and structural properties of the host materials.

Dating back to 1980s, it was very puzzled that the electrical properties of doped polycrystalline silicon are markedly different from those of single crystal silicon. In particular, in the low doping level regime, the resistivity of polycrystalline Si is several orders of magnitude higher than that of single crystal one and is not sensitive to the variations of dopant concentration. To a medium dopant density, a small increase of dopant density results in a dramatic drop in resistivity. And finally in the high dopant concentrations, the resistivity approaches that of single crystal ones. Massive experiments [8, 19-24] were done trying to solve this mystery and came up with two possible models. One is the carrier trapping model [8, 19, 20] and the other is the dopant segregation model [23, 24]. The latter one, in which it is stated that the dopant atoms migrate towards the structural grain boundaries and become electronically inactive, has been proved to be the major factor in determining the electrical properties of doped Si polycrystals [9], especially with advanced imaging techniques [7]. In fact, not only Si, other polycrystalline semiconductors and ceramics exhibit the same character in terms of dopant segregation.

Apart from structural grain boundaries, interfaces between two different materials also attract the impurities, for instance, interfaces in quantum well structures [10, 11]. *P.M. Petroff et al* reported in 1978 that the impurities at the interface of GaAs –GaAlAs accumulate from the nucleation and growth processes, and roughens the interfaces, depending on the order in which the GaAs and GaAlAs layers were deposited [10]. A follow-up study from *P.M. Petroff et al* proposed more possible mechanisms for impurity trapping towards the interfaces, including the impurity solubility difference in GaAs and GaAlAs, and the misfit strain between the two materials. The origin

of the impurity nucleation towards the interfaces was under investigation, but the phenomenon was clearly shown in multiple experiments [11].

5.1.2 Chances in Chemically Doped Two-dimensional Polycrystals

The discovery of the atomic thick materials opens a new field of researches in lower dimensionality [14, 25]. As we could imagine, a defect line has a much more significant impact in two-dimensional materials than that in three-dimensional materials, simply due to the fact that the defect-lines with the same length take up much higher “surface to bulk ratio” in lower dimensions. As such, we would expect the interplay between impurities and structural grain boundaries in two-dimensional systems to be dramatically different from that in the traditional three-dimensional materials.

Up to now, successful syntheses of large-area monolayer films have been achieved in a couple of systems including graphene [26] and MoS₂ [27, 28]. Of particular interest is that nitrogen-doped monolayer graphene films have been produced by a wide variety of techniques, and microscopic measurements of this functionalized material have already revealed the atomic-scale doping forms and local electronic properties of this material [29-32]. At the micrometer scale, it is well known that chemical vapor deposition (CVD) grown graphene films are polycrystalline [33, 34]. However, the macroscopic electronic properties are still not clearly explained [35] partially due to the lack of knowledge on the dopant concentration variations within grains and across grains.

Therefore, the nitrogen-doped monolayer graphene films are an ideal medium in which to study spatial homogeneity of doping within grains and across grain boundaries. This study, in turn, also provides us with key information to produce high-quality doped graphene films for electronic application.

5.1.3 Approaches and Subjects in Our Experiments

In this chapter, we will present our results on nitrogen dopant distribution in polycrystalline nitrogen-doped monolayer graphene films, as well as single crystalline nitrogen doped graphene islands.

Nitrogen doped monolayer graphene films were grown using low-pressure CVD technique on Cu foil substrates [26]. To investigate the effect of the growth conditions on the results we obtained, we performed growth with two types of precursor gases. The first type is a mixture of H_2 , CH_4 and NH_3 , as described in Chapter 3 [36], and the second one is pyridine vapor, a single source for both nitrogen and carbon [37]. Here, we denote the samples prepared in the first recipe as NG_Xm, where NG stands for nitrogen doped monolayer graphene sheet and Xm for a growth time of X minutes, and the samples grown with the second method by NG_Pyridine. A brief description of both recipes is as follows:

- (1) *Precursors of H_2 , CH_4 and NH_3 .* The copper foil substrate was cleaned with a flow of 10 sccm H_2 at a pressure of 0.055torr and a temperature of 1000°C for 10 minutes. Doped graphene films were then synthesized using a mixture of H_2 (10sccm), CH_4 (170sccm) and NH_3 (0.10torr partial pressure) at a total pressure of 1.9torr and temperature of 1000°C for growths of 5mins (NG_5m), 8mins (NG_8m), 10mins (NG_10m), 14mins (NG_14m) and 18mins (NG_18m).
- (2) *Precursor of Pyridine.* The copper foil substrate was first cleaned in ultra-high-vacuum (UHV) by Ar^+ ion bombardment and post-annealing cycles to obtain a fresh copper

surface. Doped graphene films were then grown using Pyridine at a pressure of 1mtorr and a temperature of 950°C for 30mins, denoted as NG_Pyridine.

As we have learnt from the STM and XPS characterizations in Chapter 3 that the typical nitrogen dopant concentration is only $\sim 0.2\%-0.5\%$ in these NG_Xm samples, conventional element analysis techniques are not sufficient here, especially when a reasonable spatial resolution is required [38]. Here, we use the high sensitivity of micro-Raman spectroscopy (532nm laser excitation) to impurities [39, 40] and free charge carriers [41, 42] in the graphene lattice to map the dopant distribution over large areas ($\sim 25 \times 25 \mu\text{m}^2$) of the films with submicron ($\sim 0.5 \mu\text{m}$) spatial resolution. We further complete these measurements with atomic-resolution scanning tunneling microscopy (STM) measurements near grain boundaries in graphene polycrystals and edges of graphene islands, which provides us direct measurements of nitrogen dopant concentrations at the nanometer scale.

5.2 Micro-Raman Spectroscopy Studies of N Dopant Distribution

5.2.1 Individual Raman Spectrum and Its Statistics on N-doped Graphene

Fig. 5.1 shows typical Raman spectra taken from a pristine graphene and a NG_10m sample transferred onto SiO_2/Si substrates. The Raman spectrum from pristine graphene shows sharp and intense well-known G and 2D bands with a 2D/G ratio of ~ 4 and a negligible D band. These features indicate that the quality of the CVD grown pristine graphene is comparable to that of the best mechanically exfoliated samples [39, 40, 43]. In contrast to the pristine graphene films, the NG_10m sample shows strong D and D' bands in the Raman spectrum, and the intensity of the 2D band is

significantly suppressed. The G band frequency displays a blue-shift compared to that of pristine graphene, as shown in the inset of Fig. 5.1. All of these observations indicate the presence of nitrogen dopants in the NG_10m graphene film, which act as defects in the graphene lattice and contribute free charge carriers to the graphene films [39-43].

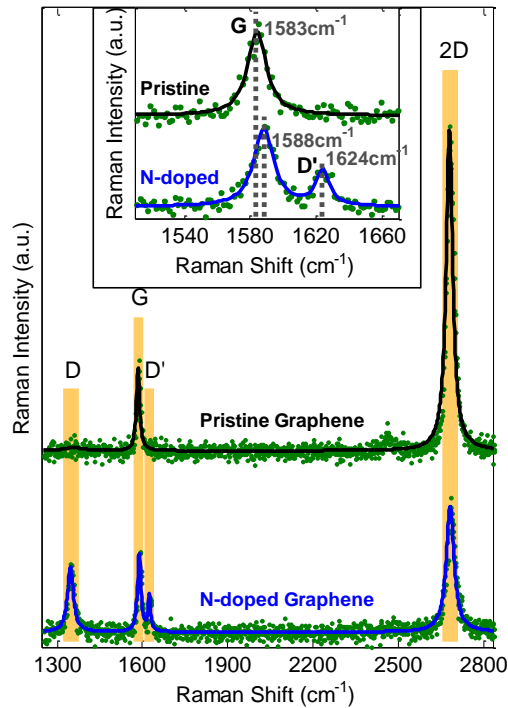


Fig. 5.1 Raman Spectra of pristine graphene (black line) and nitrogen-doped graphene (blue line) films transferred on to SiO_2/Si substrates, with D, G, D' and 2D bands highlighted in yellow background. The inset shows a zoom-in plot in the range of G and D' bands. Clear differences are observable between Raman spectra of pristine and nitrogen-doped graphene films.

As a confirmation that the transferring process does not introduce the extra features in NG_10m sample, we display Raman spectra taken on both as-grown pristine and NG_10m samples on Cu foil substrates in Fig. 5.2. The background in both spectra results from the luminescence of Cu substrates, and so does the poor signal to noise ratio. Furthermore, the peak shape is distorted and

the peak frequency is slightly shifted mainly due to the interactions (such as strain) between graphene layers and underneath Cu substrate [44]. Except these difficulties brought by the presence of Cu substrates, D and D' bands are clearly seen in NG_10m sample while they are absent in the pristine sample. For the convenience in Raman measurements and subsequent explanations, we therefore transferred the graphene films on to SiO₂/Si substrates for the Raman characterizations in the following parts of this chapter.

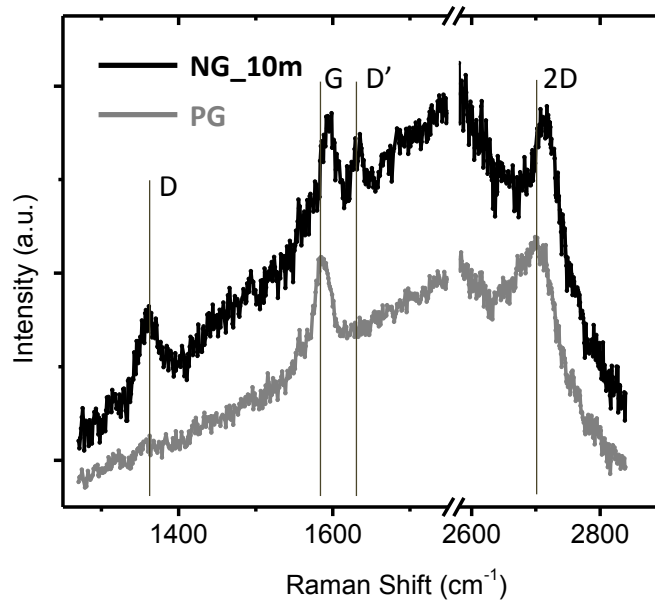


Fig. 5.2 Raman spectra taken on as-grown pristine (gray lines) and nitrogen-doped (black lines) graphene films on Cu foil substrates. Signature bands, D, G, D', and 2D are marked with vertical gray lines. The appearance of D and D' bands in NG_10m sample in addition of G and 2D bands indicates the presence of nitrogen dopants in NG_10m, despite the background from the Cu substrate luminescence.

In order to make the differences between pristine and nitrogen-doped graphene more statistically relevant, Raman spectroscopy maps were acquired on both films comprising of 4096 (64 × 64) data points examined over a 25 × 25 μm² area on each sample.

Fig. 5.3a shows the statistical distribution of G band frequencies taken over both samples. The statistical mean of the G band position for sample NG_10m (light blue blocks) is at 1589 cm^{-1} while the pristine graphene produced by the same mean has an average G band frequency of 1584 cm^{-1} . This indicates that the NG_10m sample is on average electron doped, with a carrier concentration of $\sim 7.5 \times 10^{12} \text{ cm}^{-2}$ [41, 42]. Previous STM measurements have shown that the number of electron carriers from per nitrogen dopant is approximately constant ($\sim 0.42e/N$) over a wide range of nitrogen concentration [29]. We can thus linearly scale the G peak frequency with the local nitrogen dopant concentration.

We plot the intensity ratios of the signature bands in Raman spectra as a function of G band frequency in Fig. 5.3b, both for pristine graphene (left panel with light gray background) and for NG_10m sample (right panel with light blue background). From this figure, we see that in the pristine graphene, the 2D/G ratio stays high at $\sim 3-4$ and all the other ratios (D/G, D'/G, and D/2D) are nearly zero, in accord with previous measurement on mechanically exfoliated graphene films on SiO_2/Si substrate. On the other hand, sample NG_10m shows non-zero values of the D/G, D'/G and D/2D ratios, consistent with the presence of nitrogen dopants in the graphene lattice. We note that both the D/G and D'/G intensities are linearly proportional to the G band frequency, and thus also to the N dopant concentration. Our results are consistent with previous experiments on intentionally disordered graphene films [43], indicating that the chief effect of the nitrogen dopants on the Raman spectra is to provide atomic-scale defects that make the D and D' band visible. The absolute difference in the D and D' band intensities is due to the difference in the scattering cross sections of D and D' bands [43, 45]. The effect of nitrogen doping decreases the 2D peak intensity due to increasing carrier concentration in the graphene films, as well as the addition of structural defects to the graphene lattice. The 2D/G ratio thus displays a non-linear dependence on the G band

frequency. Finally, the D/2D ratio combines the opposing trend of the D/G and 2D/G ratios on nitrogen dopant concentration, and is thus the most sensitive indicator of nitrogen dopant density in the following analysis for investigating the spatial variations of effects of nitrogen dopant density.

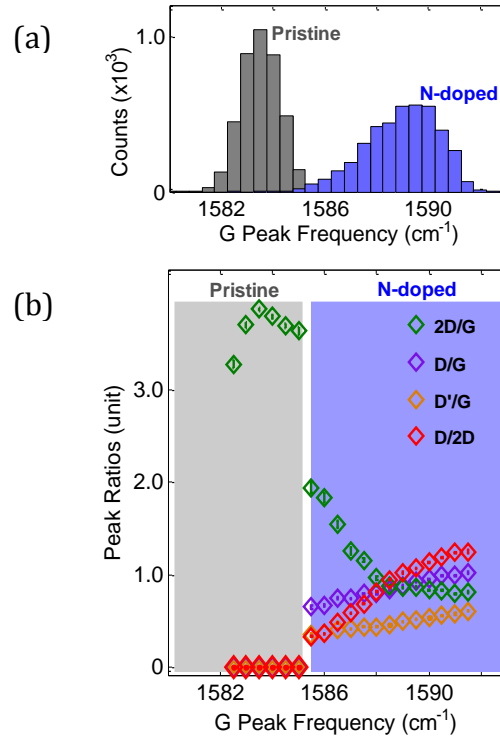


Fig. 5.3 Statistics of Raman spectra taken on pristine and nitrogen-doped graphene films. (a) Statistics of G band frequencies on pristine (gray blocks) and nitrogen-doped (light blue blocks) graphene samples over $25 \times 25 \mu\text{m}^2$ areas (64×64 pixels); (b) Statistical relations between peak intensity ratios, including D/G, D'/G, 2D/G and D/2D with respect to G band frequencies.

5.2.2 Raman Mapping on N-doped Graphene

As we have shown variations of G peak frequency, D/G, and D'/G and D/2D ratios for both pristine graphene and NG_10m sample in the last section, we wonder how these variations situate in real

space and whether they have any correlations with the structural features of graphene polycrystals. So in the following part of this section, we will first take a look at real space mappings of pristine graphene, and then move forwards to the nitrogen doped case.

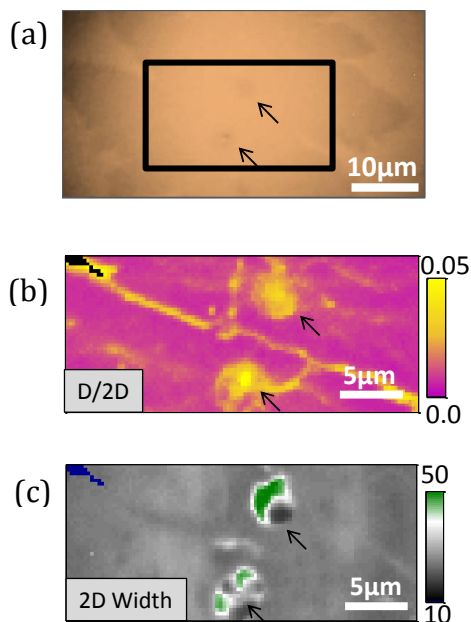


Fig. 5.4 Grain boundaries in pristine graphene imaged by Raman maps. (a) An optical image of a CVD grown pristine graphene, with two seeds highlighted by two arrows. (b) Raman map of the D/2D intensity ratio at the area highlighted by the rectangular box in (a), with two arrows indicating the two seeds (high D/2D ratio of ~ 0.04). A line with high D/2D ratio of ~ 0.04 is present between the two seeds, indicative of a grain boundary there. (c) 2D width map taken at the same area as (b), with wider 2D width highlighted with two arrows, further confirming the growth of multilayer graphene at the seeding center of each grain.

Grain boundaries and nucleation seeds are the primary sources of structural disorder in pristine graphene grown by CVD technique. We can visualize these structural features in an optical microscope, as shown in Fig. 5.4a. The two darker regions highlighted by the arrows are the nucleation seeds of two domains where multilayer graphene is typically found [46]. We expect a

grain boundary to exist in the graphene monolayer between these two seeds. Indeed, Raman spectral maps show evidence for this as indicated in Fig. 5.4b, which illustrates the D/2D ratio map in the same area as highlighted by the black rectangle in Fig. 5.4a. This map shows a line where the D/2D ratio is higher than the rest of the map, consistent with the presence of a grain boundary [47]. The existence of multilayer graphene films at the nucleation seeds is further confirmed by an image of the 2D band width shown in Fig. 5.4c.

Having understood the effect of grain boundaries and similar structural features on the Raman spectra of pristine graphene films, we are now in a position to study the interactions between these structural features and nitrogen dopants in chemically doped graphene sheets. Shown in Fig. 5.5a is an optical image of a monolayer NG_{10m} sample, where we can see these dark spots spread over the surface with an averaged distance of $\sim 3\text{-}5\mu\text{m}$. Just as in the case of pristine graphene, these dark features in optical images are associated with the multilayer growth at the nucleation centers of the grains. A D/2D ratio map taken at the same area as the optical image is shown in Fig. 5.5b. The map shows a clear patchwork structure as might be expected from a polycrystal sample. Surprisingly, however, the image shows that the D/2D ratio intensity is much smaller on the patch boundaries than that to the interior of the patches (which is relatively uniform), in complete contrast to our measurements on pristine graphene films. For the NG_{10m} sample, the average D/2D ratio at the patch boundaries is ~ 0.1 , while it is ~ 1.2 in the interior of the patches. This compares to a D/2D ratio of ~ 0.04 at the grain boundaries and ~ 0.0 in the interior for pristine graphene. Moreover, when we take a look at the 2D width map in Fig. 5.5c, we found the same patch boundaries as in Fig. 5.5b, and higher 2D width dots within each of the patches, signaling the presence of multilayers in the patches. The coincidence of the dark spots in Fig. 5.5a with the high 2D width spots in Fig. 5.5c further confirms that these dark sparkles are the

multilayers typically growing from the same nucleation seeds as the first layer. Better visualization would be gained at longer growth time when the second layers get appreciable sizes. Therefore, the surprising conclusion that one can reach from these facts is that the nitrogen dopant concentration at the grain boundaries is much lower than that in the interior of the grains, while the interior of each grain is fairly uniformly doped.

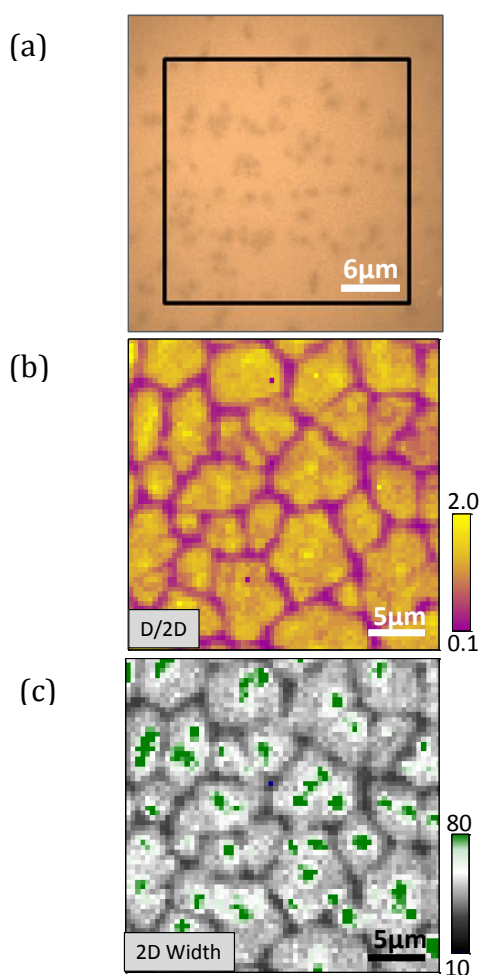


Fig. 5.5 Raman mapping on NG_{10m} sample. (a) An optical image of a fully covered NG_{10m} sample. (b) and (c) Raman maps of D/2D and 2D width in the area highlighted with black box in (a). A clear patchwork structure is observable in both maps, with lower dopant concentration at the boundaries of the patches but relative uniform nitrogen dopant distribution inside patches.

Natural questions that arise from our observation of dopant inhomogeneity are whether the observed effect of less nitrogen dopants is limited to grain boundaries, and what the possible role of the growth conditions are on the observed inhomogeneity.

To gain further insight into these questions, we first grew a series of samples using the same growth process with varying growth times of 5mins, 8mins, 10mins, and 14mins. Using optical microscopy on the samples transferred onto SiO_2/Si substrates, we confirm that the fabricated samples are in a range from a partial monolayer (NG_5m growth) through a fully formed monolayer (NG_8m and NG_10m growths) to a partially formed bilayer (NG_14m growth). We obtained Raman spectral maps of each of these samples, as shown in Fig. 5.6a-c (D/2D ratio maps) and Fig. 5.6d-f (2D width maps). A clear picture of the evolution of dopant distribution is obtained from the D/2D ratio maps. At short times (NG_5m), the areas in the immediate vicinity of the nucleation seeds are relatively undoped, while the regions outside the central core are doped. The dopant distribution at the very edge of the individual islands is generally not resolved in the Raman images (with the exception of the places where low nitrogen concentration is observed at the grain boundaries when two grains merges, such as in the white rectangle area as marked in Fig. 5.6a). We will take a careful look at these regions in the discussions of the STM measurements. When the nitrogen-doped graphene first forms a complete monolayer (NG_8m), both the nucleation seeds and the grain boundaries contain less nitrogen dopants than the other regions of the graphene films. As time progresses, the doping in the interior of the film becomes more uniform (NG_10m) but the grain boundaries remain less doped. For an even longer time (NG_14m), large bilayer patches begin to form around the nucleation seeds, but the grain boundaries always stay less doped. Based on the fact that the second layers usually grow at the same seeds as the first layers [46], the doping domains with the nitrogen depletion boundaries are the same as the structural grain boundaries of

the nitrogen-doped graphene polycrystal. This finding actually states the fact that the nitrogen dopants avoid the structural grain boundaries in the CVD grown nitrogen-doped graphene polycrystals.

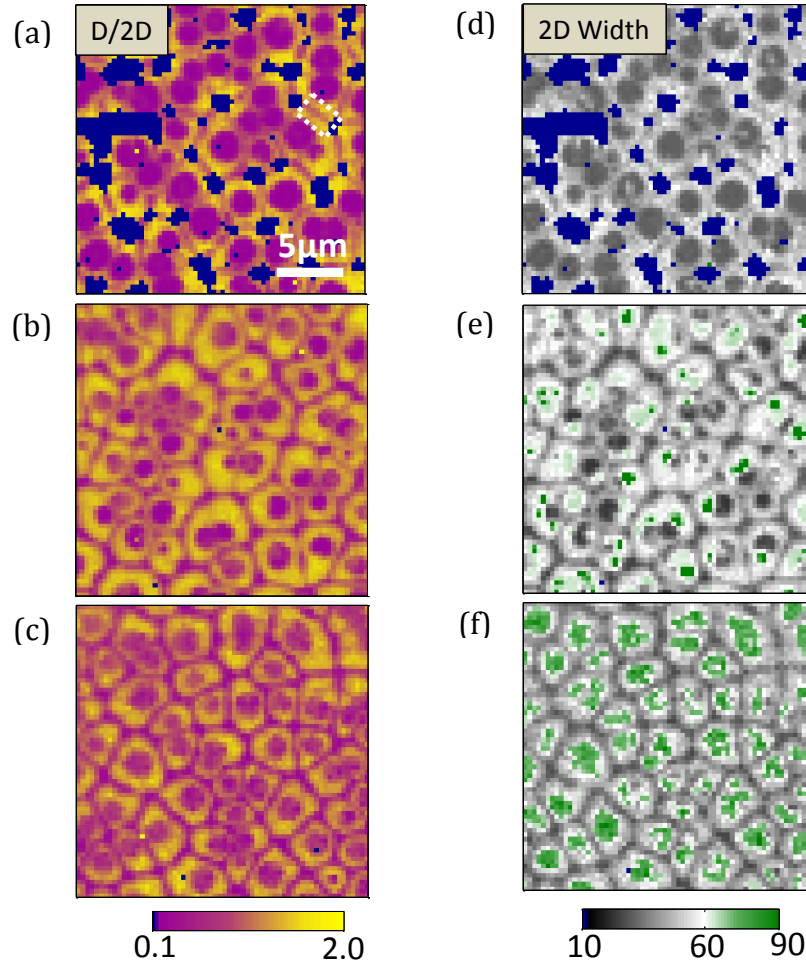


Fig. 5.6 Raman maps of NG_xm graphene films with difference growth time. (a)-(c) Raman maps of D/2D ratios for NG₅m, NG₈m, and NG₁₄m samples respectively. (d)-(e) Raman maps of 2D widths for NG₅m, NG₈m, and NG₁₄m samples respectively. Through this set of Raman maps, a clear picture of graphene film evolution as function of time is observed, with the second layer of films grown at the seeds of the first layers, and the grain boundaries remaining nitrogen depleted as time progresses.

To confirm that these results are not specific to the use of ammonia as a dopant gas, we have used pyridine as a single precursor to grow nitrogen-doped monolayer graphene. Raman spectral maps of this sample (NG_Pyridine) are shown in Fig. 5.7a and b for D/2D map and 2D width map respectively. These maps clearly exhibit the same basic phenomenology as the ammonia doping process that the nitrogen dopants stay away from the grain boundaries although the center of each grain is still less doped (similar to the case of NG_8m sample).

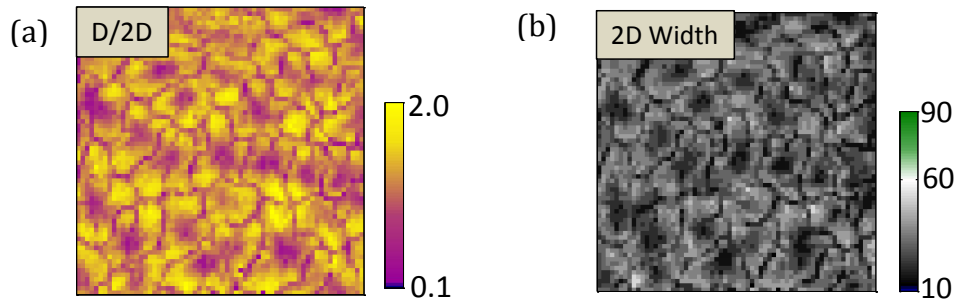


Fig. 5.7 Raman maps of NG_Pyridine samples. (a) Raman map of D/2D intensity ratio over a $25 \times 25 \mu\text{m}^2$ area on a NG_Pyridine sample. (b) Raman map of 2D width on the same area as in (a). The patchwork structure with nitrogen depleted grain boundaries is still present in this sample, indicative of the independence of this phenomenology on the growth conditions.

In order to estimate the average widths of the nitrogen depleted boundaries, we adopt a simple two-step scheme described as following, under the assumption that

$$width = \frac{area}{circumference}. \quad (5.1)$$

The first step is to determine the circumference of the grain boundaries. We take the example of NG_10m in Fig. 5.5b. The cartoon in Fig. 5.8a outlines the grain boundaries of the patches in Fig. 5.5b, from which the total length of the boundaries is calculated, $\sim 247 \mu\text{m}$. The second step is to find the area where there are less nitrogen dopants. As discussed above, the nitrogen depleted regions

have low D/2D ratio and low 2D width as revealed in the micro-Raman maps. Therefore, we select the areas that satisfy (1) the lowest 5% of the D/2D range; (2) 2D width smaller than 45cm^{-1} in order to exclude the bilayer regions in longer growth time. In the case of Fig. 5.5, we select the areas which have $D/2D < 5\% \times (2.0 - 0.1) + 0.1 = 0.195$ and 2D width $< 45\text{cm}^{-1}$. The selected regions are shown in Fig. 5.8b with red color, from which we calculated the corresponding area of $186\mu\text{m}^2$. Simply putting the numbers in Eq. 5.1 gives an averaged width of $0.75\mu\text{m}$.

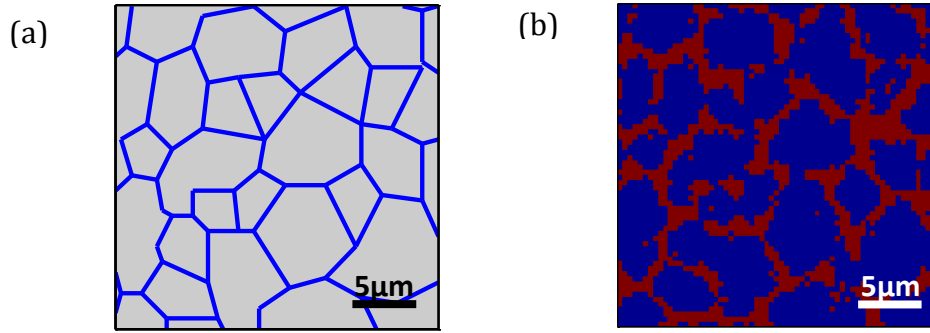


Fig. 5.8 Cartoon diagram for calculating the width of the nitrogen depleted boundaries. (a) A cartoon outlines the circumference of the grain boundaries for the Raman map in Fig. 5.5. (b) A selection of depleted nitrogen regions in Fig. 5.5b and Fig. 5.5c shows the area of these regions. The averaged width of these regions is further obtained by area in (b) divided by the circumference in (a)

Using this scheme, we get the averaged width for each of the growths and plot the results in Fig. 5.9. The estimated averaged widths of the nitrogen depleted boundaries for the samples grown with ammonia for different times are similar, about $0.6\text{-}0.8\mu\text{m}$ wide. Meanwhile, the nitrogen doped graphene films grown with pyridine have a narrower width of the dopant depleted regions, which is less than $0.5\mu\text{m}$. Despite the difference in the absolute values of the widths, all of our results consistently exhibit lower nitrogen concentration at the boundaries of the doping patches.

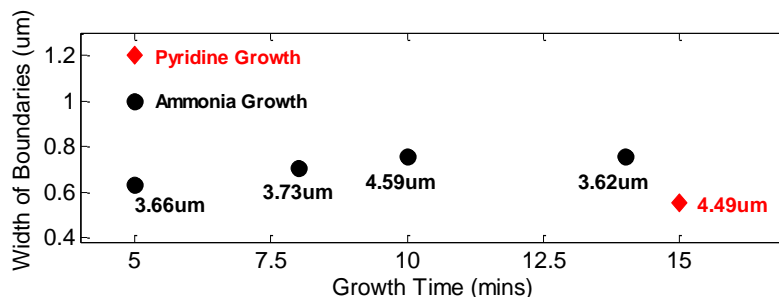


Fig. 5.9 Calculated width of nitrogen depleted grain boundaries for NG_5m, NG_8m, NG_10m, NG_14m, and NG_Pyridine. The labeled number next to each plot indicates the averaged grain size of the corresponding sample.

- All the Raman measurements were taken in collaborations with Rui He in Pinczuk group at Columbia U.

5.3 Scanning Tunneling Microscopy Studies on N Dopant Distribution

While Raman spectra give us detailed information on defect and doping concentration in graphene films, it does not directly measure the nature of the defects giving rise to the D and D' bands, and the technique is limited in spatial resolution of $\sim 0.5\mu\text{m}$ by the wave length and the spot size of the laser. To complement Raman spectroscopic measurements, we use atomically-resolved STM measurements that in the past have been employed to successfully image nitrogen dopants in graphene [29, 31, 32]. Here we use the STM to identify nitrogen dopants in graphene and to study the interaction between the dopants and the edges/grain boundaries in the graphene films. The STM measurements are performed on as-grown nitrogen doped graphene films on Cu foil and in-situ grown nitrogen doped graphene islands in UHV chamber.

5.3.1 STM of N Dopant Distribution in Polycrystalline N-doped Graphene

Shown in Fig. 5.10a is a STM topographic image (displayed in derivative mode) of a $500 \times 500 \text{ nm}^2$ area on a NG_10m sample. The overall background variations arise from the polycrystalline nature of the Cu foil substrate. The graphene monolayer forms a continuous film across this rough terrain. When the grains of graphene with different rotational angles or translational shifts merge together, a defect line is usually formed at the grain boundaries [33, 34, 48]. One of such grain boundary is observed in Fig. 5.10a, as highlighted by the black dashed line. The crystal orientations of the graphene grains on the two sides of the dashed line are rotated $\sim 18^\circ$ relative to each other as shown in Fig. 5.10b and c, further confirming the existence of the grain boundary in between. Having located the grain boundary, we can use STM to directly image the dopant concentration as a function of the distance from the boundary. Fig. 5.10d shows such an example. In this STM topography, nitrogen dopants appear as bright features due to an enhancement of local density of states at the nearest neighboring carbon sites around nitrogen dopants, as shown in previous chapters. Fig. 5.10d also clearly shows a depletion of nitrogen dopants near the grain boundary, consistent with the Raman results discussed above. We then calculated the nitrogen dopant density as a function of distance away from the grain boundary in Fig. 5.10e. A linear gradient of nitrogen concentration is observed, starting from almost zero at the grain boundary and gradually increasing to the density interior of the grain. Given the bulk value of nitrogen concentration of $\sim 0.2\%$ for this particular sample as measured by STM, we estimate the width of the nitrogen depleted region near the grain boundary to be $\sim 0.7 \mu\text{m}$. This depletion region width is in good agreement with the Raman spectroscopic measurements on the same sample (NG_10m) described in last section.

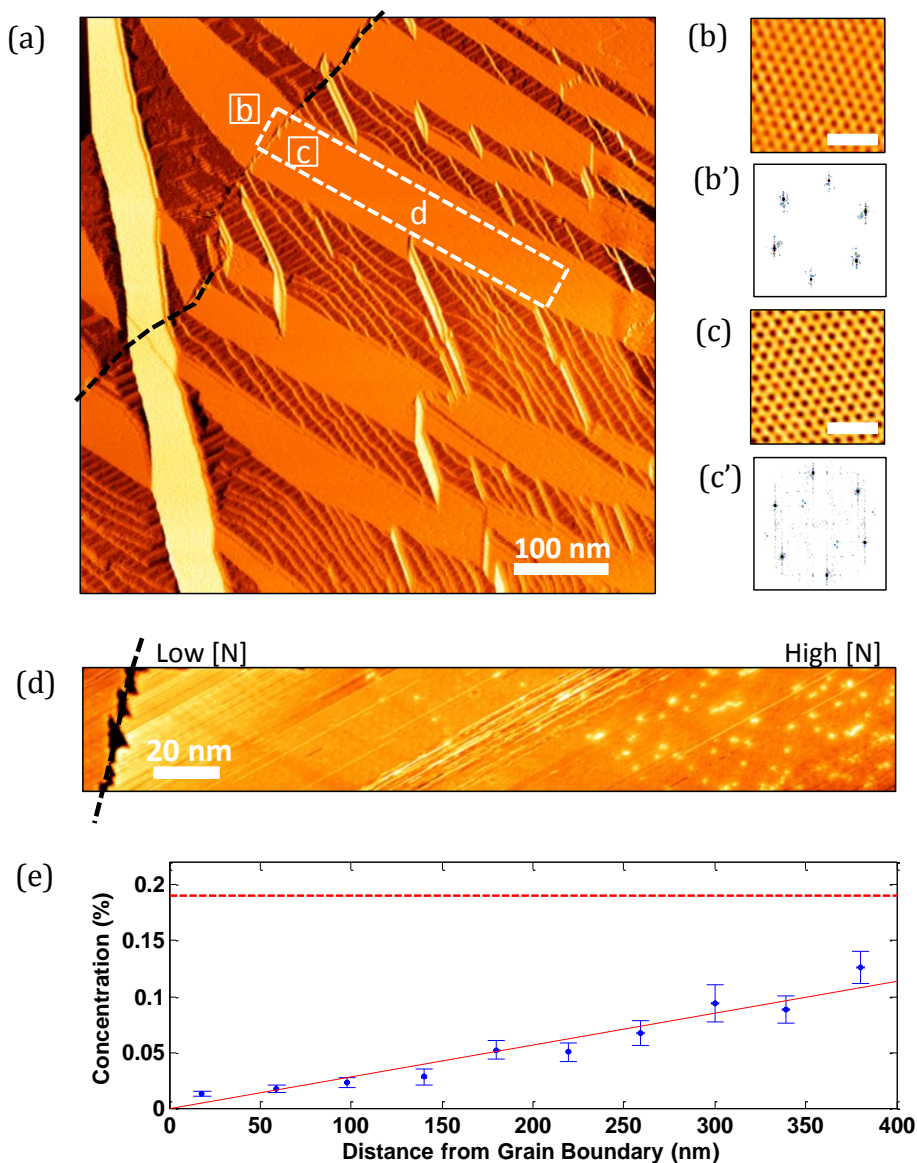


Fig. 5.10 STM topographic measurements of the nitrogen dopant distribution on as grown nitrogen-doped graphene films on Cu foil (NG_{10m}). (a) Differential STM image (500 × 500 nm², 1.5V, 0.1 nA) of an as-grown NG_{10m} sample. The black dashed line shows the location of a grain boundary; (b) and (c) Atomic resolution STM images of the corresponding areas highlighted in (a); scale bar = 1 nm. (b') and (c') FFT of STM images shown in (b) and (c), respectively; (d) STM image across a grain boundary as highlighted in (a); (e) nitrogen concentration as a function of distance from the grain boundary. The red solid line is a linear fit to the data, and dashed one is the bulk limit of nitrogen dopant concentration in this sample.

5.3.2 STM of N Dopant Distribution in N-doped Graphene Islands

To study the effect of the growth conditions, such as temperature and pressure, on the observed dopant inhomogeneity, we fabricated nitrogen-doped graphene under completely different growth conditions. We used Pyridine vapor as a single precursor under UHV conditions (pyridine pressure of 0.1mtorr and base pressure of 10^{-10} torr) on a single crystal Cu(111) at a temperature of ~ 800 - 950°C , following the procedure for pristine graphene growth [49]. We can tune the graphene coverage from isolated islands to complete monolayers depending on the growth time, and study the dopant concentration near edges and boundaries as well. As an example, we show in Fig. 5.11a a STM topographic image of $300 \times 400\text{nm}^2$ nitrogen-doped graphene island on the stepped surface of Cu(111). The graphene is identified by its apparent height on the Cu(111) substrate in STM image. We carefully studied the distribution of dopants in this island by taking high-resolution STM images across the island. Fig. 5.11b shows one such STM image obtained across one edge of this island. By taking a sequence of such images, we quantified the nitrogen dopant density over the entire island and plot the results in Fig. 5.11c. We can clearly see that the nitrogen dopants avoid the edges of the island from this image. The nitrogen concentration as a function of distance from the closest edge is plotted in Fig. 5.11d. In this sample, a linear gradient of nitrogen concentration is observed up to $\sim 60\text{nm}$ away from the edge of the island, after which the nitrogen concentration reaches a plateau at the bulk value of $\sim 0.4\%$. In addition to this nitrogen depletion at the graphene island edges, Fig. 5.11c also shows a nitrogen depleted region in the nucleation region at the center of the graphene island, which is also observed in the Raman results in Fig. 5.6 a and b. Our STM results indicate that the basic phenomenology of dopants avoiding structural defects in graphene is independent of the details of the growth conditions such as temperature, pressure and the

precursor gases used. We however note that the length scale over which the dopants avoid edges and boundaries is not a universal number, but depends on the size of the grain, with larger depletion widths observed for the large grains.

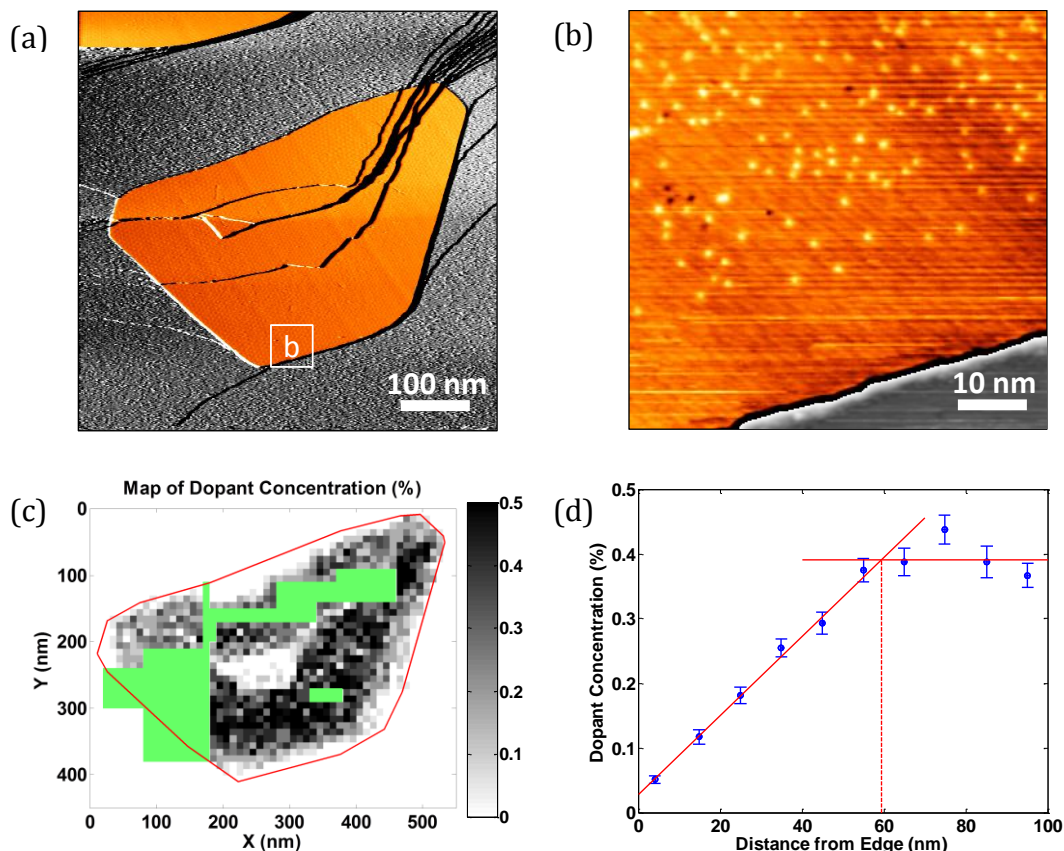


Fig. 5.11 STM topographic measurements on nitrogen-doped graphene island on Cu(111). (a) Differential STM image ($600 \times 600 \text{ nm}^2$) of graphene island. False colors: orange – graphene island, gray – Cu(111) substrate; (b) Zoom-in image ($60 \times 60 \text{ nm}^2$) taken across one edge of the graphene island at the area highlighted in (a); (c) Map of nitrogen distribution across the graphene island. Shaded boxes are areas where data is missing; (d) nitrogen concentration as a function of distance from the graphene edge. Red solid line are the linear fit to the data.

■ The STM part was done in collaboration with Amir Zabet in Flynn group at Columbia U.

5.4 Monte Carlo Simulations on N Dopant Distribution

To gain further insight into the dopant homogeneity, we use Monte Carlo (MC) techniques to simulate the kinetics of dopants in a finite-sized graphene piece, seeking possible explanation for the observed interactions between the dopants and the edges of the graphene islands.

The snapshot in Fig. 5.12a shows a typical configuration of dopant atoms throughout the simulation. We compile all the snapshots of the dopant atom distributions taken during the equilibrium stage of the simulations and generate an average density of nitrogen atoms in the sheet as shown in Fig. 5.12b. This figure clearly shows that the density of nitrogen atoms is reduced near the edge of the sheet, while it is relatively constant in the interior of the sheet. To quantify this, we calculate the distance of all the dopant atoms from their nearest edges during the equilibrium stage of the simulations, and plot the density of the dopants as a function of the distance from the nearest edge in Fig. 5.12c. We can see from this figure that the dopant density is indeed strongly reduced at the edge, and the length scale of this density reduction increases as a function of increasing system size. We extract a skin depth for each system size by fitting an exponential function to the MC data. The extracted skin depth as a function of inverse system size is shown in Fig. 5.12d. We note that the largest system we have considered is about two orders of magnitude smaller than the typical grain sizes seen in our experiments. Thus, we would not expect our skin depths to be directly comparable to experimental values. However, it is encouraging that the skin depth trend seen in our simulations is consistent with experimental values. We note that the results from the static and relaxed lattices are almost indistinguishable, indicating that strain is playing a negligible role in the dopant inhomogeneity. Our simulations do not address the effect of the substrate or the reaction kinetics of the true growth process where nitrogen and carbon atoms are present both on the surface and in

the gas phase. The fact that our simulations are able to capture the essential quantitative behavior observed in the experiments without involving these additional complications indicates that the bonding and coordination energies of the nitrogen dopants in the graphene lattice plays a key role in the observed phenomena. These general energetic considerations are expected to hold in any two-dimensional systems, and they present a challenge as well as an opportunity for creating new functionalized two dimensional materials.

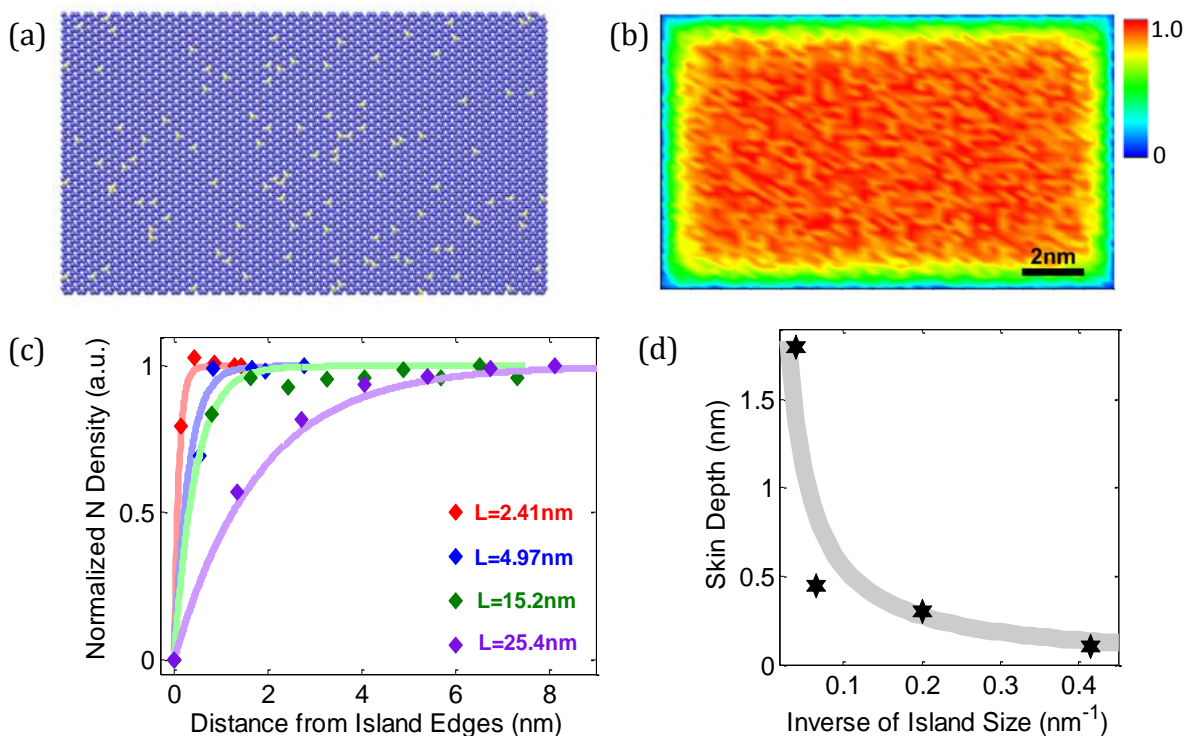


Fig. 5.12 Monte Carlo simulations of nitrogen dopant distribution in finite size graphene sheet. (a) Snap shot of simulated nitrogen distribution in an island of $15.2 \times 8.73 \text{ nm}^2$; (b) Nitrogen dopant density map ($15.2 \times 8.73 \text{ nm}^2$) averaged over time. The vertical scale bar shows the nitrogen density calibrated to the maximum value of 1; (c) Dopant density profiles for different graphene island sizes of $2.41 \times 1.35 \text{ nm}^2$, $4.97 \times 2.83 \text{ nm}^2$, $15.2 \times 8.73 \text{ nm}^2$ and $25.4 \times 14.6 \text{ nm}^2$; (d) Skin depths extracted from data in (c).

■ This theory part was done by Michael Roth at University of Northern Iowa.

5.5 References

1. Ashcroft, N. and D. Mermin, *Solid state physics*. 1976: Thomson Learning.
2. Van Swygenhoven, H., *Grain boundaries and dislocations*. Science, 2002. 296(5565): p. 66-67.
3. Bai, X.-M., et al., *Efficient Annealing of Radiation Damage Near Grain Boundaries via Interstitial Emission*. Science, 2010. 327(5973): p. 1631-1634.
4. Jia, C.L. and K. Urban, *Atomic-Resolution Measurement of Oxygen Concentration in Oxide Materials*. Science, 2004. 303(5666): p. 2001-2004.
5. Grovenor, C.R.M., *Grain boundaries in semiconductors*. Journal of Physics C: Solid State Physics, 1985. 18(21): p. 4079.
6. Maiti, A., et al., *Dopant Segregation at Semiconductor Grain Boundaries through Cooperative Chemical Rebonding*. Physical Review Letters, 1996. 77(7): p. 1306-1309.
7. Inoue, K., et al., *Three dimensional characterization of dopant distribution in polycrystalline silicon by laser-assisted atom probe*. Applied Physics Letters, 2008. 93(13): p. 133507-3.
8. Seto, J.Y.W., *The electrical properties of polycrystalline silicon films*. Journal of Applied Physics, 1975. 46(12): p. 5247-5254.
9. Mandurah, M.M., et al., *Dopant segregation in polycrystalline silicon*. Journal of Applied Physics, 1980. 51(11): p. 5755-5763.
10. Petroff, P., et al., *Crystal growth kinetics in (GaAs)_n-(AlAs)_m superlattices deposited by molecular beam epitaxy: I. Growth on singular (100) GaAs substrates*. Journal of Crystal Growth, 1978. 44(1): p. 5-13.
11. Petroff, P.M., et al., *Impurity trapping, interface structure, and luminescence of GaAs quantum wells grown by molecular beam epitaxy*. Applied Physics Letters, 1984. 44(2): p. 217-219.
12. Zou, X., Y. Liu, and B.I. Yakobson, *Predicting Dislocations and Grain Boundaries in Two-Dimensional Metal-Disulfides from the First Principles*. Nano Letters, 2012. 13(1): p. 253-258.
13. Liu, Y., X. Zou, and B.I. Yakobson, *Dislocations and Grain Boundaries in Two-Dimensional Boron Nitride*. ACS Nano, 2012. 6(8): p. 7053-7058.
14. Novoselov, K., et al., *Two-dimensional atomic crystals*. Proceedings of the National Academy of Sciences of the United States of America, 2005. 102(30): p. 10451-10453.
15. Lücke, K. and K. Detert, *A quantitative theory of grain-boundary motion and recrystallization in metals in the presence of impurities*. Acta Metallurgica, 1957. 5(11): p. 628-637.
16. Messmer, R. and C. Briant, *The role of chemical bonding in grain boundary embrittlement*. Acta Metallurgica, 1982. 30(2): p. 457-467.
17. Shvindlerman, L.S., *Grain boundary migration in metals: thermodynamics, kinetics, applications*. Vol. 9. 1999: CRC press.
18. Dimos, D., P. Chaudhari, and J. Mannhart, *Superconducting transport properties of grain boundaries in YBa₂Cu₃O₇ bicrystals*. Physical Review B, 1990. 41(7): p. 4038.
19. Baccarani, G., B. Ricco, and G. Spadini, *Transport properties of polycrystalline silicon films*. Journal of Applied Physics, 1978. 49(11): p. 5565-5570.
20. Kamins, T.I., *Hall Mobility in Chemically Deposited Polycrystalline Silicon*. Journal of Applied Physics, 1971. 42(11): p. 4357-4365.

21. Mandurah, M., K. Saraswat, and T. Kamins, *Phosphorus Doping of Low Pressure Chemically Vapor - Deposited Silicon Films*. Journal of The Electrochemical Society, 1979. 126(6): p. 1019-1023.
22. Lu, N.C.C., L. Gerzberg, and J.D. Meindl, *A quantitative model of the effect of grain size on the resistivity of polycrystalline silicon resistors*. Electron Device Letters, IEEE, 1980. 1(3): p. 38-41.
23. Cowher, M. and T. Sedgwick, *Chemical vapor deposited polycrystalline silicon*. Journal of The Electrochemical Society, 1972. 119(11): p. 1565-1570.
24. Fripp, A.L. and L.H. Slack, *Resistivity of Doped Polycrystalline Silicon Films*. Journal of The Electrochemical Society, 1973. 120(1): p. 145-146.
25. Geim, A.K. and K.S. Novoselov, *The rise of graphene*. Nature materials, 2007. 6(3): p. 183-191.
26. Li, X., et al., *Large-Area Synthesis of High-Quality and Uniform Graphene Films on Copper Foils*. Science, 2009. 324(5932): p. 1312-1314.
27. Zhan, Y., et al., *Large - Area Vapor - Phase Growth and Characterization of MoS₂ Atomic Layers on a SiO₂ Substrate*. Small, 2012. 8(7): p. 966-971.
28. Lee, Y.H., et al., *Synthesis of Large - Area MoS₂ Atomic Layers with Chemical Vapor Deposition*. Advanced Materials, 2012. 24(17): p. 2320-2325.
29. Zhao, L., et al., *Visualizing Individual Nitrogen Dopants in Monolayer Graphene*. Science, 2011. 333(6045): p. 999-1003.
30. Meyer, J.C., et al., *Experimental analysis of charge redistribution due to chemical bonding by high-resolution transmission electron microscopy*. Nat Mater, 2011. 10(3): p. 209-215.
31. Lv, R., et al., *Nitrogen-doped graphene: beyond single substitution and enhanced molecular sensing*. Sci. Rep., 2012. 2.
32. Joucken, F., et al., *Localized state and charge transfer in nitrogen-doped graphene*. Physical Review B, 2012. 85(16): p. 161408.
33. Huang, P.Y., et al., *Grains and grain boundaries in single-layer graphene atomic patchwork quilts*. Nature, 2011. 469(7330): p. 389-392.
34. Kim, K., et al., *Grain Boundary Mapping in Polycrystalline Graphene*. ACS Nano, 2011. 5(3): p. 2142-2146.
35. Wang, H., T. Maiyalagan, and X. Wang, *Review on recent progress in nitrogen-doped graphene: synthesis, characterization, and its potential applications*. Acs Catalysis, 2012. 2(5): p. 781-794.
36. Wei, D., et al., *Synthesis of N-Doped Graphene by Chemical Vapor Deposition and Its Electrical Properties*. Nano Letters, 2009. 9(5): p. 1752-1758.
37. Jin, Z., et al., *Large-Scale Growth and Characterizations of Nitrogen-Doped Monolayer Graphene Sheets*. ACS Nano, 2011. 5(5): p. 4112-4117.
38. Schiros, T., et al., *Connecting Dopant Bond Type with Electronic Structure in N-Doped Graphene*. Nano Letters, 2012. 12(8): p. 4025-4031.
39. Ferrari, A.C., *Raman spectroscopy of graphene and graphite: Disorder, electron-phonon coupling, doping and nonadiabatic effects*. Solid State Communications, 2007. 143(1-2): p. 47-57.
40. Malard, L.M., et al., *Raman spectroscopy in graphene*. Physics Reports, 2009. 473(5-6): p. 51-87.
41. DasA, et al., *Monitoring dopants by Raman scattering in an electrochemically top-gated graphene transistor*. Nat Nano, 2008. 3(4): p. 210-215.
42. Yan, J., et al., *Electric Field Effect Tuning of Electron-Phonon Coupling in Graphene*. Physical Review Letters, 2007. 98(16): p. 166802.

43. Pimenta, M.A., et al., *Studying disorder in graphite-based systems by Raman spectroscopy*. Physical Chemistry Chemical Physics, 2007. 9(11): p. 1276-1290.
44. He, R., et al., *Large Physisorption Strain in Chemical Vapor Deposition of Graphene on Copper Substrates*. Nano Letters, 2012. 12(5): p. 2408-2413.
45. Cançado, L.G., et al., *Influence of the Atomic Structure on the Raman Spectra of Graphite Edges*. Physical Review Letters, 2004. 93(24): p. 247401.
46. Vlassiuk, I., et al., *Role of Hydrogen in Chemical Vapor Deposition Growth of Large Single-Crystal Graphene*. ACS Nano, 2011. 5(7): p. 6069-6076.
47. Yu, Q., et al., *Control and characterization of individual grains and grain boundaries in graphene grown by chemical vapour deposition*. Nat Mater, 2011. 10(6): p. 443-449.
48. Duong, D.L., et al., *Probing graphene grain boundaries with optical microscopy*. Nature, 2012. 490(7419): p. 235-239.
49. Zhao, L., et al., *Influence of copper crystal surface on the CVD growth of large area monolayer graphene*. Solid State Communications, 2011. 151(7): p. 509-513.

Chapter 6

Summary and Future Experiments

6.1 Summary

As demonstrated in the last four chapters, we have achieved to grow large-area high-quality pristine, N-doped and B-doped monolayer graphene films on Cu substrates by CVD techniques, and we have mainly focused on characterizing these graphene films by STM/S and Raman spectroscopy, in conjunction with DFT calculations and NEXAFS measurements.

We found the crucial role that Cu substrate crystallicity plays in the quality of CVD grown graphene films, Cu(111) surface with the same crystal symmetry as graphene being most suitable for the CVD growths of high quality graphene films. Moreover, we used spectroscopic mapping technique to understand the interactions between graphene monolayer and Cu(111) substrate, and learnt that these electronic interactions modulate the band structure of Cu(111) surface states while charge transfer between graphene and Cu(111) is negligible.

With the knowledge of pristine graphene, we extended our scope to chemically doped graphene films, in particular, N-doped and B-doped graphene in this thesis. STM/S demonstrates that, as confirmed by NEXFAS in parallel, both nitrogen and boron dopants incorporate into graphene lattice mainly (>90% for N and >80% for B) via substitutional/graphitic doping form, and contribute charge carriers at a rate of approximately 0.5 carriers/dopants (0.5e/N and 0.5h/B). By

tuning the N/B dopant concentrations in the doped graphene films, we can well control the free charge carrier density, as well as the Fermi level position. Apart from this similarity between N- and B-doped graphene, subtle differences in atomic configuration between the two kinds of dopants lead to strikingly different dopant distribution between two sublattice of honeycomb structure in a large scale of a few hundreds nanometers. To be specific, B dopants interact with Cu substrates more than N dopants do, leading to an out-of-plane deformation of $\sim 0.4\text{\AA}$ for B dopant structures. As a result, the B dopants distribute randomly between two sublattices of graphene lattice while N dopants have sublattice segregations and form large domains (more than 100nm) of N dopants being in the same sublattice. Such sublattice clustering effect is the most efficient way to break sublattice symmetry in graphene, and possibly is another freedom that we can engineer with.

Besides looking at the properties of doped graphene films at nano-scales, we applied Micro-Raman spectroscopy mapping to expand our view up to micro-meter scale, so that we could learn the properties across and within grains of the CVD grown graphene polycrystal. Here, we focused on N-doped graphene, and found that N dopants avoid the grain boundaries for a few hundreds nanometers but stay uniform in the interior of each grain. This provides a piece of important information on the interplay between impurities/dopants and structural grain boundaries in two-dimensional polycrystals, which is different from traditional three dimensional case. Moreover, it also provides insights to explain the un-consistent transport properties reported in CVD grown N-doped graphene films.

Overall, we learnt about CVD grown pristine and N-/B-doped graphene from nano-scale up to micro-meter scale. Ongoing projects, considering probing the electronic properties of graphene

on other substrates and expanding the grain size of graphene polycrystals, will be discussed more in the following section, together with some preliminary results.

6.2 Future Experiments

Most of our measurements were performed on the as-grown samples where Cu substrates are in presence. Although Cu substrates do not affect the intrinsic electronic properties of pristine and chemically-doped graphene films strongly, they either do not have the flexibility as the dielectric substrates do.

Therefore, one possible future experiment could be STM/S studies of chemically doped graphene films on dielectric substrates, such as hexagonal BN. Hexagonal BN is a layered material just as graphite. Down to atomic structure, it resembles that of graphite as well, but replaces one sublattice of carbon atoms with boron atoms and the other sublattice of carbons with nitrogen atoms, which naturally breaks the sublattice symmetry. As such, BN is a wide band-gap material, with a uniform chemical potential across the surface. Due to the fact that it is bonded by weak Van de Waals forces between layers, BN can be exfoliated into thin layers and get deposited onto other substrates. It has been shown that pristine graphene sandwiched between two BN flakes has the highest mobility and most stability. With BN as the substrate for chemically doped graphene, we can not only explore the most intrinsic properties of such doped graphene films, but also own the ability to tune the carrier concentrations (chemical potential) of the doped graphene films by back gate the dielectric substrate, typically BN on SiO_2/Si (the geometry of which is shown in Fig. 6.1) [1]. The tunable carrier concentration in a chemically doped graphene film enables the studies of charge screening around a coulomb impurity (i.e. B or N dopant) in massless Dirac fermions as a function of carrier density, which has long been of great theoretical interest [2-4].

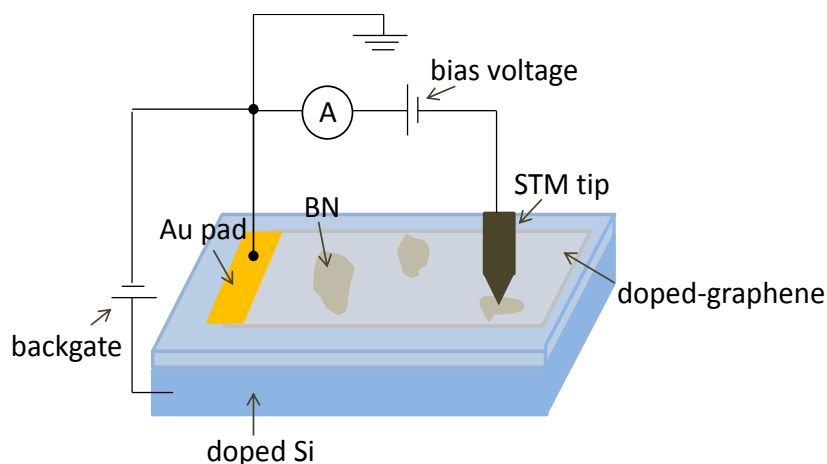


Fig. 6.1 Diagram of STM/S measurements of backgated doped graphene film on BN on SiO₂/Si substrates.

We have performed preliminary STM studies of exfoliated graphene on BN/SiO₂/Si, and displayed the results in Fig. 6.2a and b. The transfer process of such sample is described by a dry-micro-stage transfer technique in Ref. [5]. We found that the interface between graphene and BN is almost absent of impurities which is evident by the flatness of the topography (Fig. 6.2a with red arrows marking trapped impurities over the area) as well as the Moiré pattern formed between graphene and BN (Fig. 6.2b). However, similar transfer technique does not work well for CVD grown chemically doped graphene films, mainly because dopant sites tend to accumulate a lot of PMMA residues just as the grain boundaries in pristine graphene does [6, 7]. Moreover, the etchant of FeCl₃ nanoparticles gets trapped between graphene and substrates, making the interface between graphene and BN substrate dirty. Currently, efforts are made to solve these transfer issues, so that we could probe the intrinsic properties of the doped sample even after the “dirty” transfer process. Other than transferring CVD grown N-doped graphene onto BN, we can also try to post-

dope clean pristine graphene/BN by N ion bombardment or reaction with ammonia gas [8], and study their properties in-situ.

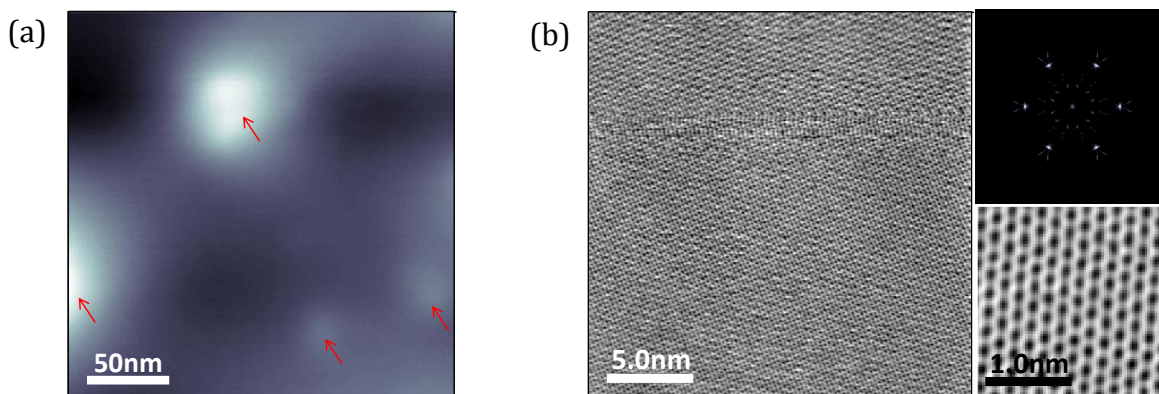


Fig. 6.2 STM topography of graphene on hexagonal BN flakes; (a) Large scale STM image of graphene/BN, with red arrows highlighting the impurities trapped between graphene and BN. (b) Zoom-in STM image of graphene/BN, displaying the atomic resolution (lower inset) and the superstructure (upper inset).

One main purpose of introducing free charge carriers into graphene is to increase the conductivity of the graphene film which depends on the product of free charge carrier density and carrier mobility. As we have shown in Chapter 3 and Chapter 4, both B and N dopants induce both inter-valley and intra-valley scattering in graphene, which will lower down the mobility of the film. Therefore, it is essential to check the mobility of the graphene system in the presence of dopants. Therefore, a second future experiment could be transport measurements of the chemically doped graphene films on BN substrates.

However, as we have demonstrated in the last chapter, the N dopants in N-doped graphene polycrystal distribute in-homogeneously over the surface, which avoid the structural grain boundaries in the graphene films but stay uniform in the interior of the grains. Considering the

irregular shape of the graphene grains and their small grain sizes ($\sim 3\text{-}5\mu\text{m}$ in diameter), it is not easy to measure the transport properties just within one grain of the graphene film. Therefore, a third possible project is to produce large-grain size doped graphene films. Along this direction, we have tried the pita-pocket recipe [9] at a low growth pressure. Our preliminary results are shown in Fig. 6.3, with the growth conditions of pita-pocket geometry, 10sccm CH_4 flow, 50sccm H_2 flow and 0.01torr of NH_3 . The optical image in Fig. 6.3a shows a single grain size of $\sim 40\mu\text{m}$ in diameter which is much larger than that in Chapter 5. Similarly, we measured Raman spectroscopy map over a single grain of such N-doped graphene flake and found the N distribution in each flake forms dendritic structure (shown in Fig. 6.3b), rather than a uniform one.

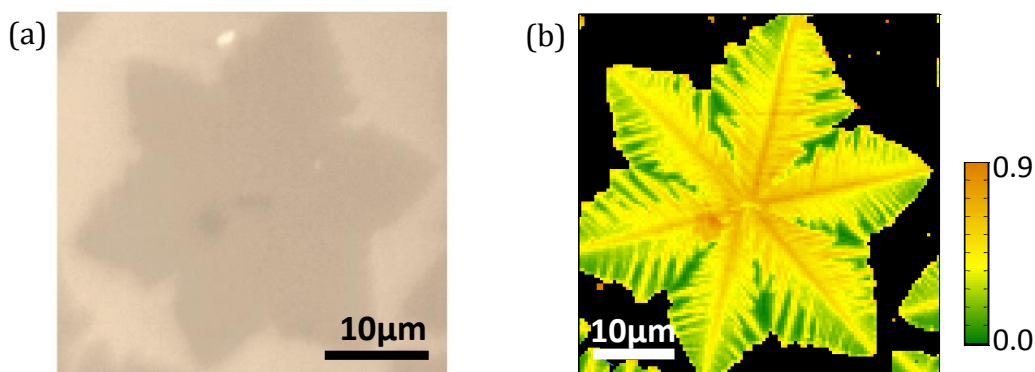


Fig. 6.3 Optical and Raman map images of large grain size N-doped graphene; (a) Optical image. (b) D/2D Raman map.

To investigate the role of H_2 flow in the N dopant distribution, we performed more growth with higher $\text{H}_2\text{:CH}_4$ ratios at same NH_3 partial pressure. Fig. 6.4(a) shows D/2D Raman map of a N-doped graphene flake grown with 300sccm H_2 flow. The N dopants tend to accumulate at the main axis of each lobe while the shape of the graphene flake is similar as that in Fig. 6.3. Moreover, we tried to grow N-doped graphene with two layer of pita-pocket geometry but same gas flows as in Fig. 6.4(a), and presented the result of D/2D map in Fig. 6.4(b). The shape of graphene islands is

cultivated into hexagons while the N dopants remain high concentration along the axis. Up to this stage, we are still working on growing large-grain size N-doped graphene films with uniform N distribution inside the grains.

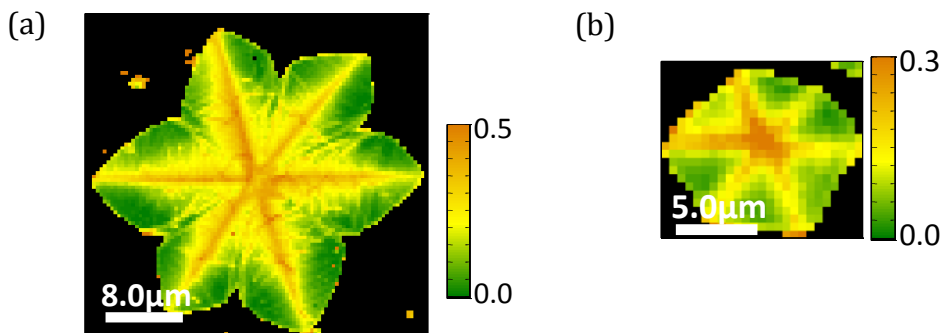


Fig. 6.4 Influence of H_2 flow on the N dopant distribution and island shape; (a) D/2D Raman map of N-doped graphene grown with $H_2:CH_4$ ratio of 300:10sccm; (b) D/2D map of N-doped graphene with double layer pita-pocket geometry.

6.3 Reference

1. Decker, R., et al., *Local electronic properties of graphene on a BN substrate via scanning tunneling microscopy*. Nano letters, 2011. 11(6): p. 2291-2295.
2. Cheianov, V.V. and V.I. Fal'ko, *Friedel oscillations, impurity scattering, and temperature dependence of resistivity in graphene*. Physical review letters, 2006. 97(22): p. 226801.
3. Pereira, V.M., J. Nilsson, and A.C. Neto, *Coulomb impurity problem in graphene*. Physical review letters, 2007. 99(16): p. 166802.
4. Biswas, R.R., S. Sachdev, and D.T. Son, *Coulomb impurity in graphene*. Physical Review B, 2007. 76(20): p. 205122.
5. Dean, C., et al., *Boron nitride substrates for high-quality graphene electronics*. Nature nanotechnology, 2010. 5(10): p. 722-726.
6. Huang, P.Y., et al., *Grains and grain boundaries in single-layer graphene atomic patchwork quilts*. Nature, 2011. 469(7330): p. 389-392.
7. Kim, K., et al., *Grain boundary mapping in polycrystalline graphene*. ACS nano, 2011. 5(3): p. 2142-2146.

8. Wang, H., T. Maiyalagan, and X. Wang, *Review on recent progress in nitrogen-doped graphene: synthesis, characterization, and its potential applications*. *Acs Catalysis*, 2012. **2**(5): p. 781-794.
9. Li, X., et al., *Graphene films with large domain size by a two-step chemical vapor deposition process*. *Nano letters*, 2010. **10**(11): p. 4328-4334.